



UNIVERSITÀ  
DEGLI STUDI  
DI PADOVA

Sede Amministrativa: Università degli Studi di Padova

Dipartimento di:

INGEGNERIA DELL'INFORMAZIONE

Scuola di dottorato di ricerca in:

SCIENZE E TECNOLOGIE DELL'INFORMAZIONE

Ciclo: 27°

**TITOLO TESI:**

**Modeling, estimation and control of ring Laser Gyroscopes  
for the accurate estimation of the Earth rotation**

**Direttore della Scuola** : Ch.mo Prof. Matteo Bertocco

**Coordinatore** : Ch.mo Prof. Carlo Ferrari

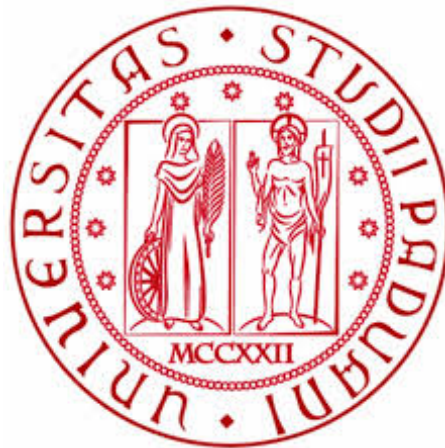
**Supervisore** : Ch.mo Prof. Alessandro Beghi

**Dottorando:** Davide Cuccato



MODELING, ESTIMATION AND CONTROL OF RING LASER  
GYROSCOPES FOR THE ACCURATE ESTIMATION OF THE  
EARTH ROTATION

DAVIDE CUCCATO



Information Engineering Department (DEI)  
Faculty of Engineering  
University of Padua, Università degli studi di Padova  
February, 18, 2015 – version 2

Davide Cuccato: *Modeling, estimation and control of ring Laser Gyroscopes for the accurate estimation of the Earth rotation*, © February, 18, 2015

**SUPERVISORS:**

Alessandro Beghi  
Antonello Ortolan

**LOCATION:**

Padova, (Italy)

**TIME FRAME:**

February, 18, 2015

...Ho presentato il dorso ai flagellatori,  
la guancia a coloro che mi strappavano la barba;  
non ho sottratto la faccia agli insulti e agli sputi...

—*Libro di Isaia 50, 6.*—

Dedicated to the loving memory of Giovanni Toso.  
1986 – 2014



## ABSTRACT

---

*He – Ne* ring lasers gyroscopes are, at present, the most precise devices for absolute angular velocity measurements. Limitations to their performances come from the non-linear dynamics of the laser. Accordingly to the *Lamb* semi-classical theory of gas lasers, a model can be applied to a *He–Ne* ring laser gyroscope to estimate and remove the laser dynamics contribution from the rotation measurements.

We find a set of critical parameters affecting the long term stability of the system. We propose a method for estimating the long term drift of the laser parameters, and for filtering out the laser dynamics effects, e.g. the light backscattering. The intensities of the counter-propagating laser beams exiting one cavity mirror are continuously measured, together with the monitor of the laser population inversion. These quantities, once properly calibrated with a dedicated procedure, allow us to estimate cold cavity and active medium parameters of the *Lamb* theory. Our identification procedure, based on the perturbative solutions of the laser dynamics, allow us for the application of the *Kalman* Filter theory for the estimation of the angular velocity.

The parameter identification and backscattering subtraction procedure has been verified by means of a Monte Carlo studies of the system, and then applied to the experimental data of the ring lasers *G-PISA* and *G-WETTZELL*. After the subtraction of laser dynamics effects by *Kalman* filter, the relative systematic error of *G-PISA* reduces from 50 to 5 parts in  $10^3$ , and it can be attributed to the residual uncertainties on geometrical scale factor and orientation of the ring. We also report that after the backscattering subtraction, the relative systematic errors of *G-WETTZELL* are reduced too.

Conversely, in the last decade an increasing attention was drawn to high precision optical experiments, e.g. ring laser experiments, which combine high sensitivity, accuracy and long term stability. Due to the experimental requirements, position and orientation of optical elements and laser beams formation must be controlled in the field of nano-positioning and ultra-precision instruments. Existing methods for beam direction computing in resonators, e.g. iterative ray tracing or generalized ray transfer matrices, are either computationally expensive or rely on overparametrized models of optical elements.

By exploiting the *Fermat's* principle, we develop a novel method to compute the beam directions in resonant optical cavities formed by spherical mirrors, as a function of mirror positions and curvature radii. The proposed procedure is based on the geometric Newton method on matrix manifold, a tool with second order convergence

rate that relies on a second order model of the cavity optical length. As we avoid coordinates to parametrize the beam position on mirror surfaces, the computation of the second order model does not involve the second derivatives of the parametrization.

With the help of numerical tests, we show that the convergence properties of our procedure hold for non-planar polygonal cavities, and we assess the effectiveness of the geometric Newton method in determining their configurations with an high degree of accuracy and negligible computational effort.

We also presents a method to account for the (ring laser) cavity deformations due to mirrors displacement, seen as the residual motions of the mirrors centers after the removal of rigid body motions. Having the cavity configuration and the model to account for mirrors movements, the calibration and active control of the optical cavity can be addressed as a control problem. In fact, our results are of some importance not only for the design and simulation of ring laser gyroscopes, but also for the active control of the optical cavities.

In the final part of this work we detail a complete model including the simulation of the physical processes of interest in the operation of a ring laser gyroscope. Simulation results for the application of the model to the ring laser *GP2* are presented and discussed.

## SOMMARIO

---

I giroscopi laser che sfruttano la tecnologia *He – Ne* a 632 nm sono attualmente i dispositivi più precisi per la misura accurata della velocità angolare di rotazione. Gli attuali limiti alle loro prestazioni provengono dalla dinamica non lineare del battimento laser. Sfruttando la teoria semi-classica di *Lamb* viene sviluppato un modello per la dinamica del laser, successivamente applicato per stimare e rimuovere il contributo della dinamica del laser dalle misure di rotazione di un giroscopio.

Individuati una serie di parametri critici la cui variazione influenza la stabilità nel tempo della misura, viene proposto un metodo per stimare la deriva dei parametri laser e per filtrare gli effetti della dinamica laser dalle misure acquisite con il giroscopio. Le intensità dei fasci laser contropropaganti che escono da uno specchio della cavità sono acquisite, assieme ad un monitor della inversione di popolazione laser. Questi osservabili, una volta correttamente calibrati con una procedura dedicata, permettono di stimare i parametri dissipativi di cavità fredda e i parametri del mezzo attivo, che determinano la parte principale delle non linearità del sistema. La procedura di identificazione, basata sulle soluzioni perturbative della dinamica del laser, ci consente l'applicazione di un filtro di *Kalman* per la stima della velocità angolare.



La procedura di identificazione dei parametri e sottrazione delle sistematiche laser è stata validata mediante uno studio Monte Carlo del sistema, inoltre i risultati delle analisi su dati sperimentali dei prototipi *G-PISA* e *G-WETTZELL* sono mostrati e discussi. Dopo la sottrazione della dinamica del laser mediante filtro di *Kalman*, l'errore sistematico relativo alla frequenza di rotazione di *G-PISA* si riduce da 50 a 5 parti in  $10^3$ , residuo che può essere attribuito alle incertezze residue sul fattore di scala geometrico e sull'orientamento del giroscopio. Anche nel caso dell'analisi dei dati di *G-WETTZELL* si segnala che l'errore sistematico relativo viene ridotto.

Negli ultimi dieci anni, una crescente attenzione è stata attirata da esperimenti ottici di alta precisione, ad esempio, esperimenti basati su giroscopi laser, che combinano alta sensibilità, precisione e stabilità a lungo termine. Per soddisfare a stringenti requisiti sperimentali, la posizione e l'orientamento degli elementi ottici, e la formazione dei fasci laser, devono essere controllati nel campo degli strumenti di nano-posizionamento e ultra-precisione. Metodi esistenti per il calcolo del cammino del fascio laser in risonatori, ad esempio, il ray tracing iterativo o le matrici di trasferimento generalizzate, sono computazionalmente costosi o si basano su modelli ridondanti di elementi ottici.

Sfruttando il principio di *Fermat*, un nuovo metodo per calcolare il cammino ottico in cavità risonanti formate da specchi sferici è sviluppato, in funzione delle posizioni degli specchi e del valore dei rispettivi raggi di curvatura. La procedura proposta si basa sul metodo di Newton geometrico, un algoritmo con tasso di convergenza del secondo ordine che si basa su un modello del secondo ordine della lunghezza ottica della cavità. Evitando di parametrizzare con coordinate la posizione del raggio laser sugli specchi, il calcolo del modello di secondo ordine non coinvolge le derivate seconde della parametrizzazione.

Con l'aiuto di simulazioni numeriche, si dimostra che le proprietà di convergenza della nostra procedura valgono per un vasto insieme di cavità poligonali non planari, e viene valutata l'efficacia del metodo di Newton geometrico nella determinazione delle configurazioni delle cavità laser con un alto grado di precisione e sforzo computazionale trascurabile.

Viene anche presentato un metodo per tenere conto delle deformazioni della cavità ottica dovute agli spostamenti degli specchi, ovvero gli spostamenti degli specchi che non si traducono in movimenti di corpo rigido della cavità stessa. Conoscendo la configurazione della cavità e avendo un modello per descrivere i movimenti degli specchi, la calibrazione ed il controllo attivo della cavità ottica possono essere studiati. I nostri risultati sono infatti di una certa importanza non solo per la progettazione e la simulazione, ma anche per l'allineamento e in linea di principio anche per il controllo attivo di giroscopi laser

ad alta precisione.

Nella parte finale di questo lavoro si descrive il modello *RLG*, un modello multiuso completo comprensivo della simulazione accurata di tutti i processi fisici rilevanti nel funzionamento di un giroscopio laser ad alta risoluzione. I risultati della simulazione dell'applicazione del modello *RLG* al giroscopio *GP2* vengono presentati e discussi.

## PUBLICATIONS

---

### *Journal papers*

- R. Santagata *et. al.* "Optimization of the geometrical stability in square ring laser gyroscopes" *Classical and Quantum Gravity*, 32, 5 January (2015).
- J. Belfi *et. al.* "Interferometric length metrology for the dimensional control of ultra-stable ring laser gyroscopes" *Classical and Quantum Gravity*, 31, 22, (2014).
- D. Cuccato *et. al.* "Controlling the non-linear intracavity dynamics of large He-Ne laser gyroscopes ", *Metrologia*, 51, 1, (2014).
- A. Di Virgilio *et. al.* "A ring lasers array for fundamental physics" *Comptes Rendus Physique*, 15, 10, (2014).
- A. Beghi *et. al.* "Compensation of the laser parameter fluctuations in large ring-laser gyros: a Kalman filter approach", *Applied Optics*, 51, 31, (2012).

### *Conference papers*

- J. Belfi *et. al.* "Experimental activity toward GINGER (gyroscopes IN general relativity)" *Laser Optics, 2014 International Conference, IEEE.*
- N. Beverini *et. al.* "Toward the "perfect square" ring laser gyroscope" *Photonics Technologies, 2014 Fotonica AEIT Italian Conference on, IEEE.*
- J Belfi *et. al.* "Absolute control of the scale factor in GP2 laser gyroscope: Toward a ground based detector of the lense-thirring effect" *European Frequency and Time Forum & International Frequency Control Symposium (EFTF/IFC), 2013 Joint, IEEE.*
- D. Cuccato *et. al.* "Laser dynamics effects on the systematics of large size laser gyroscopes" *European Frequency and Time Forum & International Frequency Control Symposium (EFTF/IFC), 2013 Joint, IEEE.*
- J. Belfi *et. al.* "Laser gyroscopes for very high sensitive applications" *European Frequency and Time Forum (EFTF), 2012, IEEE.*



*Odi et amo. Quare id faciam, fortasse requiris.  
Nescio, sed fieri sentio et excrucior.*

## ACKNOWLEDGMENTS

---

Many thanks to my family: Sara, Renata, Federico, Giulia, and Riccardo, thanks guys for supporting and guiding me through this challenge, *“Ogni mio traguardo è solo merito vostro”*. Also, I wish to thank my supervisors: Prof. Alessandro Beghi, for the wonderful and precious opportunity of pursuing my doctorate; and Dott. Antonello Ortolan, for introducing me into the fantastic world of physical signal processing and estimation. I finally want to thank the GINGER collaboration, especially Jacopo Belfi, Nicolò Beverini, Giorgio Carelli, Angela Di Virgilio, Alberto Donazzan, Enrico Maccioni, Giampiero Naletto, Maria Pellizzo, and Rosa Santagata for the valuable conversations and for the wise advices.



# CONTENTS

---

1	INTRODUCTION	1
1.1	The ring laser as a gyroscopic instrument	1
1.2	Outline of the thesis	4
1.3	Previous & Related Works	5
1.4	Current and Future developments of RLs	8
1.4.1	<i>G-PISA</i> and its experimental setup	9
1.4.2	General Relativity Tests: the <i>GINGER</i> detector	10
2	THE RLG MODEL: LASER DYNAMICS	13
2.1	Physical preliminaries and RL semi-classical treatment	13
2.1.1	RL equations: complex fields	14
2.1.2	RL equations: real variables	15
2.1.3	RL standard outputs	16
2.2	Parameters of RL dynamics	17
2.2.1	Laser medium parameters	18
2.2.2	Dissipative parameters	22
2.3	Study of RL dynamics	24
2.3.1	Lamb parameters effect on RL performances	25
2.3.2	Steady state approximate solutions	26
2.4	Calibration and Identification Procedures	28
2.4.1	Dissipative parameters identification	28
2.4.2	Experimental calibration	29
2.4.3	Estimation of $\omega_s$ by EKF	33
2.4.4	Pre-filtering scheme implementation	34
2.5	Results and Discussion	34
2.5.1	Simulation results	35
2.5.2	Analysis of <i>G-PISA</i> data	38
2.5.3	Analysis of <i>G-WETTZELL</i> data	46
3	THE RLG MODEL: CAVITY GEOMETRY	53
3.1	Computing the laser beam path in Optical Cavities	53
3.1.1	Notation and Definitions	54
3.1.2	Problem Statement for a RL cavity	57
3.1.3	Review of the Geometric Newton Algorithm	59
3.1.4	The Newton Algorithm on $\mathcal{OB}(2, N)$	62
3.1.5	Application to Square RL Cavity	64
3.1.6	Numerical Study	66
3.2	Pose and Shape of four points in $\mathbb{R}^3$	70
3.2.1	Pose and Shape Decomposition	72
3.2.2	From Shape to Distance Matrix	78
3.2.3	Simulation results	79
4	COMPLETE RLG MODEL	83
4.1	Complete RLG model overview	83
4.1.1	<i>IN</i> :Simulation parameters	83

4.1.2	<i>IN</i> :Signal & noise generation block	85
4.1.3	<i>RLG_CAV</i> : Optical cavity model	86
4.1.4	Diagonal loop	87
4.1.5	<i>RLG_PAR</i> : Backscattering and detuning model	87
4.1.6	<i>RLG_PAR</i> : <i>He – Ne</i> laser model & <i>Lamb</i> Parameters	87
4.1.7	<i>RLG_DYN</i> : RL dynamics integrator	88
4.1.8	Intensity loop	88
4.1.9	<i>OUT</i> : Simulation outputs	88
4.2	Results of the complete simulation of GP2	89
5	CONCLUSIONS	95
5.1	Ring laser dynamics	95
5.2	Ring laser geometry	96
5.3	Complete RLG model	97
A	APPENDIX	99
A.1	Proof of Proposition 1	99
A.2	Proof of Lemma 6	99
	BIBLIOGRAPHY	101



## LIST OF FIGURES

---

- Figure 1 A schematic of a *RLG*: 4 mirrors delimiting the ring square cavity, the two laser modes counter-rotating; in one corner the two output beams are made to interfere and the beat note of *Sagnac* frequency is shown. 2
- Figure 2 *G-PISA* on top of its granite table, moved from its installation in S.Piero (Pisa). 10
- Figure 3 Plot of the computed gain (a) and dispersion (b) profiles of the plasma polarizability in the *RL* cavity (continuous line), and of its contributions from  $^{20}\text{Ne}$  isotope (dashed line), and  $^{22}\text{Ne}$  isotope (dotted line), assuming  $I_1 = I_2 = I$ . The black lines represent the unsaturated profile ( $I \rightarrow 0$ ), the blue and red lines represent profiles saturated by signals of intensity  $I = 0.1$ , and  $I = 0.2$ , respectively. The vertical dashed lines indicate the centers of the broadening profiles of the Ne isotopes. 21
- Figure 4 Simulated *Allan* deviations of the estimated rotation rate. See the text for details. 26
- Figure 5 Schematic of the parameter estimation procedure, where *LP*  $\rightarrow$  lowpass *Butterworth* filter, *BP*  $\rightarrow$  bandpass *Butterworth* filter, *ZD*  $\rightarrow$  Zoom and Decimation routine, *HT*  $\rightarrow$  *Hilbert* transform (see text). 35
- Figure 6 Histograms of the relative errors  $(\hat{\alpha}_{1,2} - \alpha_{1,2})/\alpha_{1,2}$  that affect the estimation of Gain minus losses parameters calculated with  $2 \times 10^4$  realizations of the *RL* dynamics. (a) Histogram relative to  $\alpha_1$  : mean  $1.4 \times 10^{-3}$  and standard deviation  $2.9 \times 10^{-3}$ ; (b) histogram relative to  $\alpha_2$  : mean  $-2.5 \times 10^{-4}$  and standard deviation  $3.9 \times 10^{-3}$ . 37
- Figure 7 Histograms of the relative errors  $(\hat{r}_{1,2} - r_{1,2})/r_{1,2}$  that affect the estimation of backscattering coefficients calculated with  $2 \times 10^4$  realizations of the *RL* dynamics. (a) Histogram relative to  $r_1$  : mean  $1.1 \times 10^{-3}$  and standard deviation  $4.6 \times 10^{-3}$ ; (b) histogram relative to  $r_2$  : mean  $1.3 \times 10^{-3}$  and standard deviation  $3.2 \times 10^{-3}$ . 37

- Figure 8 Histogram of the absolute errors  $\hat{\varepsilon} - \varepsilon$  that affect the estimation of backscattering phase calculated with  $2 \times 10^4$  realizations of the *RL* dynamics; mean  $-4.3 \times 10^{-4}$  rad and standard deviation  $2.8 \times 10^{-3}$  rad. 37
- Figure 9 *Allan* deviation of the rotation rate estimated by *AR*(2) method (dots) and *EKF* (open diamonds) using  $2 \times 10^4$  seconds of the Monte Carlo simulation with random walk of *Lamb* Parameters. For comparison, we also plot the *Allan* deviation of the simulated rotational drift (open triangles), and the *Allan* deviation of the *EKF* estimation after the subtraction of the rotational drift (dash dotted line). 38
- Figure 10 The experimental setup for the rotation measurement and the calibration of the *RL* parameters. *PMT*: photomultiplier tube, *TA*: transimpedance amplifier, *LF*:line filter, *CL*: Collimating lens, *ECDL*: extended cavity diode laser, *TA* gain for *G-PISA* is  $1 \text{ G}\Omega$ . 40
- Figure 11 Comparison of the estimated and observed time series of  $I_1(t)$ ,  $I_2(t)$  and  $\sin(\psi(t))$  using the experimental data of *G-PISA*. 41
- Figure 12 Time series of the  $\alpha_{1,2}$ ,  $\beta$ ,  $r_{1,2}$  and  $\varepsilon$ . The parameters  $\alpha_{1,2}$ ,  $r_{1,2}$  and  $\varepsilon$  have been estimated using  $2 \times 10^4$  seconds of experimental data of *G-PISA*. 41
- Figure 13 Power spectrum of the interferogram data around the *Sagnac* frequency  $\sim 107.3$  Hz. 42
- Figure 14 *Allan* deviation of the rotation rate estimated by *AR*(2) method (dots) and *EKF* (open diamonds) using  $2 \times 10^4$  seconds of experimental data of *G-PISA*. An increase of a factor of 1.5 in rotation-rate resolution and of a factor of 2 in the time stability is observed. 43
- Figure 15 *Doppler* profile of the closed optical transition in Neon at 640.2 nm, allowing for the Neon temperature estimation. The measurement is taken in typical operation conditions for a plasma of *He - Ne* standard mixture at 4.5 mbar. Using the standard Matlab procedure for fitting custom functions, we get a reduced R-squared of 0.9947 and the fitting parameters  $a' = -4.9 \pm 0.1$ ,  $b' = -2.44 \pm 0.05$ ,  $k' = 0.65 \pm 0.02$ ,  $\eta' = 0.27 \pm 0.02$ . 44

- Figure 16 Plot of *RDT* data sampled at 10 MHz with the fitting functions  $n_{1,2} \exp(-\mu_{1,2} ct/L)$  for clockwise (*a*) and counter-clockwise (*b*) beams, respectively. The reduced *R*-squared from Matlab fitting toolbox are  $R_1^2 = 0.9969$ , and  $R_2^2 = 0.9955$ , and the fitting parameters are  $\mu_1 = (1.136 \pm 0.02) \times 10^{-4}$ ,  $\mu_2 = (1.146 \pm 0.02) \times 10^{-4}$ ,  $n_1 = (1.898 \pm 0.005) \times 10^{-1}$ ,  $n_2 = (1.982 \pm 0.005) \times 10^{-1}$ . 45
- Figure 17 Plot of single pass gain of *G-PISA* as a function of the gain monitor  $V_p$ . Each point represents the average of 10 measurements and the corresponding error bar is their standard deviation. The linear fit gives  $a = 9.87 \times 10^{-5}$ ,  $b = 1.303 \times 10^{-4}$ ,  $\sigma_a = 1.57 \times 10^{-6}$ , and  $\sigma_b = 2 \times 10^{-7}$ . 46
- Figure 18 Histograms of the estimates of *AR*(2) (pale gray) and *EKF* (dark gray) during 2 days of *G-PISA* data. The grey rectangular area represents the residual uncertainty on the predicted *Sagnac* frequency, due to geometric and orientation tolerances. Note that the *EKF* mean is shifted with respect to *AR*(2) mean (removal of null shift contribution), and that the *EKF* standard deviation is  $\sim 10$  times lower than the *AR*(2) standard deviation (increasing of long-term stability). 47
- Figure 19 *Allan* deviations of *AR*(2) (upper curve) and *EKF* (lower curve) rotational frequency estimates. The straight line represents the shot noise level of *G-PISA* for a cavity quality factor of  $5.4 \times 10^{11}$  and an output power of 4 nW. 47
- Figure 20 Plot of the means  $I_{1,2}$  (top box), of the modulations  $i_{1,2}$  (middle box) and of the phases  $\phi_{1,2}$  as estimated by the pre-filtering routine from the time series of  $I_1(t)$ ,  $I_2(t)$  and  $S(t) \sim \sin(\psi(t))$  using the experimental data of *G-WETTZELL*. 48
- Figure 21 Time series of the  $\alpha_{1,2}$ ,  $r_{1,2}$  and  $\varepsilon_{1,2}$  estimated using the experimental data of *G-WETTZELL*. 49
- Figure 22 Comparison between the *AR*(2) estimation of *G-WETTZELL* beat frequency (black and blue lines) and the estimation of the laser systematics (red lines). In the second plot the mean values of the signals have been removed. 50

- Figure 23 *Allan* deviation of the same data of Fig.22, with ( red line ) and without ( black line ) the subtraction of the laser systematics. 51
- Figure 24 Parametrization of the position of the laser spot on the  $k$ -th mirror. With respect to the inertial frame origin  $O$ , the position of laser spot is  $\mathbf{z}_k = r_k \mathbf{x}_k + \mathbf{c}_k$ . The mirror  $M_k$  has radius  $r_k$ . Relative to the mirror center  $\mathbf{c}_k$ , the position of the laser spot can be parametrized as  $r_k \mathbf{x}_k$ ,  $\mathbf{x}_k \in \mathbb{S}^2$ . 57
- Figure 25 Plot of  $h(x_k) = \|\nabla p(x_k)\|$  versus the iteration index  $k$ . 67
- Figure 26 Comparison between the functions  $p$  and its second order geometric model, and between the function  $h$  and the *Armijo* condition, on consecutive algorithm iterations from 1 to 5. The black lines represent the second order geometric model for  $p$  and the *Armijo* condition, and the red lines represent the functions  $p$  and  $h$ , respectively. The blue crosses displayed are the iterates of the line search method. 69
- Figure 27 An example of displacements of mirrors forming a square optical cavity. Elements relative to each mirror are colored in grey. Red dots mark the mirror centers, the thick orange lines represent the optical path length as a link between consecutive laser spots  $\mathbf{z}_k$ . 70
- Figure 28 In the top picture the red figure is obtained from the black one by a dilatation of the points, while in the bottom picture only the pose of the points has been changed. 71
- Figure 29 Visual scheme of the proposed set of coordinate for  $P$ . 76
- Figure 30 Picture of the domain of  $\mathbf{v}$ . The colored lines are the excerpted lines due to the nonlinear constraints  $P_i \wedge P_{i+1} \neq \mathbf{0}$ . 77
- Figure 31 Histograms of the relative variations of  $p$  (dark grey), and  $k_s$  (light grey) due to mirror displacements. The histograms of the relative variations of  $p$  and  $\|\mathbf{a}\|$  are similar. 80
- Figure 32 Histograms of the relative variations of  $p$  (dark grey), and  $k_s$  (light grey) due to mirror displacements. In all simulations the values of the first two diagonal entries of the matrix  $A$  were fixed to 2.87. 80

Figure 33	Relative standard deviation of $k_S$ as a function of $\sigma$ in the 4 cases: unconstrained ring (black), ring with constrained diagonal elements of $T$ (red), intermediate case with $\epsilon_d = 10^{-3}$ (green), and $\epsilon_d = 10^{-6}$ (blue). 81
Figure 34	<i>Simulink</i> schematic of the <i>RLG</i> model. The signal & noise generation block synthesizes the input signals and fed them to the optical cavity model, to the backscattering and detuning model, to the <i>He – Ne</i> laser model, and to the diagonal and intensity loops blocks. The optical cavity model feeds the diagonal loop and the backscattering and detuning model, both the optical cavity model and the backscattering and detuning model generate inputs for the <i>He – Ne</i> laser mode and the <i>Lamb</i> parameters generation block. The <i>He – Ne</i> laser mode and the <i>Lamb</i> parameters generation block feeds the <i>RL</i> dynamics integrator, and the signal $I_1$ is fed back to the intensity loop. 84
Figure 35	Flowchart diagram of the complete <i>RLG</i> model. The continuous lines represent the data shared between blocks, and the dashed lines indicate the presence of feedback loops. 85
Figure 36	<i>Simulink</i> block for the diagonal loop. 87
Figure 37	Realization of $\mu_{1,2}$ , <i>temp</i> and <i>press</i> for the simulation case study. 91
Figure 38	Optical cavity lengths $l_{1,2,3,4}$ resulting for the simulation case study. 91
Figure 39	Optical cavity lengths $d_{1,2}$ and $p$ resulting for the simulation case study. 92
Figure 40	<i>Sagnac</i> frequency $f_s$ as a result of the simulation case study. 92
Figure 41	<i>Lamb</i> parameters and backscattering parameters for the simulation case study. 93
Figure 42	Plot of the simulated $S_{1,2}$ and $I_{1,2}$ . 94

## LIST OF TABLES

---

Table 1	<i>He – Ne</i> laser system parameters. 15
---------	--

Table 2	Complex value of the polarization contributions as expressed in Eq.(28) and Eq.(32) for the clockwise wave calculated at a detuning $\xi_{max} = 0.05$ with respect to the center of the absorption profiles of $^{20}\text{Ne}$ and $^{22}\text{Ne}$ . 18
Table 3	Reference values of the <i>Lamb</i> parameters used in the simulation of <i>G-PISA</i> dynamics. The contribution of $r_{1,2}$ and $\tau$ to the <i>Sagnac</i> frequency is of the order of 1.5 Hz and $10^{-2}$ Hz, respectively. 36
Table 4	Contributions to the accuracy budget of <i>G-PISA</i> from systematic errors in the estimate of <i>Lamb</i> parameters. 48
Table 5	Expression for the coordinate representation of $D \text{grad } \bar{f}(x)[\eta_x]$ and of $P_x(\xi_x)$ on the Oblique manifold $\mathcal{OB}(2, N)$ . 62

## INTRODUCTION

---

### 1.1 THE RING LASER AS A GYROSCOPIC INSTRUMENT

A Ring Laser Gyroscope (*RLG*) is a planar device that employs laser light for the measure of rotation rates. The modern setup of an high sensitivity *RLG* consists in a closed optical cavity of triangular or square shape made with mirrors as vertexes and gas-filled tubes as sides. To excite the *He – Ne* laser transition of wavelength  $\lambda = 632.8$  nm, the cavity is supplied with a radio-frequency circuit in the middle of a side, for the gas discharge. In standard working conditions, two optical waves counter-propagate inside the ring cavity. In an inertial frame, each beam follows a path of the same length. When the cavity rotates, a time difference between the clockwise and counter-clockwise beams occurs. This translates into a frequency difference of the two beams which carries the information about the rotation rate of the *RLG* frame. To measure the frequency difference, in one vertex is located a beam combiner which generates the interference signal detected by a photodiode.

Fig.1 shows a schematic of a *RLG*. The physical mechanism that transduces rotations into fringe shifts is named after the physicist *Georges Sagnac*, who predicted and demonstrated the first passive ring interferometer in 1913 [52]. Although *Sagnac* had the purpose to detect the effect of the relative motion of the Earth and the ether, successive works explained the *Sagnac* effect in the framework of the Special and General Relativity [55]. To achieve a high sensitivity, the active interferometric setup is preferred to the original set up. In the former case, light is excited directly inside the ring cavity and the signal detected is a beat note, i.e. a frequency shift, while in the latter case light enters the cavity from outside and the signal detected is a phase shift. Nowadays the *RLGs* are the industry standard for precision rotation measurement, being crucial components in air and marine navigation systems, platform stabilization systems, pointing and targeting systems, and attitude and heading reference systems. In the commercial area *RLGs* are eventually preferred among the rotational sensors for low cost, no moving parts, and compact form factor. Typical commercial performances include start-up time of 1 second, bias stability less than 0.04 degree/hour, and angular random walk less than  $10^{-5}$  rad $\sqrt{\text{Hz}}$  [37].

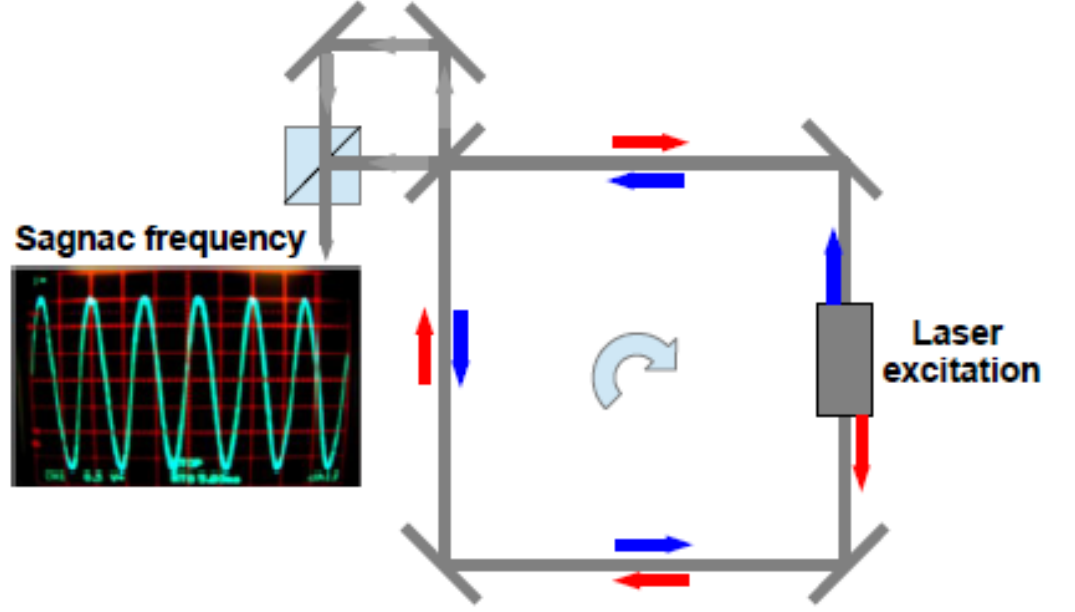


Figure 1: A schematic of a RLG: 4 mirrors delimiting the ring square cavity, the two laser modes counter-rotating; in one corner the two output beams are made to interfere and the beat note of *Sagnac* frequency is shown.

In a rotating Ring Laser (*RL*) the frequency difference between two electromagnetic waves (i.e. the frequency of the beat signal between the two beams) reads

$$\nu_s = \frac{4A}{\lambda L} \mathbf{n} \cdot \boldsymbol{\Omega} , \quad (1)$$

where  $\nu_s$  is the *Sagnac* frequency,  $A$  and  $L$  are the area and the length of the cavity, respectively,  $\lambda$  is the wavelength of the laser beam,  $\mathbf{n}$  is the unit vector normal to the plane containing the ring cavity, and  $\boldsymbol{\Omega}$  is the angular velocity of the detector. The ratio  $A/L$  is the scalar compactness factor of the instrument.

The dynamics of a *RL* is one of the sources of systematic errors in the estimate of  $\nu_s$ , and therefore in the measure of  $\boldsymbol{\Omega}$ . In fact, the laser dynamics is determined by a set of non-linear equations that depends on parameters which are slowly varying due to changes in environmental conditions of the ring cavity (mainly temperature and atmospheric pressure). Moreover, in the operation of high resolution *RLs*, some parameters, e.g. the laser detuning and the voltage oscillator power are actively controlled, with the drawback of enhancing the drifts of others parameters. To take into account the different error sources that corrupt the beat signal of a *RL*, Eq.(1) is modified as

$$\nu_s = \left( \frac{4A}{\lambda L} + \Delta\nu_{SF} \right) \mathbf{n} \cdot \boldsymbol{\Omega} + \Delta\nu_0 + \Delta\nu_{BS} + \eta , \quad (2)$$



where the deviations from ideal behavior in Eq.(1) involved in the measure of the *Sagnac* frequency are:

- Photon shot-noise described by the stochastic white noise process  $\eta$ , which is due to light incoherence. Shot-noise poses a fundamental limit to the angular velocity resolution of a *RLG*, as fluctuations limit the resolution of the instrument for a given integration time. The related power spectral density reads

$$P_{\eta\eta}^{1/2} = \frac{c}{\lambda Q} \sqrt{\frac{h\nu}{P_{out}}} , \quad (3)$$

where  $Q$  is the quality factor of the optical cavity,  $h$  the Planck constant,  $P_{out}$  the optical power detected by photodiodes,  $c$  the speed of light, and  $\nu = c/\lambda$  the light frequency.

- Corrections to the scale factor  $\Delta\nu_{SF}$ , which are due to fluctuations of either the ring cavity shape or the laser gain, cavity losses, plasma temperature and pressure, and also to the detuning between the gain center frequency and optical frequencies.
- Null shift errors  $\Delta\nu_0$ , due to any cavity non-reciprocity, e.g. cavity non planarity or asymmetries in the cavity geometry, gas flows inside the tubes, parasite magnetic fields and mirror birefringence.
- Non-linear coupling of the counter-propagating laser beams  $\Delta\nu_{BS}$ , due to light retro-reflections, also known as backscattering.

Eq.(3) leads to a standard deviation for  $\nu_s$ ,  $\sigma_\nu = P_{\eta\eta}^{1/2}/\sqrt{T}$ , where  $T$  is the integration time considered for the measure. This standard deviation, converted in equivalent rotational noise and expressed in unit of rad/s, reads

$$\sigma_\Omega = \frac{cL}{4AQ} \sqrt{\frac{h\nu}{P_{out}T}} , \quad (4)$$

note that the intrinsic noise level is inversely proportional to the optical factor  $Q$  (that depends in its turn on the mirror losses) and to the size of the *RL*, by the factor  $L/A \propto 1/L$ . Increasing the dimension of the *RL* eventually results in more demanding requirements on the mirrors alignment and on the mechanical stability of the device. Variations of the environmental conditions during measurement processes on long timescales (hours) induce deformations of the optical cavity, enhancing the fluctuations of the correction terms in Eq.(2). The magnitude of those effects, which are mainly driven by temperature and pressure drifts, has been reported to be proportional to  $L$ . Therefore a trade off must be made between the minimization of intrinsic and systematic noise sources. The world's most sensitive *RLG G-WETTZELL*,

operated inside the geodetic station of *Wettzell*, in *Bavaria (GER)*, has an optical cavity length of  $L = 16$  m, and routinely achieves a sensitivity of few  $\mu\text{rad/s}$  at the frequency of 1 Hz. The optical cavity of *G-WETTZELL* has a monolithic design to minimize the effects of environmental drifts: it exploits an ultra-low expansion coefficient glass, named *Zerodur*, and a passive stabilization of the optical cavity length by means of a pressure vessel to control some residual mechanical deformations. On the other hand, in high sensitivity large size *RLGs* of etherolithic design, as the apparatus called *G-PISA*, operated at *LNGS* (the *INFN* laboratories of *Gransasso, Abruzzo (ITA)*), the mirrors are equipped with piezoelectric transducers to react against changes in their displacement, to constrain the geometry of the instrument. By this means, *G-PISA* is now 10 times less sensitive than *G-WETTZELL*, and up to 100 times less stable. Our analysis is focused on the latter type of *RLGs*, since the etherolithic design is the most promising to be adopted for the design of *RLGs* to test General Relativity. In fact, it is not economically nor technically affordable to build monolithic optical cavities bigger than the one of *G-WETTZELL*, and such bigger dimensions are required to obtain the desired Signal-to-Noise ratio. Further more in the monolithic design there is no way to account for the geometry of the *RL* with the accuracy required by the measure of the *Lense-Thirring* effect.

We have developed accurate models for the relevant dynamics of *RLGs*, then we estimate the rotation by identifying the relevant *RL* parameters, and applying an *Extended Kalman filter (EKF)*, which is able to recursively track the laser dynamics even in the presence of noise fluctuations. We have also developed models for the computation of the optical path in resonant cavities, and for the decomposition of shape and pose of a square optical cavity, to separately account for rigid its body motions and deformations.

We have shown that identification and dynamical filtering improve the response of large size *RLGs* as *G-WETTZELL*, which have already reached a precision of  $\sim 5$  part in  $10^9$  of the Earth rotation rate, providing so informations for geophysics and geodesy of paramount importance. Middle size rings, with sides of  $\sim 1$  m as *G-PISA*, which are more affected by backscattering, improved as well. Such measurements are more suitable for geophysics applications (i.e. rotational seismology) [76], and for application to the gravitational waves interferometers (e.g. local tilts measurements) [71].

## 1.2 OUTLINE OF THE THESIS

The thesis examines several aspects of stability and accuracy of high sensitivity *RLGs*, with particular attention to the etherolithic design, by means of the offline post-processing of the acquired interferogram

and intensities signals, and the active control of the geometry of the optical cavity.

In the Sections 1.3 and 1.4 the relevant literature on *RLs* is reviewed, and their use in General Relativity tests is outlined.

In Chapter 2 we develop a comprehensive model of the *RL* dynamics, and we devise methods for estimating the *Lamb* parameters: excess gain minus losses coefficients  $\alpha_{1,2}$ , scattering coefficients  $r_{1,2}$  and  $\varepsilon_{1,2}$ , self- and cross- saturation coefficients  $\beta_{1,2}$  and  $\theta_{12,21}$ , and scale factor and null shift errors  $\sigma_{1,2}$  and  $\tau_{12,21}$ , which depend in their turn from cavity losses  $\mu_{1,2}$ , plasma polarizability and single pass gain  $G$  of the laser medium. In addition, we estimate the round trip losses and the laser medium single pass gain, and set up a monitor of the gain. Exploiting these informations, we run an *EKF* which is able to remove from Earth rotation rate measurements a relevant fraction of the laser dynamics contributions. In this way we improved the long term stability and the accuracy of the rings *G-PISA* and *G-WETTZELL*, and demonstrated the effectiveness of non-linear *Kalman* filtering techniques in removing the systematics effects of light from the *RLG* output. A motivation for this part of our work is also to foresee a calibration procedure of high resolution *RLGs* which exploits the non linearity of laser active medium.

In Chapter 3 we address the model of the geometry of the optical cavity. Our results are twofold: *i)* we develop an algorithm to compute the beam steering of an optical cavity for given mirror position and alignment; and *ii)* we state the Shape and Pose Decomposition of four tridimensional points, representing the curvature centers of the *RL* spherical mirrors. On the one hand, this decomposition provides a straight way to model the geometry of the optical cavity of a square *RL*, on the other hand, it sets up an efficient and elegant framework for the active control of a *RL* cavity.

In Chapter 4 the models developed in the previous chapters are put together to obtain a complete simulation of an high resolution *RLG*, and a simulation case study is presented. Finally, conclusions are drawn in Chapter 5.

### 1.3 PREVIOUS & RELATED WORKS

Great attention has been paid by the scientific community to the applications, and hence to the accurate modeling and optimization of any aspect of the *RLG* design; for instance, the search in *Google Scholar* with key word “ring laser” shows more than 2.000.000 occurrences among scientific papers and patents. *RLs* have been successfully operated starting from the 50’s, and the first *RLG* was empirically demonstrated as rotational sensor in 1963 [47], almost a decade before a complete model for its operation was addressed in 1973 [49], following the publication of models for the standing wave and traveling

wave optical masers, in 1963 and 1965 [82, 7]. The interest for this optical device was strong enough to allow for a dedicated review of the *Sagnac* effect itself [52], where theoretical models for the *RLG* readout in Eq.(2) are discussed. Much work will be devoted from now on to the development of error models for *RLs*, both for the optimization of the design of these instruments and for the interpretation and offline post processing of the output signals.

*E. Lamb* [82, 49] and *F. Aronowitz* [7, 9] studied the dynamics of the gas lasers by developing a set of differential equations that describe the coupling between the radiation field and the atomic polarization at the third-order expansion, in terms of the so called *Lamb* parameters. The physical process, that for its complexity and empirical relevance, became object of great study and deep research, is the backscattering, which causes the lock-in phenomenon. In the optical cavity some light from one beam is scattered back and recombined with the light of the beam traveling in the opposite direction. The lock-in behavior is a dead zone effect for small rotations in the characteristic curve of a *RLG*. Ref.[25] is expressly dedicated to the clarification of the backscattering model developed by *Aronowitz*. Even larger instruments, in which the Earth rotation rate is a bias with enough magnitude to overcome the lock-in, have been reported to be limited in their sensitivity and stability by backscattering. The most common solution to the lock-in for small *RLGs*, that are not forced to work outside the dead zone only by the Earth rotation, is to mechanically dither the instrument with a known angular velocity. The authors of ref.[10] also review and exploit a formalism to deal with frequency multiplication and time-variant differential equations systems, named after *G. Floquet*, in order to make quantitative predictions for their experiments. Other recipes to overcome the lock-in problem consist in the application of a frequency bias by means of some non reciprocal effects, i.e. magnetic (*Kerr*) effect, non planarity, or polarized light.

The reviews [8, 30] offer a comprehensive treatment of the relevant aspects of the design and operation of a *RLG*, with particular attention to backscattering effects and the lock-in phenomenon. Even if the stochastic term in Eq.(2) is often negligible for the cases of interest, the dynamics of a *RL* with backscattering have been investigated also from a statistical point of view [23, 81]. *Mandell* and others [18, 19, 88, 16] derived approximated forms of the distribution of the state description of a *RL*, assuming the reciprocity of some of the *Lamb* parameters. Deterministic solutions allowing some non reciprocities were found by *A. Chyba* [20, 21], one of *Mandell* brightest Ph.D students. *Chyba* also reported some experimental investigations that motivated and demonstrated his theoretical analysis. Basing on these results, some others authors studied deeper the *RL* backscattering model from a stochastic point of view [51], having in mind investigations on laser physics [36, 70]. In ref.[22], stochastic analytic meth-

ods devised for periodic potentials were applied to the *RL* Langevin equations, and finally in ref.[68, 44] the nature of the symmetries that connect and break down in the operation of these instruments was investigated.

The mitigation of backscattering effects in high resolution *RLGs* is still an open research field, with many publications describing methods for the active mitigation of the backscattering [27, 12, 83, 50], or for its offline subtraction [29].

On another issue, the dependence of *RLs* on the spatial orientation and misalignment of the optical cavity mirrors has been object of detailed researches, too. In ref.[43, 4] the principles of Geometric and Gaussian Optics are applied for the first time to generic resonant optical cavities and then properly to *RLs*. Another article describes a procedure to align a *RLG* and ensure its operation [5]. Basing on these results other authors discussed the possibility to compensate the misalignments of the resonant optical cavity of a *RL* by means of mirror movements and frequency stabilization [26, 56]. *Rodloff* also remarkably noticed that by accomplishing the alignment one would also mitigate the effects of backscattering. The connection between backscattering and mirror misalignments was highlighted also by *Stedman*, that developed a model for the planar alignment of a *RL* [13] as well as a refinement of *Aronowitz* backscattering analysis [73]. Its review [72] is nowadays considered one of the best review concerning the Physics experiments available by means of *RLGs*.

However, for the design of high performances *RLGs* one must face to different shapes and tridimensional configurations of ring cavity, for this reason simulation tools were developed [78] and non planar configurations studied [67]. Advances in frequency and phase active enslavement and offline processing pushed further the possibilities of constrain the optical cavity [38], as well as to investigate the relation between *Lamb parameters* and misalignments [74]. Yuan and Long [87, 84, 86, 85] addressed the relevant questions we posed so far, and formalized a tridimensional extension of the usual planar *ABCD* ray matrix formalism to account for mirror tilts and translations in a cavity with tridimensional misalignments. The action of these matrices on the spatial profile of a gaussian beam has been elegantly formalized by means of matrix group theory [11]. Some authors addressed the initial alignment of monolithic optical cavities [45], some others studied the symmetries of some of the most common optical elements to be found in the *RL* cavity, i.e. spherical and flat mirrors [46]. Most recent articles in this research field includes design methods for optical cavities with regard to simplicity [54] and practical methods to heal the magnetic sensitivity of an optical cavity by means of non planar cavity deformations [17].

The commercial applications detailed in Section 1.1 are not representative of all the *RLG* applications. For instance a *RLGs* can be

employed in giving a precise definition of the standard unit in angular metrology [31], and also down-scaling the dimensions of a *RL* may have some interesting applications [28]. *U. Schreiber* and coworkers have addressed some remarkable applications concerning seismology, geodesy and geophysics operating the instrument *G-WETTZELL* [39, 66, 61, 65, 63, 60, 35, 59]. They demonstrated the observation of the *Chandler* and *Annual Wobble*, and other Earth signals, characterized the noise contributions in the frequency band suitable for geodetical and geophysical signals, and investigated some hardware upgrades for *G-WETTZELL* to overcome the residual stability limitations. We report on two Ph.D. thesis [33, 77] that has been elaborated by two students of the Schreiber research group. To review some of the applications of *RLGs* to seismology and geophysics we also report on ref.[40, 64, 62, 76] that analyze various Earth related signals (e.g. tidal tilts) in the measures of high resolution *RLGs*.

At the end of this review, we briefly report on the research group that has inspired, guided and supported the experimental work in this thesis. At the beginning, it was of paramount importance the *INFN* proposal to measure relativistic effects related to gravity by means of a tridimensional array of *RLs* [75, 14]. In order to accomplish this goal the construction of the etherolithic *RLG G-PISA* has been pursued, and some experimental investigations have been conducted [79, 14]. This research activity promoted two master thesis [24, 58], this Ph.D. thesis and four peer-review articles already published. In addition, two papers related to the innovative contribution of this thesis are currently under review.

#### 1.4 CURRENT AND FUTURE DEVELOPMENTS OF RLS

In the last years several applications of high resolution, stable, middle or large size *RLGs*, to many cutting edge research fields of Physics have been highlighted by the scientific community. We already discussed that the mechanical properties of these devices, together with their stability and sensitivity, fit *RLG* among the most precise sensors of Earth rotation. In the near future, the application of large frame (side  $> 1$  m) *RLs* is foreseen to improve the performances of advanced gravitational waves detectors [71]. Furthermore, the gravitational physics community has addressed the study of a *RLG* array with the aim of measuring a relativistic effect with the 1% of accuracy, and so providing a ground based test of General Relativity. The relativistic effect under study is the gravito-magnetic effect of the rotating Earth, named after the physicists *Lense* and *Thirring* [14, 75, 72].

*GINGER* (Gyroscopes IN GEneral Relativity) is an *INFN* proposal to measure the Lense-Thirring effect with an array of *RLs*. An underground location is essential for this challenging experiment, and the *LNGS* facility, located in the National Laboratories of the *Gransasso*

mountain, *Assergi (AQ)*, is a suitable location. *G-GranSasso-RD* is an experiment that has been financed by the *INFN* Commission II, which aims at the planning, installation and operation of *GINGER*. The *GINGER* project is considered to be the final outcome of an international collaboration with Germany and New Zealand, i.e. the institutes of the *TUM* University and the *Canterbury* University, prof. *U. Schreiber*, prof. *J.P. Wells* and their research groups.

The Italian group has developed two ring-laser prototypes, *G-PISA* and *GP2*, and both apparatus have an etherolithic design: *G-PISA* is the first prototype, a square ring with side length of 1.35 m. It is a transportable device, which so far has been installed in different locations, and with different orientations. *GP2* is the newest prototype (2014), at present installed in the *INFN* Laboratories of *S.Piero a Grado (PI)* and it was expressly designed to address the study of the geometry of the ring cavity and its active control. The preliminary tests done with *G-PISA* operated at the clean room of *S.Piero a Grado*, and at *LNGS*, showed the several advantages of the passive stabilization of the device provided by an underground location.

#### 1.4.1 *G-PISA and its experimental setup*

The *RLG G-PISA* consists in a square optical cavity with a side length of 1.350 m. The four cavity mirrors are contained in a steel vacuum chamber entirely filled with a *He – Ne* gas mixture. This design allows us to change the perimeter of the ring simply by changing the length of the tubes connecting the four cavity mirrors. In the middle of one side of the cavity is mounted a pyrex capillary, 4 mm in internal diameter and 150 mm in length. The capillary plays a double role: it acts as a diaphragm selecting the  $TEM_{00}$  spatial mode and it gives the possibility to apply a radio-frequency electric field for the laser excitation of the *He – Ne* plasma. The measurement of the *Sagnac* interferogram is obtained by combining the two output beams exiting one corner through an intensity beam splitter, while the single beam intensities are directly detected at the output of the adjacent corner. Two optically transparent windows are mounted on each corner of the cavity and allow to monitor the eight beams exiting the cavity. Two of the four mirrors are equipped with a piezo-transducer, which moves the mirror along a diagonal of the square. They are used to keep constant the perimeter of the ring allowing a continuous measurement of the angular velocity of the ring. In fact the *RLG* can be operated either free running or enabling the control loop of the perimeter. The perimeter is controlled by keeping the wavelength of one of the two modes of the *RL* constant, using a stabilized laser source as an external reference. For this purpose a Doppler-stabilized, single-frequency *He – Ne* laser associated with a *Lambda Meter LM-10* is employed.



Figure 2: *G-PISA* on top of its granite table, moved from its installation in S.Piero (Pisa).

Inside the dedicated area in the *LNGS* facilities *G-PISA* has been fixed to a granite table that, in its turn, is firmly attached to a special monument. The monument is made of reinforced concrete, which can support the *RLG* and its granite table in horizontal configuration. In this configuration, the *Sagnac* frequency due to the Earth rotation is about 104 Hz. Two broad-band seismometer and a tilt-meter, with  $\mu\text{rad}$  resolution in frequency below a mHz, have been installed on top of the granite table. The monument was not fixed to the ground, it was simply laying against the floor. Finally, simple acoustic and thermal shielding was constructed around the ring-laser: a simple box has been mounted around the apparatus, and the structure to hold the *stiferite* panels used for the acoustic shielding is also visible. The data acquisition is based on a *NI PXI* system.

Fig.2 shows the experimental set-up of *G-PISA*, attached to the granite table, horizontally oriented. The next installation of this *RLG* with augmented side length and renamed *GINGERino* has begun in Spring 2014, and likely we expect to have the device operating in the first months of 2015.

#### 1.4.2 *General Relativity Tests: the GINGER detector*

The theory of General Relativity is the pillar of contemporary understanding of matter, energy and space-time. The theory succeeds in explaining the behavior of the whole universe, as well as it fails to be



in accordance with quantum mechanics in the high energy domain. Anyway, also in the very low energy sector of the gravitational interaction there are predictions of General Relativity which have not been fully explored up to now. A typical example is the so called gravito-magnetic component of the gravitational field, i.e. the *Lense-Thirring* effect, whose direct verification relies for the moment on three experiments in space: Gravity Probe B; the two *LAGEOS* satellites orbital nodes analysis; and the *LARES* mission. Here we report that the expected accuracy in the *Lense-Thirring* effect detection for those experiments ranges from 10% to 2% [75].

Other evidence of gravito-magnetic effects may be found in the laser ranging of the orbit of the moon and on the study of the dynamics of binary systems composed of at least one compact massive object (neutron star) [53]. Moreover, some facts concerning galaxies motions and the dark matter theory have stimulated the idea that General Relativity might need some extensions. What matters here is that the phenomenology to look for is in the differences from empirical observations and General Relativity in the domain of low and ultra-low energies. All above said gives motivations for working experimentally on the gravitational interaction in the weak domain looking for post-Newtonian effects and Parametrized Post Newtonian descriptions which predict deviations from classical General Relativity.

Among various possible experimental approaches, a nearly perfect tool is represented by light. Light is indeed intrinsically relativistic and is affected in various ways by the gravitational field.

In the classical domain and treating space-time as a continuous four- dimensional Riemannian manifold, light completely covers the manifold with a network of null geodesics. If we can measure the local and global configuration of the null geodesics tissue we can reconstruct the gravitational field and see whether it fully corresponds to the General Relativity description or not. For a *RL* fixed on the Earth the General Relativity predicts a signal of the form

$$v_s = \frac{4A}{\lambda L} \left[ \boldsymbol{\Omega} - 2 \frac{\mu}{R} \boldsymbol{\Omega} \sin \theta \mathbf{u}_\theta + \frac{GJ_\oplus}{c^2 R^3} (2 \cos \theta \mathbf{u}_r + \sin \theta \mathbf{u}_\theta) \right] \cdot \mathbf{n}$$

where  $\boldsymbol{\Omega}$  is the angular velocity of the Earth,  $\theta$  is the colatitude of the laboratory,  $\mathbf{u}_r$  and  $\mathbf{u}_\theta$  are unit vectors that represent the azimuthal and north-south directions,  $\mu = GM_\oplus/c^2 \approx 4.4 \times 10^{-3} \text{m}$  is half of the *Schwarzschild* radius of the Earth, and  $M_\oplus$ ,  $J_\oplus$  and  $R$  are the mass, the angular momentum and the radius of the Earth, respectively. In summary: the *RL* beat note has 3 terms: *Sagnac*, *de Sitter* (Geodetic term) and *Lense-Thirring* (Gravito-magnetic).

Since the Earth angular velocity is independently measured with very high accuracy by the *VLBI* system, which measure the Earth rotation with respect to the fixed stars, the Relativistic terms can be

obtained by subtracting from the ring-laser data the *Sagnac* term measured by *VLBI*. For all these reasons the *RL* appears today as a most interesting apparatus to probe the structure of space- time at the laboratory scale.

## 2.1 PHYSICAL PRELIMINARIES AND RL SEMI-CLASSICAL TREATMENT

In the research field of high stability high resolution RLGs the 632.8 nm transition of the Helium Neon ( $He - Ne$ ) laser system is almost uniquely used [7, 9, 82, 49]. To improve both the stability and the accuracy of these instruments, it is of paramount importance to model the details of the stimulated emission process of the  $He - Ne$  media in non ideal optical cavities. In fact the subtleties of the ring laser dynamics are mainly related to the emission process in the  $He - Ne$  medium and to the dissipative and parasite processes taking place during light scattering on mirrors. The semi-classical treatment of the RL, introduced by Lamb, Aronowitz, et al. [7, 49], is a framework in which the laser radiations propagating in a closed path are modeled by

$$c^2 \frac{\partial^2 \mathcal{E}_i(s, t)}{\partial s^2} - \frac{\partial^2 \mathcal{E}_i(s, t)}{\partial t^2} + 2 \{ \hat{s} \cdot [\Omega(s, t) \times \mathbf{n}(s, t)] \} \frac{\partial^2 \mathcal{E}_i(s, t)}{\partial s \partial t} \quad (5)$$

$$= \frac{1}{\epsilon_0} \frac{\partial}{\partial t} [J_i(\mathcal{E}_{-n} \dots, \mathcal{E}_n, s, t) + P_i(\mathcal{E}_{-n} \dots, \mathcal{E}_n, s, t)] , i \in \mathbb{N} \quad (6)$$

Eq.(5) is the component of a set of coupled *Maxwell-Bloch* equations, where the index  $i$  is an integer number positive for clock-wise traveling waves and negative for anti-clockwise ones: the state of the system  $\mathcal{E}_i(s, t)$  is the value of the electromagnetic field polarized along the direction perpendicular to the optical cavity plane, traveling in the clockwise + and counter-clockwise - direction. The electromagnetic field represented by a complex number is dependent on both time  $t$  and the spatial coordinate on the cyclic path  $s$ . Here  $\hat{s}$  is the vectorized optical path parametrized in  $s$ ,  $\Omega$  is the Earth rotation rate vector,  $\mathbf{n}$  is the unit vector of the vectorial area of the optical cavity,  $c$  is the light speed,  $\epsilon_0$  is the dielectric constant of vacuum,  $J_i$  is an Ohmic current accounting for dissipative and scattering effects due to light reflection transmission and absorption, and  $P_i$  is the effect of the electric polarization of the active media on the laser mode labeled by  $\mathcal{E}_i$ .

The resulting system of equations can be solved by using variables separation, within the *WKB* approximation [49]. The *WKB* approximation is a method for finding approximate solutions to partial differential equations. The electric fields are recast as series of complex

exponential functions, and then expanded assuming that amplitudes and phases are slowly varying with respect to the eigenfrequencies of the system. The polarizations and the currents are then expanded in terms of the exponential functions, becoming functions of the slowly varying amplitudes and phases. Within the small gain approximation, i.e. when the laser is not excited far above threshold, the series are truncated at the third order in powers of the fields, retaining a good accuracy in the resulting model.

### 2.1.1 *RL equations: complex fields*

The hypothesis made on Maxwell-Bloch equations fit the usual working regime of high resolution *RLGs*, which is obtained with a gain starvation approach, where only the fundamental lasing mode *TEM00* is excited in both the directions of propagations, labeled with 1 and 2 for clockwise and counter-clockwise traveling waves, respectively. Therefore the ordinary differential equation system for the slowly varying amplitudes and phases of the two lasing modes reads

$$\begin{aligned}\dot{E}_1(t) &= (\mathcal{A}_1 - \mathcal{B}_1|E_1(t)|^2 - \mathcal{C}_{12}|E_2(t)|^2) E_1(t) + \mathcal{R}_2 E_2 \\ \dot{E}_2(t) &= (\mathcal{A}_2 - \mathcal{B}_2|E_2(t)|^2 - \mathcal{C}_{21}|E_1(t)|^2) E_2(t) + \mathcal{R}_1 E_1\end{aligned}\quad (7)$$

The amplitudes and phases are collected in the complex quantities  $E_1$  and  $E_2$ , the parameters  $\mathcal{A}_1, \mathcal{B}_1, \mathcal{C}_{12}, \mathcal{R}_1$ , and for the opposite traveling wave,  $\mathcal{A}_2, \mathcal{B}_2, \mathcal{C}_{21}, \mathcal{R}_2$ , account for the aggregate effect of amplification, saturation, absorption, transmission, and reflection in the optical cavity of a *RL*.

By introducing the 2-dimensional vector complex valued function  $\mathbf{E}(t) = (E_1, E_2)^T$ , Eqs.(7) can be write in matricial form

$$\dot{\mathbf{E}} = \left[ \mathbf{A} - \mathcal{D}(\mathbf{E}) \cdot \mathbf{B} \cdot \mathcal{D}(\mathbf{E}^*) \right] \mathbf{E}, \quad (8)$$

where we have defined the complex-valued matrices

$$\mathbf{A} \equiv \begin{pmatrix} \mathcal{A}_1 & \mathcal{R}_2 \\ \mathcal{R}_1 & \mathcal{A}_2 \end{pmatrix}, \quad \mathbf{B} \equiv \begin{pmatrix} \mathcal{B}_1 & \mathcal{C}_{21} \\ \mathcal{C}_{12} & \mathcal{B}_2 \end{pmatrix}, \quad (9)$$

accounting for the linear and quadratic field interactions, and the auxiliary field matrix

$$\mathcal{D}(\mathbf{E}) \equiv \begin{pmatrix} E_1 & 0 \\ 0 & E_2 \end{pmatrix}. \quad (10)$$

$\gamma_a$	12 MHz
$\gamma_b$	127 MHz
$\gamma_{ab}$	234 MHz
$\mu_{ab}$	$3.2 \cdot 10^{-30} \text{C m}$

Table 1: *He – Ne* laser system parameters.2.1.2 *RL equations: real variables*

Eqs.(7) or Eq.(8) can be transformed into a real 4 components equations system by considering the light intensities normalized in *Lamb* units

$$I_{1,2}(t) = \frac{|\mu_{ab}|^2(\gamma_a + \gamma_b)}{4\hbar^2\gamma_a\gamma_b\gamma_{ab}} |E_{1,2}(t)|^2,$$

and the phases  $\phi_{1,2}(t) = \angle E_{1,2}(t)$ , where

$$|\mu_{ab}| = \sqrt{\pi\epsilon_0 \frac{\lambda^3}{(2\pi)^3} \hbar A_{ik}}$$

is the electric dipole moment between states  $a = 3s^2$  and  $b = 2p^4$  (i.e. the upper and the lower of the laser energy levels),  $\gamma_a$  and  $\gamma_b$  are the decay rates in *Paschen* notation,  $\hbar$  is the reduced *Planck* constant,  $A_{ik}$  is the radiative decay rate between the laser levels, and  $\epsilon_0$  is the dielectric constant of vacuum. The Table 1 contains the reference values of the above quantities for a *Doppler* broadened active medium in presence of collisions.

Since the dynamics of the monobeam intensities  $I_{1,2}(t)$  and of the *Sagnac* phase  $\psi(t) = \phi_1(t) - \phi_2(t)$  are autonomous, i.e. not influenced by the quantity  $\phi_1(t) + \phi_2(t)$ , we retain the system of 3 differential equations [7, 9]

$$\frac{\dot{I}_1(t)}{I_1(t)} = \alpha_1 - \beta_1 I_1(t) - \theta_{12} I_2(t) + 2r_2 \sqrt{\frac{I_2(t)}{I_1(t)}} \cos(\psi(t) + \varepsilon_2) \quad (11)$$

$$\frac{\dot{I}_2(t)}{I_2(t)} = \alpha_2 - \beta_2 I_2(t) - \theta_{21} I_1(t) + 2r_1 \sqrt{\frac{I_1(t)}{I_2(t)}} \cos(\psi(t) + \varepsilon_1) \quad (12)$$

$$\dot{\psi}(t) = \omega_s + \sigma_1 - \sigma_2 + \tau_{21} I_1(t) - \tau_{12} I_2(t) + \dots \quad (13)$$

$$+ r_1 \sqrt{\frac{I_1(t)}{I_2(t)}} \sin(\psi(t) + \varepsilon_1) + r_2 \sqrt{\frac{I_2(t)}{I_1(t)}} \sin(\psi(t) + \varepsilon_2), \quad (14)$$

where the real valued parameters  $\alpha_{1,2}$ ,  $\beta_{1,2}$ ,  $\theta_{12,21}$ ,  $\omega_s$ ,  $\sigma_{1,2}$ ,  $\tau_{12,21}$ ,  $r_{1,2}$ , and  $\varepsilon_{1,2}$  are related to the complex ones  $\mathcal{A}_{1,2}$ ,  $\mathcal{B}_{1,2}$ ,  $\mathcal{C}_{21,12}$ ,  $\mathcal{R}_{1,2}$  by the relations

$$\begin{cases} \mathcal{A}_{1,2} = \frac{c}{L} \left( \frac{\alpha_{1,2}}{2} \pm i \frac{\omega_s + \sigma_{1,2}}{2} \right) \\ \mathcal{B}_{1,2} = \frac{c}{L} \sqrt{\frac{|\mu_{ab}|^2 (\gamma_a + \gamma_b)}{4\hbar^2 \gamma_a \gamma_b \gamma_{ab}}} \beta_{1,2} \\ \mathcal{C}_{12,21} = \frac{c}{L} \sqrt{\frac{|\mu_{ab}|^2 (\gamma_a + \gamma_b)}{4\hbar^2 \gamma_a \gamma_b \gamma_{ab}}} (\theta_{12,21} - i\tau_{12,21}) \\ \mathcal{R}_{1,2} = \frac{c}{L} r_{1,2} e^{i\varepsilon_{1,2}} \end{cases}, \quad (15)$$

recall that  $L$  is the length of the optical cavity, the ratio  $c/L$  is called free spectral range of the optical cavity and it is a very important design parameter for a *RL*. Here  $\omega_s$  is the *Sagnac* frequency,  $\alpha_{1,2}$  are the excess gain minus losses coefficients,  $\beta_{1,2}$  are the self saturation coefficients,  $\theta_{12,21}$  are the cross saturation coefficients,  $\sigma_{1,2}$  the frequency error coefficients,  $\tau_{12,21}$  are the null shift error coefficients,  $r_{1,2}$  are the backscattering amplitude coefficients and  $\varepsilon_{1,2}$  are the backscattering angles.

### 2.1.3 *RL standard outputs*

The most important measured signal for *RLs* is the interferogram, i.e. the signal obtained combining on a photo-diode the two beams transmitted through a mirror. The intensities of both beams are also separately acquired with other photo-diodes on another mirror. In this description only one measure for sampling time of the beat signal and of the intensities is considered, moreover we are not accounting for the dynamics of the amplification stages, as they are faster ( $\sim 10^4$  Hz) than the characteristic frequencies of the system ( $\sim 10^2$  Hz) [79]. The vector collecting all the outputs of the system at the time intervals  $kT_s$  reads

$$\mathbf{y}(k) = \begin{pmatrix} V_1(k) \\ V_2(k) \\ S(k) \end{pmatrix} + \mathbf{w}(kT_s), \quad (16)$$

where  $T_s$  is the sampling time, the vector  $\mathbf{w}$  represents a white noise stochastic process, and

$$\begin{cases} V_1(k) = c_1 I_1(kT_s) \\ V_2(k) = c_2 I_2(kT_s) \\ S(k) = c_3 |h_1 E_1(kT_s) + h_2 E_2(kT_s)|^2 \end{cases}; \quad (17)$$

here the constants  $c_i$  and  $h_i$  are real numbers which account for photodetectors characteristics. It is worth mentioning that the parameters  $c_i$  and  $h_i$  are also related to parameters of the electronic amplification and digital conversion stages, and hence they may drift as the envi-

ronmental conditions change. The interferogram signal  $S(kT_s)$  can be recast as

$$S(k) = c_3 h_1^2 I_1(kT_s) + c_3 h_2^2 I_2(kT_s) + 2c_3 h_1 h_2 \sqrt{I_1(kT_s) I_2(kT_s)} \cos(\psi(kT_s)). \quad (18)$$

Here we anticipate that the steady state intensities  $I_{1,2}$  are usually in the form of constant signals plus small modulations, so the phase information in the interferogram is, at a first approximation, introduced only by  $\psi(kT_s)$ . For this reason the interferogram signal is regarded as the most important signal in the estimation of rotation rates by means of *RLGs*. To estimate  $\cos(\psi(kT_s))$  directly from  $S(kT_s)$ , the linear trend  $c_3 h_1^2 I_1(kT_s) + c_3 h_2^2 I_2(kT_s)$  is removed, and the scale  $2c_3 h_1 h_2 \sqrt{I_1(kT_s) I_2(kT_s)}$  is normalized to 1 over time intervals which usually correspond to thousands of cycles. We stress that in general, if we allow the intensities to have oscillatory parts, the interferogram phase information is not given only by the oscillations of the *Sagnac* phase. In fact oscillatory components would arise also from the non-linear coupling between intensities, from the coupling between intensities and the *Sagnac* phase, and finally from the addition of the intensity signals. Therefore to estimate the *Sagnac* frequency of a *RLG* one would need information on the full *RL* system state. This has often been misunderstood by the scientific community, which regarded to the interferogram as the main output of the instrument, and to the intensities as sort of auxiliary signals.

## 2.2 PARAMETERS OF RL DYNAMICS

We already noted that the *RL* equations depend on two sets of parameters with distinct physical origin: *i*) cold cavity parameters associated to dissipative and parasite scattering effects; and *ii*) active medium parameters associated to atomic polarizability.

Correspondingly, the *RL* matrices in Eq.(9) can be written as

$$\mathbf{A} \equiv \frac{c}{L} \mathbf{P}^{(0)} - \mathbf{M} \quad , \quad (19)$$

$$\mathbf{B} \equiv \frac{c}{L} \mathbf{P}^{(2)} \quad (20)$$

where  $\mathbf{P}^{(0)}$  and  $\mathbf{P}^{(2)}$  are the 0-th and 2-nd order contributions to the gas mixture polarizability and  $\mathbf{M}$  is the dissipative linear coupling matrix.

## 2.2.1 Laser medium parameters

We now address to the study of the parameters related to *He – Ne* laser system (Atomic Polarizability) avoiding the “Doppler limit” approximation usually made by *Aronowitz* [7]. The polarization  $P$  in Eq.(5) is presented for the case of two opposite traveling *TEM00* beams. This leads to the terms  $\mathbf{P}^{(0)}$  and  $\mathbf{P}^{(2)}$  in the matrices  $\mathbf{A}$  and  $\mathbf{B}$  of Eqs.(8),(19) and (20). The matrices  $\mathbf{P}^{(0)}$  and  $\mathbf{P}^{(2)}$  are given by

$$\mathbf{P}^{(0)} = \frac{G}{2} \begin{pmatrix} z^{(0)}(\xi_1) & 0 \\ 0 & z^{(0)}(\xi_2) \end{pmatrix}, \quad \mathbf{P}^{(2)} = G \begin{pmatrix} z_s^{(2)}(\xi_1) & z_c^{(2)}(\xi_{1,2}) \\ z_c^{(2)}(\xi_{1,2}) & z_s^{(2)}(\xi_2) \end{pmatrix}, \quad (21)$$

where  $G$  is the laser single pass gain, and  $z^{(0)}(\xi_{1,2})$ ,  $z_s^{(2)}(\xi_{1,2})$  are functions related to the atomic polarization which depends on the detunings of the optical frequencies to the cavity center frequency  $\xi_{1,2}$ . The typical values of  $z^{(0)}(\xi_{1,2})$ ,  $z_s^{(2)}(\xi_{1,2})$ , and  $z_c^{(2)}(\xi_{1,2})$  for the *RL G-PISA* tuned at the maximum of the gain profile, are listed in Tab.2.

$z^{(0)}(\xi_{max})$	$0.878 - 0.011 i$
$z_s^{(2)}(\xi_{max})$	$1.107$
$z_c^{(2)}(\xi_{max})$	$0.413 + 0.04 i$
$z_{ms}^{(2)}(\xi_{max})$	$0.403 - 1.893 i$
$z_{mc}^{(2)}(\xi_{max})$	$0.154 + 0.033 i$

Table 2: Complex value of the polarization contributions as expressed in Eq.(28) and Eq.(32) for the clockwise wave calculated at a detuning  $\xi_{max} = 0.05$  with respect to the center of the absorption profiles of  $^{20}\text{Ne}$  and  $^{22}\text{Ne}$ .

The complex valued functions  $z^{(0)}(\xi_{1,2})$ ,  $z_s^{(2)}(\xi_{1,2})$ , and  $z_c^{(2)}(\xi_{1,2})$  which allow us to estimate self- and cross- saturation parameters are rather common in plasma physics, and were calculated for the first time by *Aronowitz* with two counter-propagating laser beams [7]. His model of plasma requires that the ratio  $\eta$  between homogeneous  $\gamma_{ab}$  and inhomogeneous  $\Gamma$  broadening line width is  $\eta \equiv \gamma_{ab}/\Gamma \ll 1$ . For instance, in the experiment of ref. [9], the typical value of  $\eta$  is  $\simeq 10^{-2}$ . For gas mixtures with pressure  $4 \div 8$  mbar and temperature  $300 \div 500$  K, as in *G-PISA*, we have instead  $0.2 \leq \eta \leq 0.5$  and so we must perform a more general calculation of the atomic polarization. However, we will follow the approach of *Aronowitz* for what concerns the series expansion in powers of the electric fields describing the interaction between radiation and atoms. *Aronowitz* showed that the complex polarization of the active medium in a gas *He – Ne* laser, expanded to the third order in the field amplitude, can be written in the following integral form



$$\mathcal{P}^{(3)}(E_{1,2}) = -\frac{2i|\mu_{ab}|^2 E_{1,2}}{\gamma_{ab}} \int_0^\infty \chi_{1,2}^s(v) \rho^{(2)}(v, E_{1,2}) dv, \quad (22)$$

where  $|\mu_{ab}|$  is the electric dipole moment between states  $a$  and  $b$ ,  $\gamma_{ab}$  is the homogeneous line width,  $v$  is the velocity of atoms,  $\chi_{1,2}^s(v) = 1/(i\eta + \xi_{1,2} \pm v/u)$  is the complex susceptibility,  $u$  is the atomic mass constant, and

$$\rho^{(2)}(v, E_{1,2}) = \frac{N e^{-\frac{v^2}{u^2}}}{2\gamma_a\gamma_b\hbar\Gamma} \left( 1 - I_1 \frac{1}{1 + (\xi'_1 + v/u)^2} \right) \quad (23)$$

$$- \frac{\gamma_a + \gamma_b}{\gamma_{ab}} I_2 \frac{1}{1 + (\xi'_2 - v/u)^2} \quad . \quad (24)$$

is the second order population inversion. Here  $\gamma_a$  and  $\gamma_b$  are the decay rates of the upper and lower energy level,  $N$  is the average excitation inversion density,  $I_{1,2}$  are the normalized light intensities of  $E_{1,2}$  expressed in *Lamb* units, and  $\xi'_{1,2} = (\omega_0 - \omega_{1,2})/\gamma_{ab}$  is the frequency detuning to the natural line width ratio,  $\omega_{1,2}$  are the mode frequencies, and  $\omega_0$  is the gain center frequency. It is worth mentioning that the polarization depends on both amplitudes and frequencies of the electrical fields. After a decomposition in simple fractions of the rational part of Eq.(23), the integral in Eq.(22) can be conveniently evaluated by means of the plasma dispersion function

$$\begin{aligned} \mathcal{Z}(y) &\equiv \mathcal{Z}_R(y) + i\mathcal{Z}_I(y) = \\ &= \frac{1}{\sqrt{\pi}} \int_{\mathbb{R}} \frac{e^{-x^2}}{x - i\eta - y} dx = \\ &= i\sqrt{\pi} e^{-(\eta - iy)^2} \operatorname{erfc}(\eta - iy) \quad , \end{aligned}$$

where  $\operatorname{erfc}(\cdot)$  is the complementary error function, and  $\mathcal{Z}_R$  and  $\mathcal{Z}_I$  are the real and imaginary parts of the plasma dispersion function, and are proportional to the spectral gain and dispersion profiles of the unsaturated active medium, respectively.

The expression for the atomic polarization up to the 3-rd order approximation reads

$$\begin{aligned} \mathcal{P}^{(3)}(E_{1,2}) &\equiv \chi(E_{1,2}) E_{1,2} \quad (25) \\ &= \frac{\sqrt{\pi} A \mathcal{Z}_I(0)}{\gamma_{ab}\gamma_a\gamma_b} \left( z^{(0)}(\xi_{1,2}) - z_s^{(2)}(\xi_{1,2}) I_{1,2} - z_c^{(2)}(\xi) I_{2,1} \right) E_{1,2} \quad (26) \end{aligned}$$

where  $\chi(E_{1,2})$  is the cavity atomic polarizability,  $A = N|\mu_{ab}|^2/(\hbar\Gamma)$ ,

$$\begin{cases} z^{(0)}(\xi_{1,2}) = \frac{\mathcal{Z}(\xi_{1,2})}{\mathcal{Z}_I(0)} \\ z_s^{(2)}(\xi_{1,2}) = \frac{\mathcal{Z}_I(\xi_{1,2})(1 - 2\eta(\eta + i\xi_{1,2}))}{\mathcal{Z}_I(0)} + \\ \quad + \frac{2\eta - 2\eta\mathcal{Z}_R(\xi_{1,2})(i\eta - \xi_{1,2})}{\mathcal{Z}_I(0)} \\ z_c^{(2)}(\xi) = \frac{\gamma_a + \gamma_b\eta}{\gamma_{ab}} \frac{\eta}{\xi} \frac{\overline{\mathcal{Z}}_I(\xi)\xi - \overline{\mathcal{Z}}_R(\xi)\eta - \overline{\mathcal{Z}}_i(\xi)(\xi - i\eta)}{\mathcal{Z}_I(0)(\eta + i\xi)} \end{cases}, \quad (27)$$

and  $\xi_{1,2} = \pm(\omega - \omega_{1,2})/\Gamma$  is the frequency detuning to the *Doppler* width ratio,  $\overline{\mathcal{Z}}_I = [\mathcal{Z}_I(\xi_1) + \mathcal{Z}_I(\xi_2)]/2$ ,  $\overline{\mathcal{Z}}_R = [\mathcal{Z}_R(\xi_1) + \mathcal{Z}_R(\xi_2)]/2$ ,  $\overline{\mathcal{Z}}_i = [\mathcal{Z}_I(\xi_1) - \mathcal{Z}_I(\xi_2)]/2$ . Using Eq.(25), the expression of r.h.s. of Eq.(21), (8) can be identified with the coefficients of  $z^{(0)}(\xi_{1,2})$ ,  $z_s^{(2)}(\xi_{1,2})$  and  $z_c^{(2)}(\xi_{1,2})$  of Eq.(27), except for the constant laser single pass gain  $G$ .

In our calculations we must take into account that usually a *RL* cavity is filled with a gas mixture of two Neon isotopes. Thus the matrix elements of Eq.(21) must be substituted by

$$\begin{cases} z^{(0)}(\xi_{1,2}) = k' z^{(0)}(\xi'_{1,2}) + k'' z^{(0)}(\xi''_{1,2}) \\ z_s^{(2)}(\xi_{1,2}) = k' z_s^{(2)}(\xi'_{1,2}) + k'' z_s^{(2)}(\xi''_{1,2}) \\ z_c^{(2)}(\xi) = k' z_c^{(2)}(\xi') + k'' z_c^{(2)}(\xi'') \end{cases}, \quad (28)$$

where the symbols ' and '' refer to the  $^{20}\text{Ne}$  and  $^{22}\text{Ne}$  isotopes,  $k'$  and  $k''$  are the fractional amount of each isotope, and  $\xi'_{1,2}$ ,  $\xi''_{1,2}$  are the detuning to the center frequency of each isotope. Practically, the values of  $\eta$ ,  $\xi$  and  $k$  are rescaled by the square root of the ratio of the atomic mass of the two isotopes. As an example, we show in Fig.3 the polarization of a 50-50  $^{20}\text{Ne}$ - $^{22}\text{Ne}$  gas mixture as the sum of contributions arising from each Ne isotope, according to Eq.(28).

It is worth noticing that in the standard *RL* operation where the rotational frequency is negligible respect to the modes frequencies of the cavity,  $|\xi_1 - \xi_2| \lesssim 10^{-7}$ , consequently the difference between the polarization contributions for the 1 and 2 beams is very small,  $|z^{(0)}(\xi_1) - z^{(0)}(\xi_2)| \lesssim 10^{-6}$ . Therefore we will use the approximations  $\mathcal{B}_1 \simeq \mathcal{B}_2 = \mathcal{B}$ , from now on, by discarding the pedices 1,2.

### 2.2.1.1 Multimode saturation coefficients

We address to the problem of calculating the cross-saturation coefficients  $z_{ms}^{(2)}(\xi)$ ,  $z_{mc}^{(2)}(\xi)$  for two multimode counter-propagating waves  $E_{3,4}$ , lasing at  $\xi_{3,4} = \xi_{1,2} + nc/L$ ,  $n \in \mathbb{Z}$ , that arise at multimode transition of a *RL*.

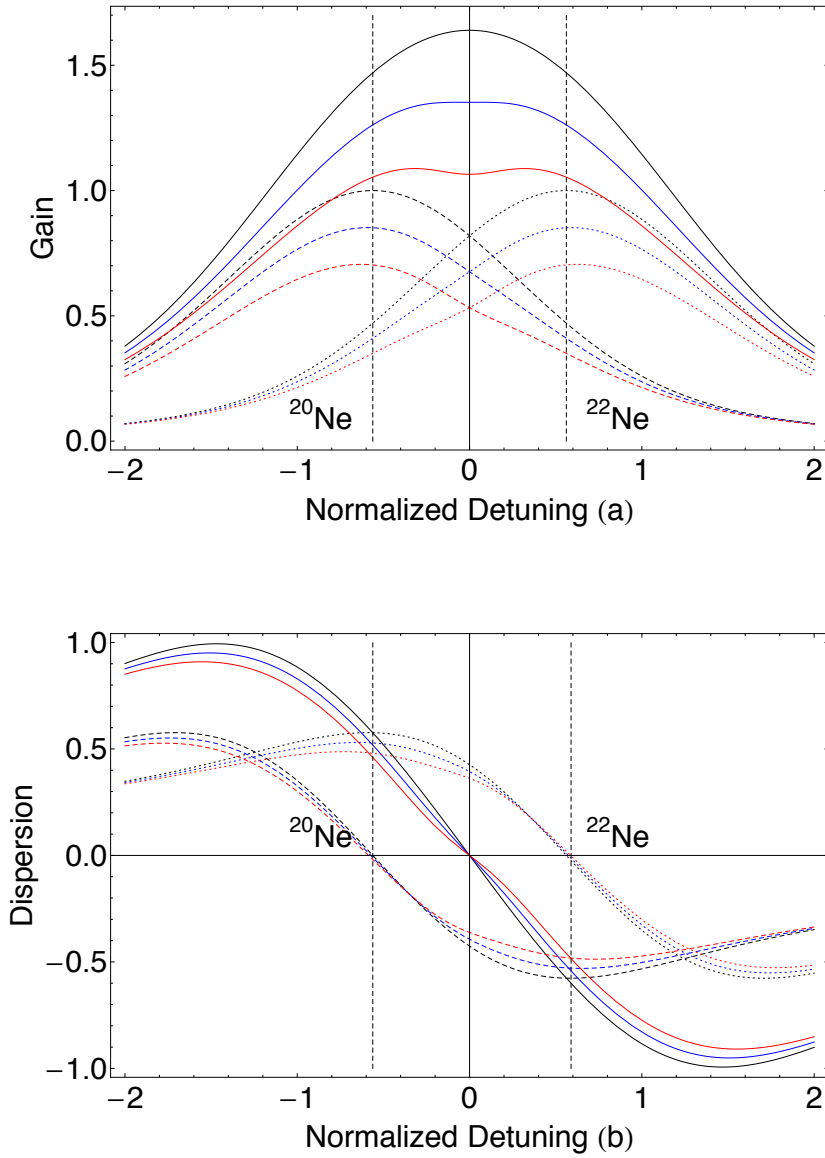


Figure 3: Plot of the computed gain (a) and dispersion (b) profiles of the plasma polarizability in the  $RL$  cavity (continuous line), and of its contributions from  $^{20}\text{Ne}$  isotope (dashed line), and  $^{22}\text{Ne}$  isotope (dotted line), assuming  $I_1 = I_2 = I$ . The black lines represent the unsaturated profile ( $I \rightarrow 0$ ), the blue and red lines represent profiles saturated by signals of intensity  $I = 0.1$ , and  $I = 0.2$ , respectively. The vertical dashed lines indicate the centers of the broadening profiles of the Ne isotopes.

The polarization components for the waves  $E_{3,4}$  at multimode threshold is given by Eq.(22), provided that the subscript 1,2 is substituted with 3,4, and  $\rho^{(2)}(v, E_{1,2})$  is replaced with the following expression

$$\rho_m^{(2)}(v, E_{1,2}) = \frac{Ne^{-\frac{v^2}{\Gamma^2}}}{2\gamma_a\gamma_b\hbar\Gamma} \left( 1 - \frac{\gamma_a + \gamma_b}{\gamma_{ab}} I_1 \frac{1}{1 + (\xi_3 - f_m + v/u)^2} \right) \quad (29)$$

$$- \frac{\gamma_a + \gamma_b}{\gamma_{ab}} I_2 \frac{1}{1 + (\xi_4 - f_m - v/u)^2} \quad (30)$$

where  $f_m = nc/(L\Gamma)$ . The expression for the multimode atomic polarization reads

$$\mathcal{P}^{(3)}(E_{3,4}) = \frac{\sqrt{\pi}A\mathcal{Z}_I(0)}{\gamma_{ab}\gamma_a\gamma_b} E_{3,4} \left( z^{(0)}(\xi_{3,4}) - z_{ms}^{(2)}(\xi_{3,4})I_{1,2} - z_{mc}^{(2)}(\xi)I_{2,1} \right) , \quad (31)$$

where

$$\begin{cases} z_{ms}^{(2)}(\xi_{3,4}) = \frac{2\eta^2 \frac{\gamma_a + \gamma_b}{\gamma_{ab}} \frac{\mathcal{Z}(\xi_{3,4} - f_m) - \mathcal{Z}(\xi_{3,4})^*}{f_m(i f_m + \eta)\mathcal{Z}_I(0)}}{2} \\ z_{mc}^{(2)}(\xi_{3,4}) = \frac{\eta}{\xi - \frac{f_m}{2}} \frac{\gamma_a + \gamma_b}{\gamma_{ab}} \frac{(\xi - \frac{f_m}{2})\mathcal{Z}_I(\xi_{4,3} - f_m) - \frac{\eta}{2}(\mathcal{Z}(\xi_{4,3} - f_m) + \mathcal{Z}(\xi_{3,4})^*)}{\mathcal{Z}_I(0)(\eta + i(\xi - \frac{f_m}{2}))} \end{cases} \quad (32)$$

In addition, for the cross saturation coefficients between 1 and 2 modes of fundamental and  $m$ -th mode, we have

$$\begin{cases} \theta_{31,42} = \text{Re} \left[ z_s^{(2)}(\xi_{3,4}) \right] \\ \theta_{32,41} = \text{Re} \left[ z_c^{(2)}(\xi_{3,4}) \right] \end{cases} \quad (33)$$

When more than one isotope is present in the gas mixture, one must modify Eqs.(32) using the weighted average of each isotope contribution, as in Eqs.(28). As a final remark, we note that, for large RL sensing the Earth rotation, the difference between the normalized detunings of each  $m$ -mode is very small, e.g.  $|z^{(0)}(\xi_3) - z^{(0)}(\xi_4)| \lesssim 10^{-6}$ . Consequently, the following approximation holds

$$\begin{cases} z_{ms}^{(2)}(\xi_{3,4}) \sim z_{ms}^{(2)}\left(\frac{\xi_3 + \xi_4}{2}\right) \\ z_{mc}^{(2)}(\xi_{3,4}) \sim z_{mc}^{(2)}\left(\frac{\xi_3 + \xi_4}{2}\right) \end{cases} \quad .$$

### 2.2.2 Dissipative parameters

In contraposition with the active medium parameters, the dissipative parameters are characteristics of the mirrors, and account for light scattering inside the optical cavity. Since the effects described by these parameters are dissipative effects, no detailed physical model for their

calculation exists. For this reason the values of the dissipative parameters of a *RL* must be determined directly from the measured output signals, in an identification framework. The elements of the linear coupling matrix  $\mathbf{M}$  are

$$\mathbf{M} = \begin{pmatrix} \frac{c}{L} \frac{\mu_1}{2} + i\omega_1 & -\frac{c}{L} r_2 e^{i\varepsilon_2} \\ -\frac{c}{L} r_1 e^{i\varepsilon_1} & \frac{c}{L} \frac{\mu_2}{2} + i\omega_2 \end{pmatrix}, \quad (34)$$

where  $\omega_{1,2} = \Omega_{1,2} - \omega_r + \frac{c}{L} \sigma_{1,2}$ ,  $\mu_{1,2}$  are the cavity losses,  $r_{1,2}$  are the backscattering coefficients and  $\varepsilon_{1,2}$  are the backscattering phases.

The effects of these parameters in the dynamics of a *RL* is to account for light scattering, each dissipative parameter is given by the sum of contributions representing the cavity dissipative sources, e.g. the mirrors. We stress that, in the case of an optical cavity with additional scattering centers, the additional centers must be taken into account to compute the dissipation parameters.

In Eq.(5) the complex current  $J$ , acting as a source, accounts for dissipations. For the two fundamental counterpropagating laser modes the latter current reads

$$J(E_{1,2}) = \sigma_{1,2}^s E_{1,2} + \delta_{1,2}^s E_{2,1} \quad (35)$$

where the self interaction coefficients  $\sigma_{1,2}^s$  are reals, and the cross interaction coefficients  $\delta_{1,2}^s$  are complex numbers. A non zero imaginary part of  $\sigma_{1,2}^s$  can account for a flow of the gas atoms in the ring cavity, that lead to corrections to the nominal value of the frequency difference between the two beams. This effect is called *Langimur* flow, and it has been previously reported and studied in the literature [82, 7]. This flow effect has been reported to be caused by asymmetries in the geometry of the radio-frequency circuit of the *RL*. For modern high sensitivity sensors this effect is carefully avoided, and the imaginary parts of  $\sigma_{1,2}^s$  will not be considered in our treatment.

### 2.2.2.1 Mirror losses

During the process of light reflection on mirrors in the optical cavity a small portion of the laser light is transmitted, absorbed and scattered. The coefficients  $\mu_{1,2}$ , which are proportional to the self interaction coefficients  $\sigma_{1,2}^s$ , accounts for all these light losses in the *RL* model [49]. Those quantities are also related to the optical quality factor  $Q$  of the *RL* cavity by

$$Q_{1,2} = \frac{4c}{L\mu_{1,2}} = \omega\tau_{1,2},$$

where  $\tau_{1,2}$  is the average decay time of photons in the cavity. For super-mirrors of modern manufacture the losses are of the order of some part per million, providing modern high sensitivity *RLGs* with side  $\sim 1$  m with quality factors  $\sim 10^{13}$ .

### 2.2.2.2 Backscattering coefficients

In the optical cavity, during *RL* operation, part of the light lost in the former reflection processes is scattered from one beam to the opposite traveling one. This retro-reflection is called backscattering. The backscattering is modeled by the coefficients  $r_{1,2}$ , representing the relative amount of light scattered from beam 1,2 in the direction of propagation of the beam 2,1, and the phases  $\epsilon_{1,2}$ , representing the relative phase shift between the backscattered and opposite traveling beams [73]. If the *RL* is provided with  $n$  mirrors, we can decompose the backscattering parameters as

$$r_{1,2}e^{i\epsilon_{1,2}} = \sum_{j=1}^n \rho_{1,2}^{(j)} e^{\left(\frac{2\pi i l_j}{\lambda} + \epsilon_{1,2}^{(j)}\right)}, \quad (36)$$

where  $\lambda$  is the laser wavelength,  $l_j$  are the optical paths between consecutive scattering centers, and  $\rho_{1,2}^{(j)}$  and  $\epsilon_{1,2}^{(j)}$  are the local backscattering amplitudes and phases of the  $j$ -th scattering center.

## 2.3 STUDY OF RL DYNAMICS

Some insights are gained by writing Eqs.(12) in the new coordinates  $\mathbf{I} = (I_1, I_2)^T$ , and  $X = \log(I_1/I_2) \psi$ , as

$$\begin{cases} \frac{d}{dt} \log(\mathbf{I}) &= 2\text{Re} \left[ \begin{pmatrix} \mathcal{A}_1 \\ \mathcal{A}_2 \end{pmatrix} - \mathbf{B} \cdot \mathbf{I} + \begin{pmatrix} \mathcal{R}_2 e^{-X} \\ \mathcal{R}_1 e^X \end{pmatrix} \right] \\ \frac{d}{dt} X &= \mathcal{A}_1 - \mathcal{A}_2 - (\mathcal{B} - C)(I_1 - I_2) + \mathcal{R}_2 e^{-X} + \mathcal{R}_1 e^X \end{cases} \quad (37)$$

which reduce to Eqs.(12) after one identifies  $\psi = \text{Im}[X]$ , and assumes  $C = 0$ . By translating  $\psi$  of an initial phase  $\psi_0 = \pi + (\epsilon_1 + \epsilon_2)/2$ , it also comes out that the dynamics of the system depends only on the value of the scattering angle difference  $\epsilon = (\epsilon_1 - \epsilon_2)/2$ . We assume in what follows that  $\epsilon_{1,2} = \pm\epsilon$ .

The matrix form of Eq.(37) is suitable for a general system analysis and identification. In fact, if the system of Eqs.(37) is written for a reciprocal ring (i.e.  $\mathcal{A}_1 = \mathcal{A}_2$ ,  $\mathcal{B}_1 = \mathcal{B}_2$ ,  $\mathcal{C}_{21} = \mathcal{C}_{12}$ , and  $\mathcal{R}_1 = \mathcal{R}_2$ ), it is clearly invariant under the transformation  $(E_1, E_2, \Omega_1, \Omega_2) \rightarrow (E_2, E_1, \Omega_2, \Omega_1)$ ; thus the corresponding phase portrait is topologically equivalent to a torus [68]. Therefore we have two kinds of asymptotic time behaviors depending whether or not the orbits in the phase space can be continuously shrunk to a point. For behaviors of the first kind, Eqs.(37) exhibit a fixed point, the beat frequency is equal to zero and the light intensities are constant (laser switched off or locked-in).

Conversely, the behaviors of the second kind are limit cycles regimes, characterized by nonzero beat frequency of the the counter-propagating waves (single mode laser operation). When the reciprocal conditions do not hold, the qualitative characteristics of asymptotic time behavior are left unchanged, due to the invariance of the phase portrait topology under continuous variation of  $RL$  parameters. The study of Eqs.(12) has been conducted by several authors in the past, both with numerical and analytical approaches. Analytic solutions of Eqs.(12) have been found in the case of  $I_1 \propto I_2$  [73],  $C_{21} = C_{12}$  and  $\mathcal{R}_1 = \mathcal{R}_2^*$  [51], or  $Re[C_{21}] = Re[C_{12}] = \mathcal{B}_1 = \mathcal{B}_2$ , [21]. However, general analytic solutions of the  $RL$  equations system with non reciprocal parameters are not known, and therefore perturbative solutions are necessary to study actual  $RL$ . Approximated analytical expressions for the time evolution of the *Sagnac* phase provide, nevertheless, an useful reference to better understand the role of the *Lamb* parameters noise on the estimation of the angular velocity  $\omega_s$ .

### 2.3.1 *Lamb* parameters effect on $RL$ performances

We present in the following the periodic solution of the  $RL$  dynamics, derived from Eqs.(12) in the case where:  $I_1/I_2 = k$  and,  $\tau_{12} = \tau_{21} = 0$ . In this case the phase equation takes the form:

$$\dot{\psi} = \omega_s - \frac{c}{L} \left[ r_1 k \sin(\psi - \varepsilon) + \frac{r_2}{k} \sin(\psi + \varepsilon) \right] . \quad (38)$$

Eq.(38) admits the following solution:

$$\psi(t) = 2 \arctan \left[ \frac{\Omega_{L1} + \Omega_p \tan \left( \frac{1}{2} \Omega_p t \right)}{\omega_s + \Omega_{L2}} \right] , \quad (39)$$

where  $\Omega_{L1} = c/L(kr_1 + r_2/k) \cos \varepsilon$ ,  $\Omega_{L2} = c/L(r_2/k - kr_1) \sin \varepsilon$  and  $\Omega_p = \sqrt{\omega_s^2 - \Omega_{L1}^2 - \Omega_{L2}^2}$ .

From Eq.(39), for  $\Omega_{L1,L2} \ll \omega_s$ , we get

$$\omega(t) \simeq \omega_s - \Omega_{L2} \cos \omega_s t - \Omega_{L1} \sin \omega_s t , \quad (40)$$

where  $\omega$  denotes the detected *Sagnac* frequency and  $\omega_{BS} \equiv -\Omega_{L2} \cos \omega_s t - \Omega_{L1} \sin \omega_s t$  represents the frequency modulation of the *Sagnac* signal.

In Figure 4 we report the results of a Monte Carlo simulation of  $10^6$  s of  $RL$  dynamics evolution with  $I_1/I_2 = k$ . We considered the following noise sources in the system: a white frequency noise, with standard deviation of  $10^{-1}$ , on  $\omega(t)$  (mimic of the output of  $AR(2)$  frequency detection algorithm) and a random-walk noise on the parameters  $r_{1,2}$ ,  $k$ , and  $\varepsilon$ . The *Allan* variance of  $\omega(t)$  has been calculated for four different cases, denoted with (a), (b), (c) and (d).

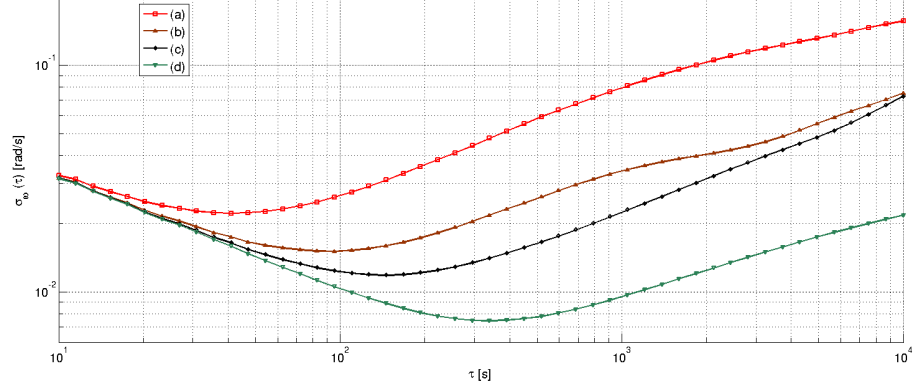


Figure 4: Simulated *Allan* deviations of the estimated rotation rate. See the text for details.

In case (a)  $(r_{1,2}, k, \varepsilon)$  are independent and vary in random walk with relative step size of  $(10^{-2}, 10^{-3}, 10^{-2})$  respectively. In case (b) the only varying parameter is  $k$ , with a step size of  $10^{-3}$ . In case (c) all parameters vary as in (a), but the processes  $r_1$  and  $r_2$  have been correlated with a correlation coefficient of 0.9, while  $\varepsilon$  varies around the nominal value of 0 rad with a random walk step size of  $10^{-4}$  rad. In case (d) all parameters vary as in (b), but the process  $\varepsilon$  varies around the nominal value of  $\pi/2$  rad with a random walk step size of  $10^{-4}$  rad.

It can be easily observed that the noise contribution coming from the parameters fluctuation is transferred to the noise of the measured *Sagnac* frequency exhibiting the same random walk plus white noise pattern. The relative noise on the laser parameters is converted into frequency noise by the factor  $c/L$  meaning that the larger is the cavity perimeter, the larger is the rejection of the laser parameters noise. In addition, it is worth noticing that the backscattering phase  $\varepsilon$  plays a crucial role in transferring the fluctuations of  $r_1, r_2$  on  $\omega$ . It determines a strong reduction of the output noise for values close to  $\varepsilon = \pi/2$  (trace (d)). In this regime, also known as *conservative coupling regime*, the backscattered photons interact destructively and their influence on the nonlinear interaction between the two intracavity beams and the active medium is minimized.

### 2.3.2 Steady state approximate solutions

To provide suitable algorithms for parameter estimation, we study the steady state regime of Eqs.(12). By inspection of the right hand side of Eqs.(12), one finds that the general steady state solutions are periodic. In particular, without backscattering ( $r_{1,2} = 0$ ), Eqs.(12) exhibit steady state solutions of the type



$$\begin{cases} I_1(t) &= \frac{\alpha_1}{\beta} \\ I_2(t) &= \frac{\alpha_2}{\beta} \\ \psi(t) &= \omega_s t \end{cases}, \quad (41)$$

for  $t \rightarrow \infty$ . In the presence of backscattering, the above solutions switch to periodic steady state solutions and exhibit oscillatory behaviors, and the backscattering can be treated as a perturbative sinusoidal forcing term. We can study the system oscillation around its unperturbed steady state by means of the time dependent perturbation theory [32]. To this aim we introduce the expansion parameter  $\lambda$ , which is assumed to be of the same order of magnitude of  $r_{1,2}$  and write:

$$\begin{cases} \mathcal{I}_1(\lambda, t) &= \sum_{k=0}^{\infty} \frac{\lambda^k}{k!} I_1^{(k)}(t) \\ \mathcal{I}_2(\lambda, t) &= \sum_{k=0}^{\infty} \frac{\lambda^k}{k!} I_2^{(k)}(t) \\ \Psi(\lambda, t) &= \sum_{k=0}^{\infty} \frac{\lambda^k}{k!} \psi^{(k)}(t) \end{cases} \quad (42)$$

For  $k = 0$ , substituting the latter into the Eqs.(12), we recover the solution (41) with the positions  $I_1^{(0)}(t) = \alpha_1/\beta$ ,  $I_2^{(0)}(t) = \alpha_2/\beta$ ,  $\psi^{(0)}(t) = \omega_s t$ . The approximated solutions can be calculated iteratively from the series expansion in powers of  $\lambda$  of (42) into the dynamic of Eqs.(12). A second order approximations of the solutions reads:

$$\begin{cases} \mathcal{I}_1(t) \simeq \frac{\alpha_1}{\beta} + 2r_2 \sqrt{\alpha_1 \alpha_2} \frac{\alpha_1 \cos(\varepsilon + \omega_s t) + \omega_s \sin(\varepsilon + \omega_s t)}{\beta (\alpha_1^2 + \omega_s^2)} - \frac{2r_1 r_2 \sin(2\varepsilon)}{\beta \omega_s} \\ \mathcal{I}_2(t) \simeq \frac{\alpha_2}{\beta} + 2r_1 \sqrt{\alpha_1 \alpha_2} \frac{\alpha_2 \cos(\varepsilon - \omega_s t) - \omega_s \sin(\varepsilon - \omega_s t)}{\beta (\alpha_2^2 + \omega_s^2)} + \frac{2r_1 r_2 \sin(2\varepsilon)}{\beta \omega_s} \\ \Psi(t) \simeq \left( \omega_s - \frac{2r_1 r_2 \cos(2\varepsilon)}{\omega_s} \right) t + \frac{r_1 \sqrt{\frac{\alpha_1}{\alpha_2}} \cos(\varepsilon - \omega_s t) + r_2 \sqrt{\frac{\alpha_2}{\alpha_1}} \cos(\varepsilon + \omega_s t)}{\omega_s}, \end{cases} \quad (43)$$

where we made the additional approximation of keeping the leading terms in  $\omega_s^n$ , with  $n \geq 2$ . Solutions (43) show a correction to the mean intensity level and pushing and pulling in the phase difference, as well as the presence of the first harmonic of  $\omega_s$ . A slightly more accurate solution can be obtained by the *Poincaré-Lindstedt* method [80], i.e. by substituting in Eq.(43) the approximate angular frequency (at the second order) with the exact angular frequency  $\omega$ , which can be directly obtained from experimental measurements.

## 2.4 CALIBRATION AND IDENTIFICATION PROCEDURES

With aim at applying *Kalman* filtering to *RLG* data for the estimation of the *Sagnac* frequency from the measured light intensity  $\{I_{1,2}(n)\}$ , and interferogram  $\{S(n)\}$  time series. In this way we can firstly estimate and then remove the parameters drifts effect in the detected beat frequency, thus increasing the long-term stability of the estimate of the rotation rate. To achieve also an accurate estimation of the rotation rate, we devise an identification procedure and a calibration method for the parameters associated to the non linear laser dynamics.

## 2.4.1 Dissipative parameters identification

The existence of a limit cycle greatly simplify the steady state analysis of the *RL* dynamics because asymptotic solutions are periodic with period  $T = 2\pi/\omega$ . In fact, we can construct the functional

$$J(\mathbf{I}, X, \mathbf{A}, \mathbf{B}) \equiv \left\| \frac{d}{dt} \log(\mathbf{I}) - 2\text{Re} \left[ \begin{pmatrix} \mathcal{A}_1 \\ \mathcal{A}_2 \end{pmatrix} - \mathbf{B} \cdot \mathbf{I} + \begin{pmatrix} \mathcal{R}_2 e^{-X} \\ \mathcal{R}_1 e^X \end{pmatrix} \right] \right\|_{L_2(T)}^2, \quad (44)$$

where  $\|\cdot\|_{L_2(T)} \equiv \sqrt{\int_0^T (\cdot)^2 dt}$  is the norm in the Hilbert space of  $L^2$  T-periodic signal, and search for its minimum value to derive a statistics of parameters estimation. From the perturbative solutions (43), we can write the steady state intensities approximate up to the first harmonic terms

$$\begin{cases} I_1(t) &= I_1 + i_1 \sin(\omega t + \phi_1) \\ I_2(t) &= I_2 + i_2 \sin(\omega t + \phi_2) \\ X(t) &= \frac{1}{2} \log \left[ \frac{I_1(t)}{I_2(t)} \right] + i\omega t \end{cases} \quad (45)$$

where  $I_{1,2}$ ,  $i_{1,2}$ , and  $\phi_{1,2}$  are the intensity offsets, monobeam modulation amplitudes and phases, which can be readily measured from *RL* outputs; it follows also that the backscattering phase differences can be simply estimated by  $\hat{\varepsilon}_{1,2} = \phi_{1,2}$ , so that it holds  $\hat{\varepsilon} = \phi_1 - \phi_2$ . Thus, after substituting Eqs.(45) into Eq.(44), we can estimate the cavity loss parameters  $\mu_{1,2}$  and  $r_{1,2}$  as

$$(\hat{\mu}_{1,2}, \hat{r}_{1,2}) = \underset{\mu_{1,2}, r_{1,2}}{\text{argmin}} \{J(I, X, \mathbf{A}, \mathbf{B})\}.$$

The new identified parameters read

$$\begin{cases} \hat{\mu}_{1,2} = \alpha_0 - \beta \left( I_{1,2} + \frac{i_{1,2}^2}{I_{1,2}} \right) - \frac{i_1 i_2 I_{2,1} (L\omega/c) \cos \hat{\epsilon}}{4I_{1,2}^2} - \\ - \theta \left( \frac{i_{2,1}^2 + 4I_{2,1}^2}{4I_{1,2}} - \frac{i_{1,2}^2 I_{2,1}^2}{2I_{1,2}^3} + \frac{i_1 i_2 I_{2,1} \cos \hat{\epsilon}}{I_{1,2}^2} + \frac{i_{2,1}^2 \cos 2\hat{\epsilon}}{4I_{1,2}} \right), \\ \hat{r}_{1,2} = \frac{i_{2,1} (L\omega/c)}{2\sqrt{I_{1,2}}} \mp i_{1,2} \sqrt{\frac{I_{1,2}}{I_{2,1}}} \theta \sin \hat{\epsilon} \end{cases}, \quad (46)$$

where  $\hat{\epsilon} = \hat{\epsilon}_1 - \hat{\epsilon}_2$ , and  $\alpha_0$  is the excess gain for zero losses. Unfortunately, the minimization of the functional in Eq.(44) is ill-posed for the full set of *Lamb* parameters, and so different approaches for their measurement must be investigated.

#### 2.4.2 Experimental calibration

Here we discuss the theory used and the different monitors employed in our calibration procedure, and give details on their derivation and implementation.

##### 2.4.2.1 Ring Down time measurement

The spectroscopic technique known as “*Ring Down Time measurement*” (*RDT*) allow us to estimate mirror losses from the impulse response of a linear system. In fact, from Eq.(8) written with  $G = 0$ , we have

$$\dot{\mathbf{E}} = \mathbf{M} \cdot \mathbf{E}, \quad (47)$$

and so the system shows two exponential decays, which reflect losses parameters. If we switch off the laser excitation at the time  $t = 0$ , the initial conditions are  $\mathbf{E}(0) = \left[ \sqrt{I_1(0)}, \sqrt{I_2(0)} e^{i\phi_0} \right]$ , where  $I_{1,2}(0)$  are the initial intensities, and  $\phi_0$  is the initial phase difference equal to  $(\epsilon_1 - \epsilon_2)/2$ .

The solutions of Eq.(47) for the light intensities, expanded in series of  $\omega \gg \frac{c}{L} r_{1,2}, \frac{c}{L} \mu_1, \frac{c}{L} \mu_2$  up to the first order, reads

$$\begin{cases} I_1(t) = I_1(0) e^{-\frac{c}{L} \mu_1 t} \\ I_2(t) = I_2(0) e^{-\frac{c}{L} \mu_2 t} \end{cases}, \quad (48)$$

The experimental procedure to measure the light decays is performed by recording with a fast detector, (photomultiplier *Hamamatsu H7827012*) loaded on a 1 k $\Omega$  impedance, after a rapid switch off of the radio-frequency discharge. The switching-off operation has to be much faster than the laser decay time. In our setup we obtain a sufficiently rapid switch off by grounding one of the two electrodes of the radio-frequency discharge by means of a mechanical switch. A validation of this technique is obtained by measuring the decay time of the plasma fluorescence which results to be of the order of few mi-

croseconds. Finally, we performed an exponential fit of the collected data.

#### 2.4.2.2 Calibration of Intensities in Lamb units

To get accurate estimates of the *Sagnac* frequency, the light intensities input of the *EKF* must be calibrated in *Lamb* units. An accurate experimental method consists in the generation of additional longitudinal mode to the two fundamental cavity modes. This dynamical change is known as “multimode transition”, and has been widely studied in the literature, mainly for medium size and large size *RLs*. The multimode transition can be achieved by increasing the laser output power and the laser single pass gain until new modes appear. The value of the mean light intensity for the multimode transition expressed in lamb units  $I_{th}$ , is commonly defined multimode threshold [34, 33]. Different calculations of the multimode threshold were proposed [33], taking into account only the plasma dispersion function, evaluated at frequencies of fundamental and higher order modes. To increase the accuracy of the multimode threshold its convenient to account for cavity losses and back-scattering in the balance of gained and lost photons for longitudinal lasing modes.

The threshold condition for multimode transition can be calculated from the stability analysis of the *RL* system. Starting from Eqs.(37), we can write the following system of equations for the intensities  $I_{1,2}$  of two fundamental modes

$$\dot{\mathbf{I}} = \text{Re} (\mathcal{D}(\mathbf{E}^*)\dot{\mathbf{E}}) = \text{Re} (\mathcal{D}(\mathbf{E}^*)\cdot\mathbf{A}\mathbf{E} - \mathcal{D}(\mathbf{I})\cdot\mathbf{B}\cdot\mathcal{D}(\mathbf{E}^*)\mathbf{E}) , \quad (49)$$

where  $\mathbf{I} = (I_1, I_2)^T$ . If a new  $m$ -mode (lasing at  $\omega_{1,2} + mc/L$ ) adds to the system, its dynamics will depend on 4 intensities of light  $I_{1,2,3,4}$ . The evolution of the system is still ruled by Eqs(49), provided that we substitute the  $2 \times 2$  matrices  $\mathbf{A}$  and  $\mathbf{B}$  with the corresponding  $4 \times 4$  matrices, calculated by means of the plasma dispersion function for 4 intensities (see Subsection 2.2.1).

We now consider the system in the initial configuration  $(I_1, I_2, 0, 0)^T$  and look for the condition of the  $m$ -th mode growth. The lower diagonal block of the Jacobian matrix of the 4 modes dynamical system is given by

$$\begin{pmatrix} \cdots & \cdots & \cdots & \cdots \\ \cdots & \cdots & \cdots & \cdots \\ 0 & 0 & \alpha_3 - \theta_{31}I_1 - \theta_{32}I_2 & 0 \\ 0 & 0 & 0 & \alpha_4 - \theta_{41}I_1 - \theta_{42}I_2 \end{pmatrix} , \quad (50)$$

where  $\alpha_{3,4}$  are the gain minus losses of clockwise and counter-clockwise  $m$ -th mode, and  $\theta_{31,41,32,42}$  are the cross saturation coefficients between fundamental and  $m$ -th modes propagating in clockwise and counter-clockwise direction. By the Lyapunov linearization theorem, if the eigenvalues of the above matrix lie in the strictly positive complex half-plane, the equilibrium point is unstable, and the new laser modes can start to grow [69]. Therefore an higher  $m$ -mode can be excited if  $\alpha_3 - \theta_{31}I_1 - \theta_{32}I_2 > 0$  and  $\alpha_4 - \theta_{41}I_1 - \theta_{42}I_2 > 0$ . Since the frequency difference of the two counter-propagating beams is much smaller than the *Doppler* width, we have  $\theta_{31} \sim \theta_{42} \sim \theta_{ms}$ ,  $\theta_{32} \sim \theta_{41} \sim \theta_{mc}$ . Thus, to derive a threshold condition for the multimode operation we can take the average of the two inequalities and write

$$\bar{\alpha}_m > \bar{\theta}_m \bar{I},$$

where  $\bar{\alpha}_m = (\alpha_3 + \alpha_4)/2$ ,  $\bar{I} = (I_1 + I_2)/2$  and  $\bar{\theta}_m = (\theta_{ms} + \theta_{mc})/2$ , and so the threshold condition for the intensity  $I_{th}$  is

$$\bar{\alpha}_m = \bar{\theta}_m I_{th}. \quad (51)$$

This condition is not sufficient to determine the multimode threshold because active laser parameters depend on the value of the single pass gain at the threshold  $G_{th}$ , which is also unknown. However, we can add to Eq. (51) a second equation representing the balance of the average intensity for the fundamental mode in steady state, and write the equation system

$$\begin{cases} G_{th} z_m^{(0)}(\xi) - \bar{\mu} = 2I_{th} G_{th} [z_m^{(2)}(\xi_m)] \\ G_{th} z^{(0)}(\xi) - \bar{\mu} = I_{th} G_{th} [z_s^{(2)}(\xi) + z_c^{(2)}(\xi) \frac{1+3\delta_I^2}{1-\delta_I^2}] \end{cases}, \quad (52)$$

where  $\xi_m$  is the normalized detuning averaged over the beams 3 or 4,  $\delta_I = (I_1 - I_2)/(I_1 + I_2)$ ,  $\bar{\mu} = (\mu_1 + \mu_2)/2$ ,  $z_m^{(0)}$ ,  $z_s^{(0)}$  and  $z_c^{(0)}$  are polarization contributions from the plasma dispersion function which are computed in Subsection (2.2.1). As  $m$ -modes are very close in frequency, their losses can be assumed with good approximation to be equal. The quantity  $\delta_I$  can be estimated from the acquired intensity channels  $V_{1,2}$  as  $\delta_I = (V_1 - V_2)/(V_1 + V_2)$ . It is worth noticing that the measure of  $\delta_I$  is independent of multiplicative change of scale. The multimode condition can be derived by solving Eq.(52) in the variables  $G_{th}$  and  $I_{th}$ ,

$$\begin{cases} I_{th} = \frac{\Delta z^{(0)} (1 - \delta_I^2)}{\Delta z^{(2)} + \delta_I^2 (\Delta z^{(2)} - 4z_c^{(2)}(\xi))}, \\ G_{th} = \frac{\bar{\mu}}{z_m^{(0)}(\xi) - I_{th} z_m^{(2)}(\xi_m)} \end{cases}, \quad (53)$$

where  $\Delta z^{(0)} = z^{(0)}(\xi) - z_m^{(0)}(\xi)$ ,  $\Delta z^{(2)} = z_s^{(2)}(\xi) + z_c^{(2)}(\xi) - 2z_m^{(2)}(\xi_m)$  represent the difference between the fundamental and  $m$ -modes of the  $0^{th}$  and  $2^{nd}$  population inversion contributions. The resulting value  $I_{th}$  provides the calibration of the voltages  $\{V_{1,2}(n)\}$ , acquired by photodetectors as detailed in Subsection 2.1.3, to the intensities  $\{I_{1,2}(n)\}$  in *Lamb* units. In addition, we have also derived an estimate of  $G_{th}$  that will be used as the initial value of the gain monitor.

### 2.4.2.3 Population Inversion Monitor

The intensity of the plasma fluorescence line at 632.8 nm provides a good observable for monitoring the relative variations of the atomic population in the upper laser level. In order to perform an on-line measurement of the laser gain, we coupled part of the plasma fluorescence to a multi-fiber bundle. The collected light containing all the spectral contribution of the *He – Ne* discharge, is filtered by a line filter 1 nm wide around 632.8 nm and detected with a photodiode. The photocurrent is amplified with a transimpedance stage with a gain of 1 G $\Omega$ . The voltage  $V_p$  of the photodiode is used as an optical monitor of the laser gain by recording the dependence of the output powers  $I_1$  and  $I_2$  on  $V_p$ , after losses have been estimated. The calibration of the monitor signal is obtained by performing intensity steps in the neighborhood of the monomode working regime of the *RL*, exploiting the identification procedure described in Eq.(46), and a linear least squares fit. In fact, the second equation of the system in Eq.(52), representing the balance among gain, losses and mean intensities, holds for any value of  $G$  and  $\bar{I}$ . By solving this equation for the variable  $G$ , and using  $N$  measurements  $\{\bar{I}(n)\}$  and  $\{\delta_I(n)\}$  ( $n = 1, 2, 3 \dots, N$ ) in the monomode regime, we obtain  $N$  estimates of the gain signal

$$G(n) = \frac{\bar{\mu}}{z^{(0)}(\xi) - \bar{I}(n) \left( z_s^{(2)}(\xi) + z_c^{(2)}(\xi) \frac{1+3\delta_I^2(n)}{1-\delta_I^2(n)} \right)},$$

where the mean losses value  $\bar{\mu}$  is supposed to be constant and equal to the mean of *RDT* estimation.

To account for the experimental setup, we can consider a simple linear measure model  $G = aV_p + b$  for the gain monitor signal  $V_p$ , where the constants  $a$  and  $b$  have to be estimated by the linear least squares fit

$$\begin{pmatrix} \hat{a} \\ \hat{b} \end{pmatrix} = \operatorname{argmin}_{a,b} \left\| \begin{pmatrix} V_p(1) & 1 \\ \vdots & \vdots \\ V_p(N) & 1 \end{pmatrix} \begin{pmatrix} a \\ b \end{pmatrix} - \mathbf{G} \right\|^2,$$

where  $\mathbf{G} = [G(1), \dots, G(n)]$  is the vector of gain estimates. The estimated constants  $\hat{a}$ ,  $\hat{b}$  and  $G_{th}$  allow us to monitor the laser single

pass gain by acquiring the signal  $V_p$  without affecting the continuous operation of a *RL*.

#### 2.4.2.4 Spectroscopic probe of the gain medium

Essential information about the gain medium can be extracted by observing the *Doppler* absorption of the plasma at  $640.2 \text{ nm}$  using a tunable laser crossing. This is a closed transition of Neon and can be easily interrogated by probing the *He – Ne* plasma through the pyrex allowing the *RL* radio-frequency excitation. We setup a frequency tunable *ECDL* (Extended Cavity Diode Laser) crossing the *He – Ne* plasma through the pyrex capillary. From this measurement one can get a precise estimation of the *Doppler* broadening, as well as of the isotopic composition of the gas. An example of this measurement is given in Fig. 15, where a standard *He – Ne* gas mixture has been studied by injecting a scanning laser frequency around  $640.2 \text{ nm}$ .

#### 2.4.3 Estimation of $\omega_s$ by EKF

Knowledge of the *Lamb* parameters  $\hat{\alpha}_{1,2}$ ,  $\hat{r}_{1,2}$  and  $\hat{\varepsilon}$ , together with the gain  $G$  separately acquired, allow us to set up an *EKF* for the estimation of the rotation rate  $\hat{\omega}_s$ . The *EKF* state variables are the  $\mathbb{R}^3$  vector  $\mathbf{X}(t) \equiv [I_1(t), I_2(t), \psi(t)]^T$ . The dynamics model is given by Eqs., with the addition of the model error as a zero mean, white, stochastic vector field  $\mathbf{v}(t)$  with variance  $\text{Var}[\mathbf{v}(t)] \equiv Q$ , where  $Q$  is a  $3 \times 3$  covariance matrix that accounts for the effects of unmodeled dynamics, for instance, identified parameter errors, calibration errors, and numerical integration inaccuracies. The *EKF* prediction step, which corresponds to the integration of Eqs.(12) over the time interval  $T_s$ , is carried out using the *RK4 Runge-Kutta* routine. In the discrete time domain, the model of the measurement process reads  $\{\mathbf{y}(n)\} = \{\mathbf{X}(n)\} + \{\mathbf{w}(n)\}$ , where  $\mathbf{w}(n)$  is zero mean, white, stochastic vector field (observation noise) with variance  $\text{Var}[\mathbf{w}(n)] \equiv R$ , and  $R$  is a  $3 \times 3$  covariance matrix. In the standard experimental set up of *RLGs*  $[I_1(t), I_2(t), \psi(t)]$  are measured by independent sensors, and so we can assume that  $R$  is diagonal, with diagonal elements the observation noise variances  $\sigma_{I_1}^2, \sigma_{I_2}^2, \sigma_{\psi}^2$  which can be conveniently calculated through the level of white noise in the power spectrum of  $\{\mathbf{y}(n)\}$ .

The backscattering frequency is estimated from the filtered channels  $\hat{I}_{1,2}(n)$ ,  $\hat{\psi}(n)$ , the identified parameters  $\hat{\alpha}_{1,2}$ ,  $\hat{r}_{1,2}$ ,  $\hat{\varepsilon}$ , and the exogenous parameter  $\beta$  as

$$\hat{\omega}_{BS} = \frac{c}{L} \left[ \hat{r}_1 \sqrt{\frac{\hat{I}_1}{\hat{I}_2}} \sin(\hat{\psi} - \hat{\varepsilon}) + \hat{r}_2 \sqrt{\frac{\hat{I}_2}{\hat{I}_1}} \sin(\hat{\psi} + \hat{\varepsilon}) \right]$$

where, for simplicity, we have dropped the index ( $n$ ) from time series. The *Sagnac* frequency is then estimated from the difference

$\hat{\omega}_s = \hat{\psi} - \hat{\omega}_{BS}$ , where the numerical derivative of  $\hat{\psi}$  has been computed by the “5 point method” [53] designed to reject the derivative amplification of the noise.

#### 2.4.4 Pre-filtering scheme implementation

The data are acquired at a sampling frequency of 5 kHz ( $T_s = 200 \mu\text{s}$ ). To remove the oscillating component, intensity signals are low-pass filtered with a first order *Butterworth* filter with 1 Hz cutoff frequency. The quantities  $I_{1,2}$  are estimated by averaging the decimated intensities over a time interval of 10 s (i.e.  $5 \times 10^4$  samples). On the other side, to calculate the modulation  $i_{1,2}$  and phases  $\phi_{1,2}$ , the intensities are first band-passed around the fundamental *Sagnac* band [95 ÷ 125] Hz by means of a *Butterworth* filter, and decimated by a factor 2. The decimation procedure has been carried out by the tail recursive routine “Zoom and Decimation of a factor  $2^n$ ” ( $ZD(n)$ ), where each iteration step is composed by a half band filter stage with discrete transfer function  $H(z) = \left( \frac{z^3 + 2z^2 + 2z + 2}{4z^3 + 2z} \right)^5$ , followed by a downsampling by 2. The  $ZD(n)$  procedure ensures a linear phase filter response at least for  $n = 3$  iterations, as no appreciable phase distortion was observed in simulated sinusoidal signals. The resulting data are then demodulated with a digital lock-in using as reference signal the discrete *Hilbert* transform of the interferogram, and setting the integration time to 10 s. A schematic of the parameter estimation procedure is reported in Fig.5. In addition, the phase of the two monobeam oscillating components is determined by the discrete *Hilbert* transform, and their difference is estimated by unwrapping the phase angle and taking its average over 10 s. As a concluding remark on the parameter estimation procedure, we mention that the problem of filtering very long time series has been solved by the “*overlap and save*” method, which is an efficient algorithm for avoiding the boundary transients due to finite length of digital filters.

## 2.5 RESULTS AND DISCUSSION

We here describe the implementation of the *Lamb* parameter estimation procedures for simulation tests, and then for the *G-PISA* and *G-WETTZELL* RLGs, and the results obtained. The two rings employ different types of laser discharge circuits and diagnostic sensors, and different informations about the rings orientations were available. We implemented the subtraction of the laser systematic effects in the beat frequency of *G-PISA* with and without the calibration of the experimental apparatus. For the RLG *G-WETTZELL* the calibration of the experimental apparatus could not have been performed up to now. When no calibration is provided the numerical values needed, e.g.



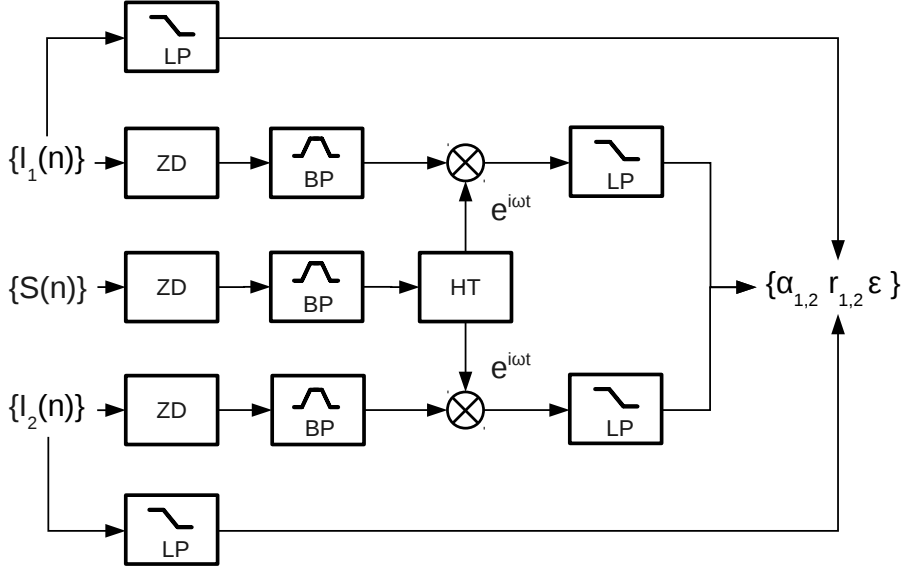


Figure 5: Schematic of the parameter estimation procedure, where  $LP \rightarrow$  lowpass *Butterworth* filter,  $BP \rightarrow$  bandpass *Butterworth* filter,  $ZD \rightarrow$  Zoom and Decimation routine,  $HT \rightarrow$  *Hilbert* transform (see text).

the laser gain and the calibration constants of the detectors, are set to some reasonable values.

### 2.5.1 Simulation results

The reliability of the parameter estimation routine is tested by Monte Carlo simulations of the dynamics of Eqs.(12) followed by the estimations of *Lamb* parameters from the simulated time series of  $I_{1,2}$  and  $\psi$ . We run  $10^4$  simulations of Eqs.(12) allowing  $\alpha_{1,2}$  and  $r_{1,2}$  to vary according to normal distributions with mean as in Tab.3 and standard deviation equal to 10% of their means. In addition,  $\beta$  is assumed constant, and  $\epsilon_{1,2}$  uniformly distributed in  $[0, \pi/2)$ . In each simulation, we have compared the numerical *RK4* solution of Eqs.(12) and approximated analytical solution (43) evaluated with the same *Lamb* parameters. We found that they are in a very good agreement, with means of the relative errors on  $I_1(t)$ ,  $I_2(t)$  and  $\psi(t)$  of  $-6.4 \times 10^{-7}$ ,  $-6.2 \times 10^{-7}$  and  $-1.5 \times 10^{-5}$ , and standard deviations of  $4.6 \times 10^{-6}$ ,  $4.6 \times 10^{-6}$  and  $1.3 \times 10^{-6}$ , respectively.

To numerically assess the performance of the parameter estimation procedure, we run a simulation of 6 hours in which  $\alpha_{1,2}$ ,  $r_{1,2}$ ,  $\epsilon_{1,2}$  and  $\omega_s$  fluctuate according to independent random walk processes with self-correlation time of 1 hour. To reproduce the experimental behavior of a *RLG*, the time drift of  $\omega_s$ , which mimic the effects of local tilts and rotations, is a factor of 5 lower than the auto-correlation times of the other parameters. We superimposed to the simulated data an

$c/L$	$5.5 \times 10^7 \text{Hz}$
$\alpha_{1,2}$	$\sim 10^{-6}$
$\beta$	$5 \times 10^{-5}$
$\theta$	$6.5 \times 10^{-6}$
$r_{1,2}$	$\sim 2 \times 10^{-7}$
$\tau$	180 rad/s

Table 3: Reference values of the *Lamb* parameters used in the simulation of *G-PISA* dynamics. The contribution of  $r_{1,2}$  and  $\tau$  to the *Sagnac* frequency is of the order of 1.5 Hz and  $10^{-2}$  Hz, respectively.

additive white noise, with  $SNR=10^2$  for the beam intensities and  $SNR=5 \times 10^3$  for the interferogram. Such order of magnitudes are routinely achieved in large RLGs. The results we got are summarized in Fig. 6, Fig. 7 and Fig. 8.

The overall accuracy of the *Lamb* parameter estimation procedure is good, with a relative standard deviation of  $3 \times 10^{-3}$  and  $4 \times 10^{-3}$  in the estimation of  $\alpha_{1,2}$ , and  $r_{1,2}$ , respectively. The absolute error in the estimation of  $\varepsilon$  is  $3 \times 10^{-3}$  rad. The attained accuracy is not far from the lower bound  $\sim 10^{-4}$  associated to the level of the observation noise of  $\{I_1(n)\}$ ,  $\{I_2(n)\}$  and  $\{\psi(n)\}$ . The capability of the *EKF* in increasing the time stability and the resolution of the gyroscope has been tested with a 6 hours simulation of the *RL* dynamics. We use the typical parameters of *G-PISA* as given in Tab. 3, their variations were simulated as in the parameter estimation tests. We used a step size of 0.2 msec to integrate the Eqs.(12).

The results are summarized in Fig.9, where we compared the *Allan* variance of *AR*(2) and *EKF* frequency estimations. We conclude that, for this simulation with typical parameters of middle-size rings, the rotational resolution increases by a factor of 10 while the minimum of the *Allan* deviation shifts from 60 s to 360 s.

Then we have studied the bias induced in the estimate of the *Sagnac* frequency by the approximations made in Eq.(46). The parameters  $\alpha_{1,2}$ ,  $r_{1,2}$  and  $\varepsilon$  are simulated as independent random walks with starting value as in Tab.3, correlation time of half of the simulation length 300 s, and relative step size of  $10^{-2}$ . The initial value of the backscattering phase  $\varepsilon$  is assumed uniformly distributed in  $[0, \pi/2]$ . We find that the relative accuracy of the *Sagnac* frequency estimation is few parts in  $10^5$ .

Moreover, the Monte Carlo simulations show that the precision and accuracy of the identification procedure increases with the dimension of the ring, as the values of *Lamb* parameters decrease linearly with the free spectral range; e.g. for a square ring with a side of  $\simeq 1, 5$  and 10 m we found that the relative frequency accuracy is few parts in  $10^5, 10^8$ , and  $10^9$ , respectively. Other Monte Carlo simulations were run by appropriately biasing the intensity time series, to mimic a sys-

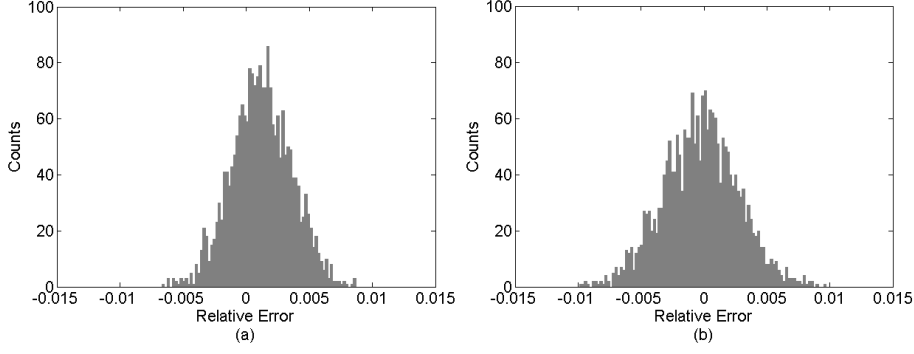


Figure 6: Histograms of the relative errors  $(\hat{\alpha}_{1,2} - \alpha_{1,2})/\alpha_{1,2}$  that affect the estimation of Gain minus losses parameters calculated with  $2 \times 10^4$  realizations of the *RL* dynamics. (a) Histogram relative to  $\alpha_1$  : mean  $1.4 \times 10^{-3}$  and standard deviation  $2.9 \times 10^{-3}$ ; (b) histogram relative to  $\alpha_2$  : mean  $-2.5 \times 10^{-4}$  and standard deviation  $3.9 \times 10^{-3}$ .

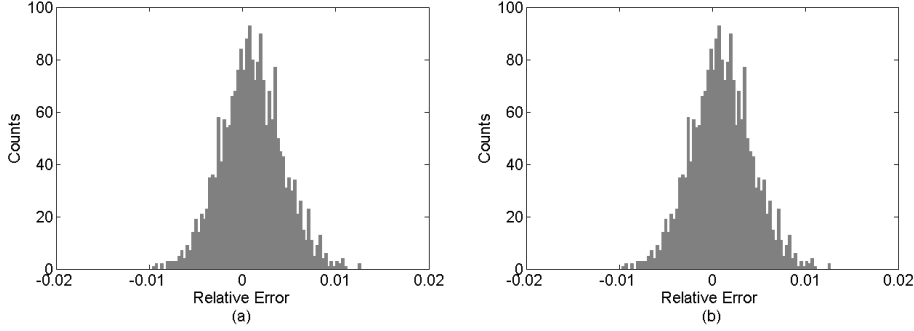


Figure 7: Histograms of the relative errors  $(\hat{r}_{1,2} - r_{1,2})/r_{1,2}$  that affect the estimation of backscattering coefficients calculated with  $2 \times 10^4$  realizations of the *RL* dynamics. (a) Histogram relative to  $r_1$  : mean  $1.1 \times 10^{-3}$  and standard deviation  $4.6 \times 10^{-3}$ ; (b) histogram relative to  $r_2$  : mean  $1.3 \times 10^{-3}$  and standard deviation  $3.2 \times 10^{-3}$ .

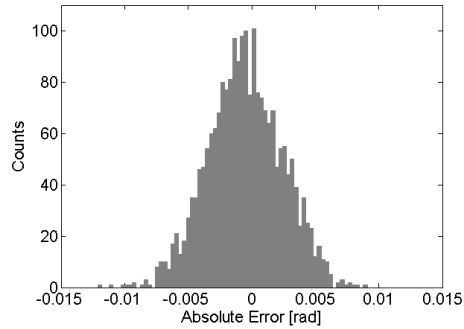


Figure 8: Histogram of the absolute errors  $\hat{\varepsilon} - \varepsilon$  that affect the estimation of backscattering phase calculated with  $2 \times 10^4$  realizations of the *RL* dynamics; mean  $-4.3 \times 10^{-4}$  rad and standard deviation  $2.8 \times 10^{-3}$  rad.

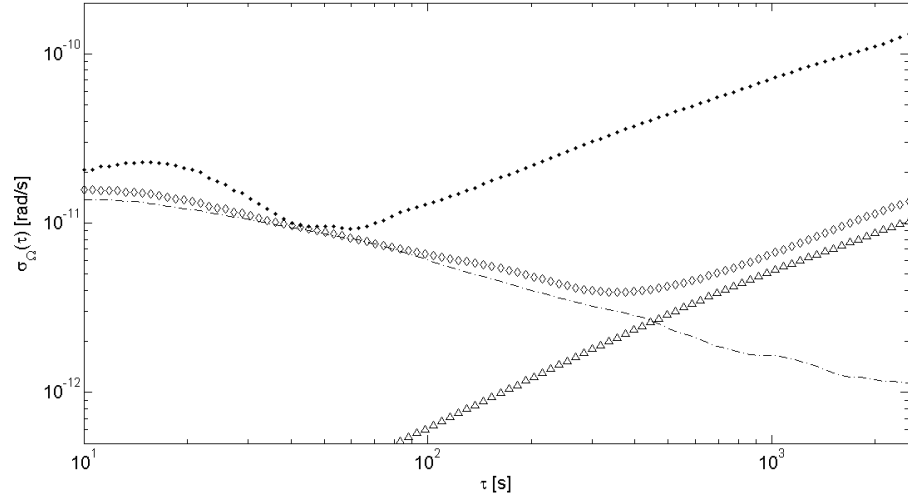


Figure 9: *Allan* deviation of the rotation rate estimated by *AR(2)* method (dots) and *EKF* (open diamonds) using  $2 \times 10^4$  seconds of the Monte Carlo simulation with random walk of *Lamb* Parameters. For comparison, we also plot the *Allan* deviation of the simulated rotational drift (open triangles), and the *Allan* deviation of the *EKF* estimation after the subtraction of the rotational drift (dash dotted line).

tematic error in their calibration in *Lamb* units or acquisition process. It results that the corresponding relative error in the *Sagnac* frequency estimation mainly depends on the values of  $r_{1,2}$ ,  $\tau$  and  $\varepsilon$ . In particular, for the typical *G-PISA* parameters in table 3, the relative frequency error scales linearly with the intensity error, and it turns out to be  $\simeq 1$  part in  $10^4$  times the intensity relative error. Finally, we studied the effects of systematic errors of the laser active medium parameters. The end result of these Monte Carlo runs is that the accuracy of the *Sagnac* frequency estimation is dominated by systematic errors of the single pass gain. For instance, by biasing the relevant active medium parameters  $\beta$ ,  $\theta$  and  $\tau$  of a relative error of  $10^{-1}$ ,  $10^{-2}$ , and  $10^{-3}$ , the corresponding relative error in the *Sagnac* frequency turns out to be  $10^{-4}$ ,  $10^{-5}$ , and  $10^{-6}$ , respectively.

### 2.5.2 Analysis of *G-PISA* data

We applied our identification and estimation routines for the subtraction laser dynamics from the beat frequency signal of the instrument *G-PISA*. *EKF* and parameter identification were used on data both with and without the experimental calibration of the laser gain parameter and photodetectors proposed.

#### 2.5.2.1 *G-PISA* experimental setup

The *G-PISA* cavity is fixed to a granite table that, in its turn, is firmly attached to a special monument completed in 2012 [79]. The monu-

ment is made of reinforced concrete. The optical setup of *G-PISA* is shown in Fig. 10. The *Sagnac* signal and the single beams are detected with large area ( $5.8 \times 5.8 \text{ mm}^2$ ) *Si* photodiodes (*Hamamatsu S1227-66BR*), followed by a transimpedance amplifier (*FEMTO LCA-4K-1G*) with a gain of  $10^9 \Omega$  and bandwidth of 4 kHz. On the corner opposite to the one for the *Sagnac* detection an optical beat setup is mounted between the clock-wise beam and the stabilized *He – Ne* reference laser. The beat is detected by an avalanche photodiode whose current is amplified by a transimpedance amplifier (*FEMTO HCA-400M-5K-C*) with a gain of 4 k $\Omega$  and a bandwidth of 400 MHz. During *G-PISA* operation, the detuning of the clock-wise wave is kept constant by a perimeter stabilization loop [79], acting on the position of two opposite mirrors of the cavity. The ring laser frequency is locked in this way to the value where  $\text{Re}[z^{(0)}(\xi_{1,2})]$  attains its maximum.

### 2.5.2.2 *Sagnac Frequency Estimation results without calibration*

We run the parameter estimation routine on the *G-PISA* data without making use of the calibration procedure. The photodetector signals  $V_{1,2}(t)$  are converted to dimensionless intensities  $I_{1,2}(t)$  (*Lamb* units), using the following relation

$$I_{1,2}(t) = c_{Lamb} \frac{V_{1,2}(t)}{G_{ph} a_{eff}} \equiv c_{Lamb} P_{out 1,2}, \quad (54)$$

where:  $G_{ph} = 10^9 \text{ V/A}$  is the photo-amplifiers gain,  $a_{eff} = 0.4 \text{ A/W}$  is the quantum efficiency of the photo-diodes, and  $c_{Lamb} = 3.5 \times 10^6 \text{ W}^{-1}$  is the calibration constant to *Lamb* units.  $P_{out 1,2}$  is the output power in Watt. The parameter estimation for *G-PISA* is completed by the acquisition of the laser gain  $G$ .

In Fig. 11 we show the comparison between the time series measured on the *RLG G-PISA* and the signals computed by our algorithm after the parameter estimation step, according to the schematic in Fig. 5.

In Fig. 12 we show the time series of the identified parameters and of  $\beta$ , for the *RLG G-PISA*.

After the estimation of the *G-PISA* parameters, we apply the *EKF* to the light intensities and to the interferogram. However, the implementation of the *EKF* requires an estimation of the covariance matrices  $Q$  and  $R$  of observation and model errors. Typically  $Q$  and  $R$  are considered as tuning parameters and set on the base of trial-and-error procedures. In fact, we started from an initial raw estimation for the diagonal elements of  $Q$  and  $R$  using simulations and power spectra of  $I_{1,2}$  and  $\psi$ , respectively. Then we tuned these values searching for the minimum of the *Allan* variance of  $\omega_s$  and came to  $Q = \text{diag}(10^{-8}, 10^{-8}, 10^{-10})$  and  $R = \text{diag}(10^{-8}, 10^{-8}, 10^{-8})$ .

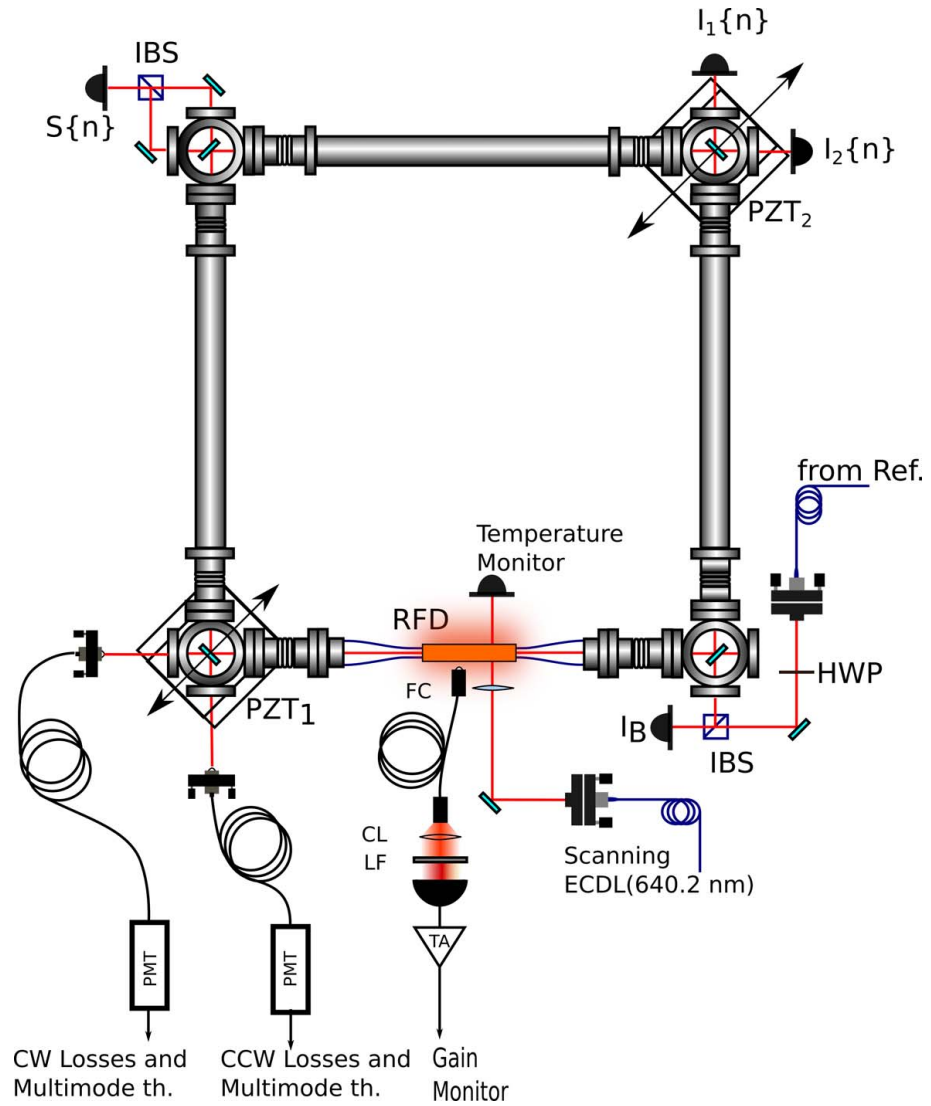


Figure 10: The experimental setup for the rotation measurement and the calibration of the RL parameters. *PMT*: photomultiplier tube, *TA*: transimpedance amplifier, *LF*:line filter, *CL*: Collimating lens, *ECDL*: extended cavity diode laser, *TA* gain for *G-PISA* is  $1\text{ G}\Omega$ .

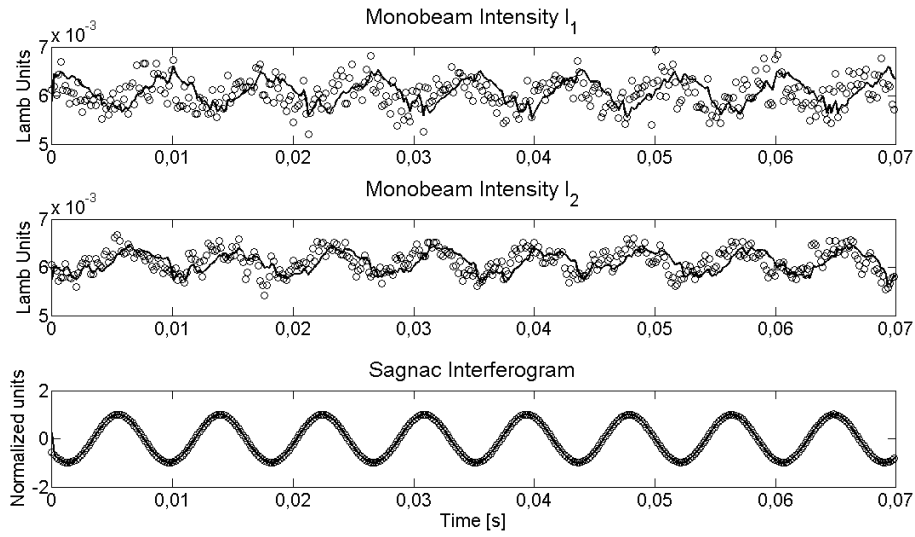


Figure 11: Comparison of the estimated and observed time series of  $I_1(t)$ ,  $I_2(t)$  and  $\sin(\psi(t))$  using the experimental data of *G-PISA*.

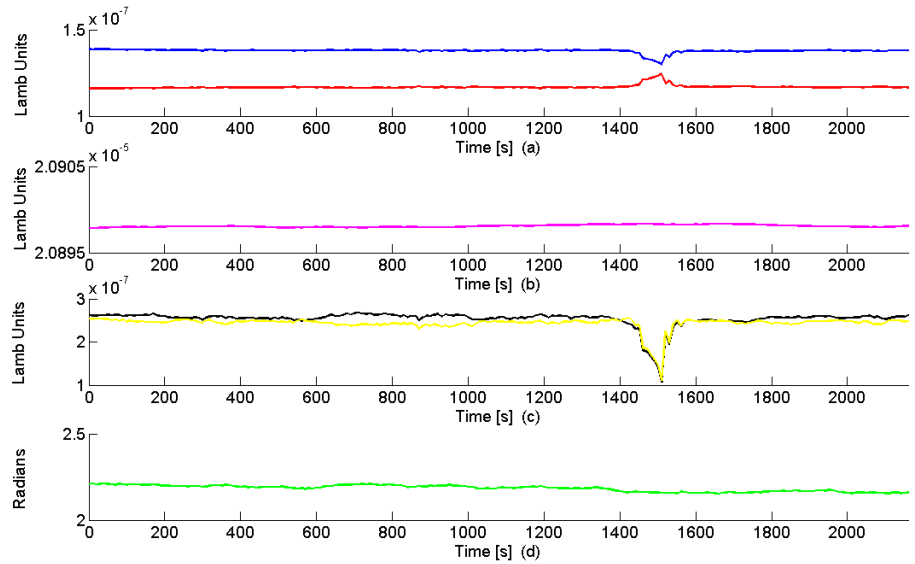


Figure 12: Time series of the  $\alpha_{1,2}$ ,  $\beta$ ,  $r_{1,2}$  and  $\epsilon$ . The parameters  $\alpha_{1,2}$ ,  $r_{1,2}$  and  $\epsilon$  have been estimated using  $2 \times 10^4$  seconds of experimental data of *G-PISA*.

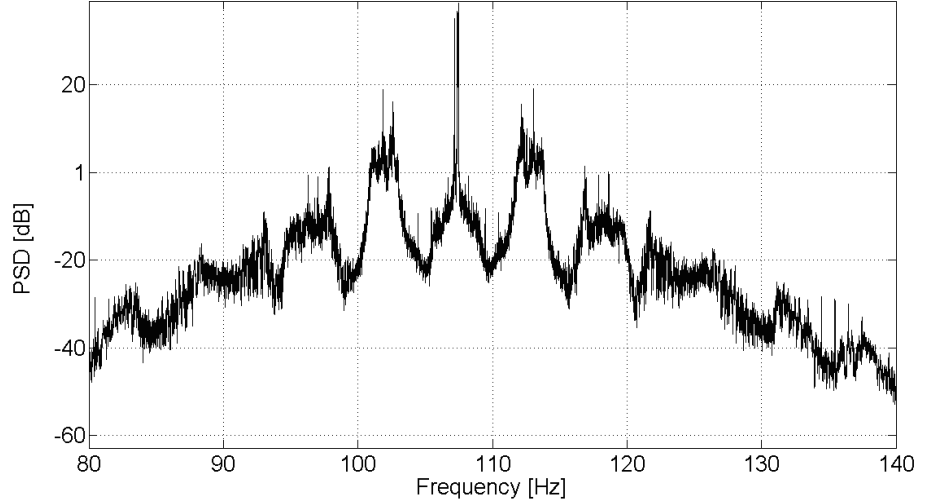


Figure 13: Power spectrum of the interferogram data around the *Sagnac* frequency  $\sim 107.3$  Hz.

The performances of parameter estimation and *EKF* were limited by the environmental conditions of *G-PISA*, e.g. local tilts and spurious rotations induced by the granite slab that support the instrument and some electronic disturbances, as it can be seen in Fig.13, showing the power spectrum of  $\{S(n)\}$ .

In figure 14 we report the *Allan* deviation of the *Sagnac* frequency estimated with *AR(2)* and *EKF*.

### 2.5.2.3 Measurement setup for calibration

To increase the level of precision and accuracy in the rotation-rate measurements, cold cavity and active medium parameters (Neon atomic kinetic temperature  $T_p$ , the total gas pressure  $p$ , and isotopic composition  $k'$ ,  $k''$ ) should be directly measured on the experimental apparatus. The experimental setup for the calibration of a *RLG* is sketched in Fig.10. To measure the ring-down times of the clockwise and counterclockwise mode, the beams exiting the corner opposite to the one dedicated to the intensities monitors are injected into two single mode fibers, and detected by two photomultiplier (*Hamamatsu H7827012*). Two diagnostics have been arranged for the estimation of the active medium parameters. A monitor for the gain variations and an absorption spectroscopy setup where a tunable diode laser interrogates the plasma across the laser pyrex capillary. In order to perform an on-line measurement of this quantity, we coupled part of the plasma fluorescence to a multi-fiber bundle and detect it with a photodiode after a line filter 1 nm wide around 632.8 nm, as sketched in Fig.10. The photocurrent is amplified with a transimpedance stage with a gain of 1 G $\Omega$ . The voltage  $V_p$  of the photodiode is used as an optical monitor of the laser gain by recording the dependence of the output powers  $I_1$  and  $I_2$  on  $V_p$ , after losses have been estimated.



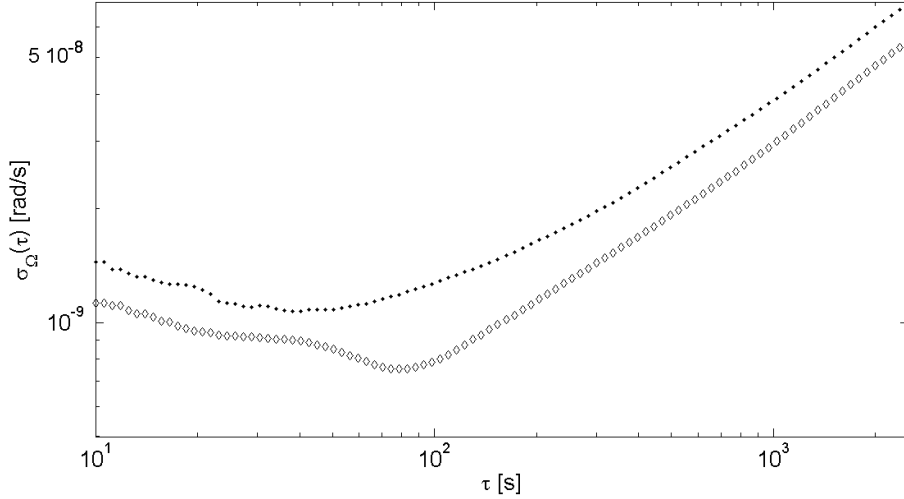


Figure 14: *Allan* deviation of the rotation rate estimated by *AR(2)* method (dots) and *EKF* (open diamonds) using  $2 \times 10^4$  seconds of experimental data of *G-PISA*. An increase of a factor of 1.5 in rotation-rate resolution and of a factor of 2 in the time stability is observed.

The calibration of the monitor signal is obtained by performing intensity steps in the neighborhood of the monomode working regime of the *RL*, exploiting the identification procedure described in Section 2.4, and a linear least squares fit.

The *RL G-PISA* is operated with a gas mixture of 50%  $^{20}\text{Ne}$  and 50%  $^{22}\text{Ne}$ , at a total pressure of 7.5 mbar. The monument of *G-PISA* is oriented toward the local North direction and allows to hold the granite table with a tilt angle equal to the latitude of the laboratory. The positioning of monument has been done by using topographic references (angle with the north) and an inclinometer (angle with the local vertical). The estimated error in the monument orientation was estimated to be less than  $< 1^\circ$ . In this configuration, the *Sagnac* frequency signal due to the Earth rotation is maximum, and the rotation rate of the instrument is more stable in time. This is the best condition for reducing the environmental disturbances, and for the systematic study of the laser dynamics.

#### 2.5.2.4 *Sagnac Frequency estimation results with calibration*

We implemented the estimation and calibrations routines for *G-PISA* described in the previous sections. In addition, we also implemented a data quality criterion that discards large outliers due to electronic spikes. To get an estimation of the plasma temperature, gas pressure and isotopic concentration, we fit the normalized measures of a laser diode on the standard *He – Ne* gas mixture to the function  $z^{(0)}(\xi)$  in Eq.(27), see Fig.15. To account for detuning uncertainties in the laser probe, we scaled the experimental abscissa so that  $\xi' = a'\xi + b'$ ,  $\xi'' = a''\xi + b''$ . The fit parameters are  $a'$ ,  $b'$ ,  $\eta'$ ,  $k'$ ,  $a'' = \sqrt{22/20}a'$ ,

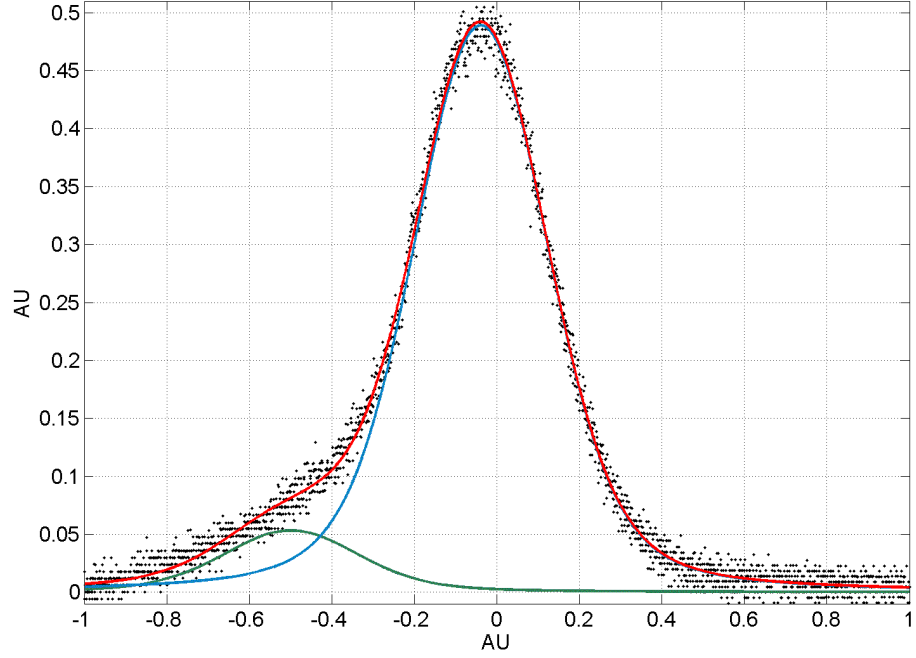


Figure 15: *Doppler* profile of the closed optical transition in Neon at 640.2 nm, allowing for the Neon temperature estimation. The measurement is taken in typical operation conditions for a plasma of *He – Ne* standard mixture at 4.5 mbar. Using the standard Matlab procedure for fitting custom functions, we get a reduced R-squared of 0.9947 and the fitting parameters  $a' = -4.9 \pm 0.1$ ,  $b' = -2.44 \pm 0.05$ ,  $k' = 0.65 \pm 0.02$ ,  $\eta' = 0.27 \pm 0.02$ .

$b'' = \sqrt{22/20}b'$ ,  $k'' = \sqrt{22/20}k'$ , and  $\eta'' = \sqrt{22/20}\eta'$ . From the fit results, we get  $T_{Ne} = (360 \pm 12) K$ , giving  $\eta_{20} \sim 0.27 \pm 0.02$ , and  $\eta_{22} \sim 0.28 \pm 0.02$ , see Fig.15 for details.

In Fig.16 we report the results of the ring down time measurements, the losses for the two beams were estimated as  $\mu_1 = (1.136 \pm 0.02) \times 10^{-4}$ ,  $\mu_2 = (1.146 \pm 0.02) \times 10^{-4}$ . Notice that within the precision of the fit it is  $\mu_1 \sim \mu_2$ .

Fig.17 shows the calibration line of the single pass gain as a function of  $V_p$ , and the experimental data used for the linear fit.

Once the calibration of the experimental apparatus has been performed, we have used the monobeam intensity offsets, modulation amplitudes and phases, and the gain monitor to estimate both cold cavity and active medium parameters. The intensity and interferogram data, sampled at 5 kHz, were collected in two days. We compared the performances of the *EKF* routine devised with *AR(2)*, the standard frequency detection algorithm for *RL* beat note [63].

Fig.18 shows the histograms of the *AR2* and *EKF* estimates. Note that the *EKF* mean is shifted with respect to *AR2* mean (effective removal of the frequency null shift), and that the *EKF* standard deviation is  $\sim 10$  times smaller than the standard deviation of *AR2* es-

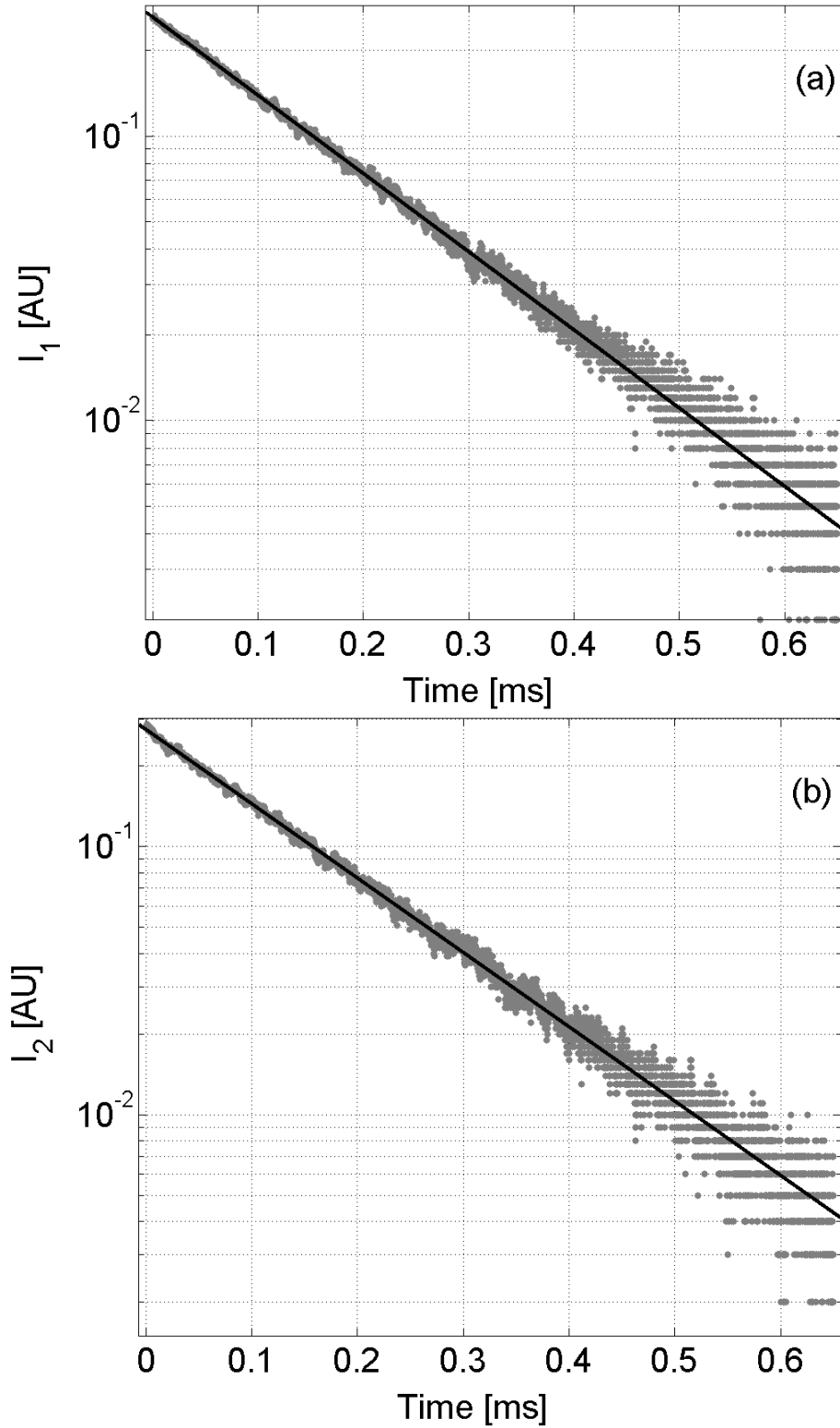


Figure 16: Plot of *RDT* data sampled at 10 MHz with the fitting functions  $n_{1,2} \exp(-\mu_{1,2}ct/L)$  for clockwise (a) and counter-clockwise (b) beams, respectively. The reduced *R*-squared from Matlab fitting toolbox are  $R_1^2 = 0.9969$ , and  $R_2^2 = 0.9955$ , and the fitting parameters are  $\mu_1 = (1.136 \pm 0.02) \times 10^{-4}$ ,  $\mu_2 = (1.146 \pm 0.02) \times 10^{-4}$ ,  $n_1 = (1.898 \pm 0.005) \times 10^{-1}$ ,  $n_2 = (1.982 \pm 0.005) \times 10^{-1}$ .

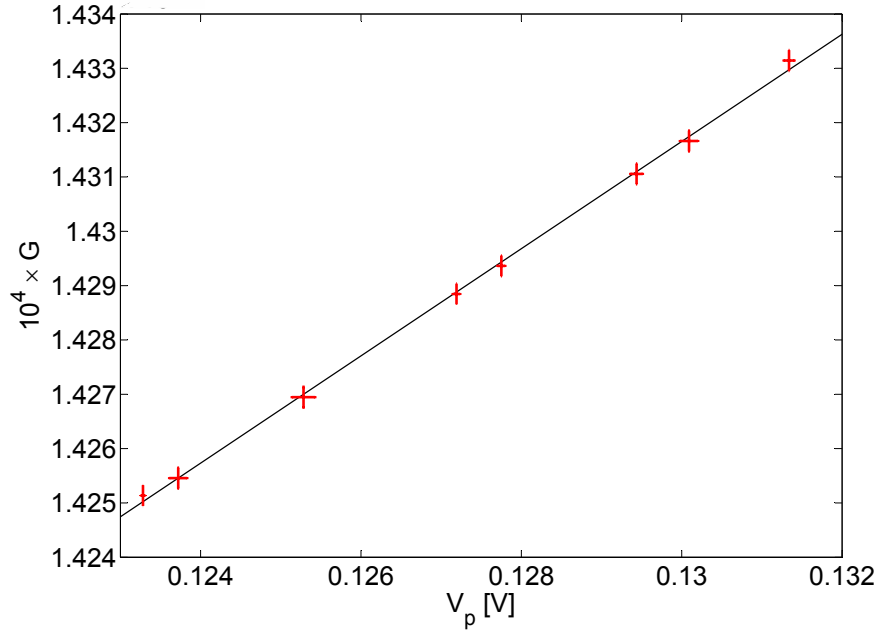


Figure 17: Plot of single pass gain of  $G$ -PISA as a function of the gain monitor  $V_p$ . Each point represents the average of 10 measurements and the corresponding error bar is their standard deviation. The linear fit gives  $a = 9.87 \times 10^{-5}$ ,  $b = 1.303 \times 10^{-4}$ ,  $\sigma_a = 1.57 \times 10^{-6}$ , and  $\sigma_b = 2 \times 10^{-7}$ .

timator. The  $G$ -PISA long-term stability and accuracy have been so increased.

Moreover, Fig.19 displays the *Allan* deviation of the two estimates ( $AR(2)$  and  $EKF$ ), and the reference curve of the *Allan* deviation for a frequency signal corrupted by shot noise.

Table 4 summarizes the systematic error contributions to rotation rate accuracy of  $G$ -PISA. For middle size  $RLG$  backscattering phenomena are the most important systematic error source. The noise filtering algorithm developed in this work promises to be also effective in improving the long term stability of larger  $RLGs$ . For instance, we know from Monte Carlo simulations that to filter out a relative backscattering contribution of 1 part in  $10^8$  from the *Sagnac* frequency, the inaccuracy on the laser dynamics parameters should be of the order of 1 part in  $10^5$ .

### 2.5.3 Analysis of $G$ -WETTZELL data

We have applied the laser systematic subtraction algorithm to the  $RLG$   $G$ -WETTZELL. The intensity and interferogram data, sampled at 2 kHz, were collected in almost one month. We could not apply the calibration routine because the auxiliary measurements for estimating the laser gain and the calibration constants for the detectors

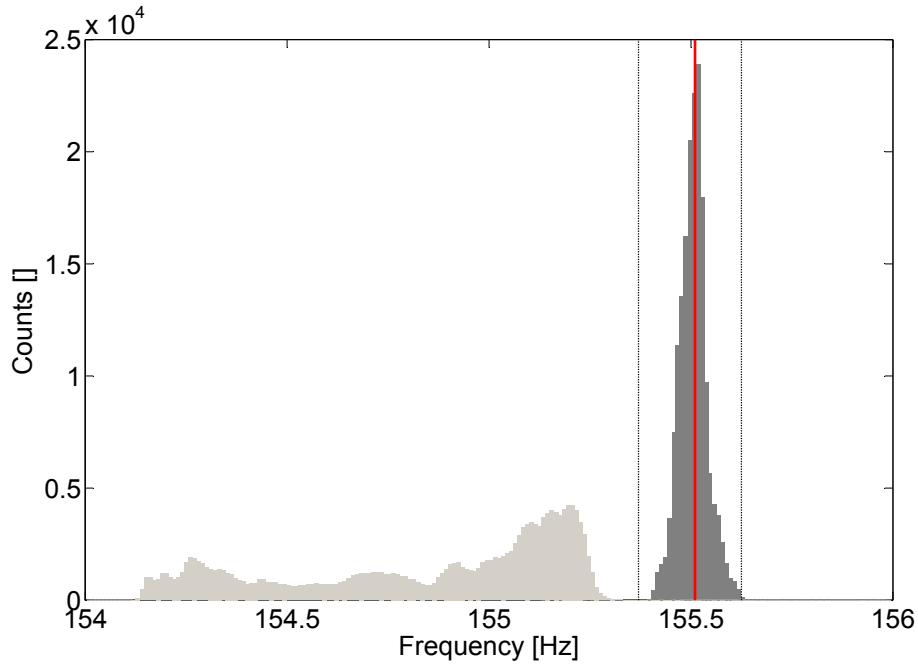


Figure 18: Histograms of the estimates of  $AR(2)$  (pale gray) and  $EKF$  (dark gray) during 2 days of  $G$ - $PISA$  data. The grey rectangular area represents the residual uncertainty on the predicted *Sagnac* frequency, due to geometric and orientation tolerances. Note that the  $EKF$  mean is shifted with respect to  $AR(2)$  mean (removal of null shift contribution), and that the  $EKF$  standard deviation is  $\sim 10$  times lower than the  $AR(2)$  standard deviation (increasing of long-term stability).

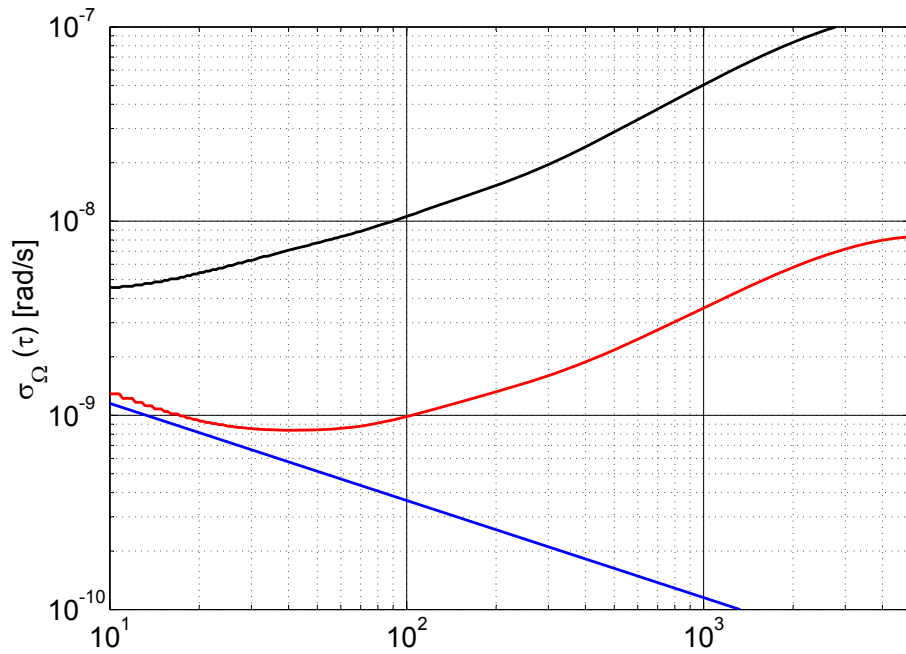


Figure 19: *Allan* deviations of  $AR(2)$  (upper curve) and  $EKF$  (lower curve) rotational frequency estimates. The straight line represents the shot noise level of  $G$ - $PISA$  for a cavity quality factor of  $5.4 \times 10^{11}$  and an output power of 4 nW.

Error Source	Freq. error
Back-scattering $\mathcal{R}_2 e^{-X} + \mathcal{R}_1 e^X + \text{c.c.}$	0.4695 Hz
Null Shift $\tau (I_1 - I_2)$	$-8.7 \times 10^{-4}$ Hz
Atomic Scale Factor $\sigma_1 - \sigma_2$	$5.56 \times 10^{-6}$ Hz
Cross Dispersion $I (\tau_{21} - \tau_{12})$	$1.75 \times 10^{-6}$ Hz

Table 4: Contributions to the accuracy budget of *G-PISA* from systematic errors in the estimate of *Lamb* parameters.

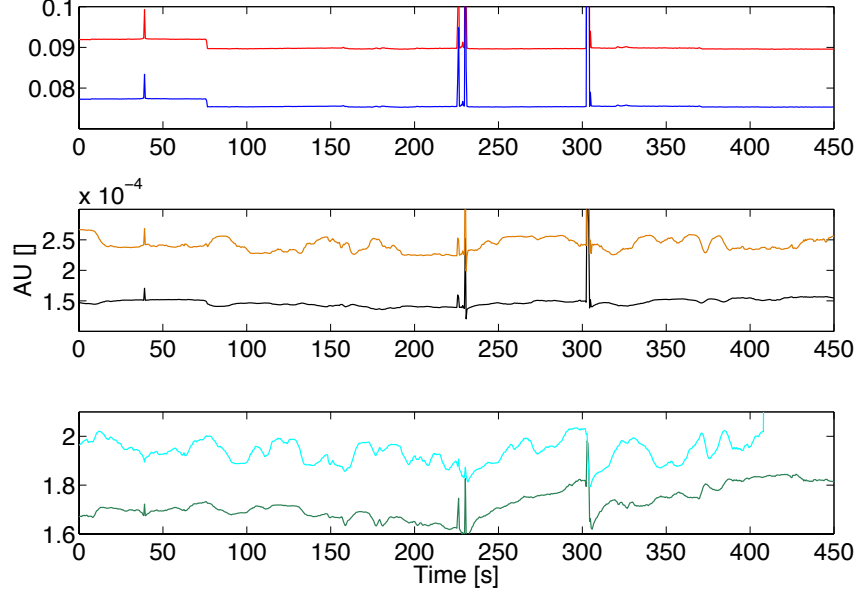


Figure 20: Plot of the means  $I_{1,2}$  (top box), of the modulations  $i_{1,2}$  (middle box) and of the phases  $\phi_{1,2}$  as estimated by the pre-filtering routine from the time series of  $I_1(t)$ ,  $I_2(t)$  and  $S(t) \sim \sin(\psi(t))$  using the experimental data of *G-WETTZELL*.

were not available. However, the engineer that operates the ring gave us the nominal values of calibration constants for detectors, round trip losses, pressure and temperature of the gas mixture, so we were able to complete our analysis. However, to achieve greater precision in the systematic subtraction, we firstly collect all the computed corrections to the beat frequency and then fit them to experimental data on time periods of several days, in this way we retain good results even without the experimental calibration.

In Fig.20 we show the results of the pre-filtering procedure, note that the ratio between the monobeam modulations  $i_{1,2}$  and the monobeam means  $I_{1,2}$  is two order of magnitude smaller than in *G-PISA* data, this is due to the greater dimensions of the *G-WETTZELL* optical path.

In Fig.21 we show the results of the laser parameter identification procedure, it should be noted that, as we have no experimental calibration available, the units of  $\alpha_{1,2}$  and  $r_{1,2}$  are arbitrary.

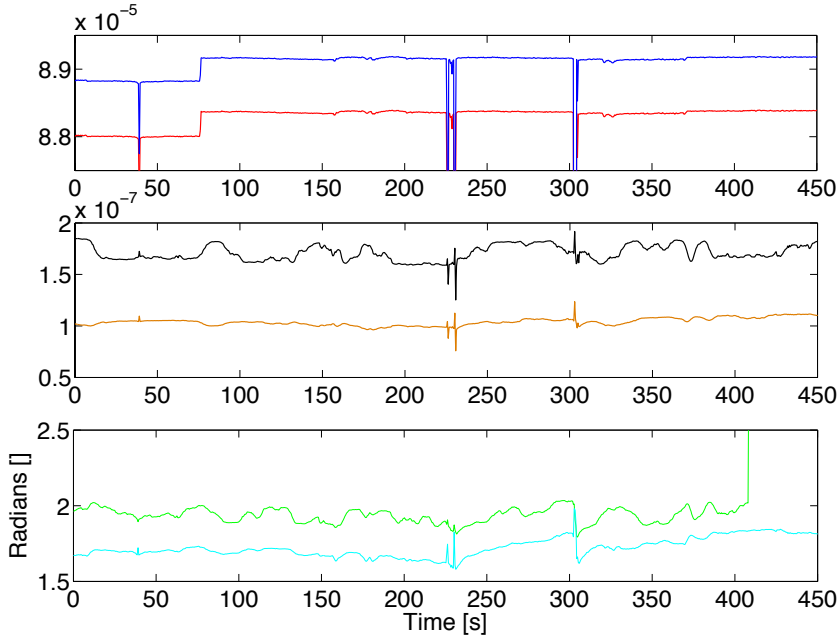


Figure 21: Time series of the  $\alpha_{1,2}$ ,  $r_{1,2}$  and  $\varepsilon_{1,2}$  estimated using the experimental data of *G-WETTZELL*.

In Fig.22 we show good correlations between our estimation of the laser systematics and  $AR(2)$ . The selected data correspond to several days in which the laser parameters does not vary significantly.

In Fig.23 we finally show the *Allan* deviation of  $AR(2)$  after the subtraction of the estimation of the laser systematics, for the 180 h of the second plot of Fig.22. We note that  $i_{1,2}$  and  $\phi_{1,2}$  exhibit larger variations than  $I_{1,2}$ , therefore light backscattering is the main systematic error source. In fact, the backscattering subtraction by our methods improved the *Allan* deviation on the  $10^5$  s timescale.

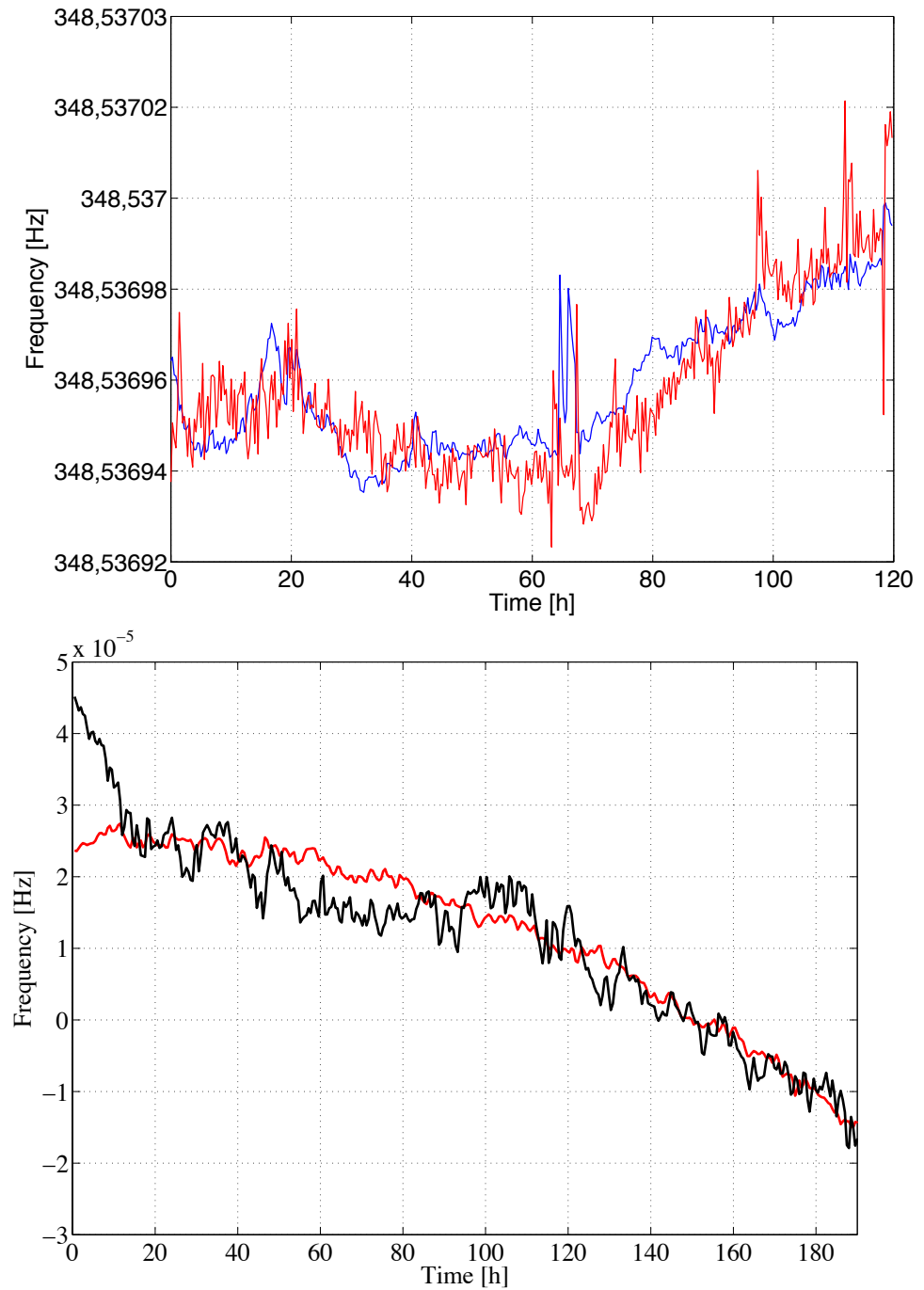


Figure 22: Comparison between the  $AR(2)$  estimation of *G-WETTZELL* beat frequency (black and blue lines) and the estimation of the laser systematics (red lines). In the second plot the mean values of the signals have been removed.



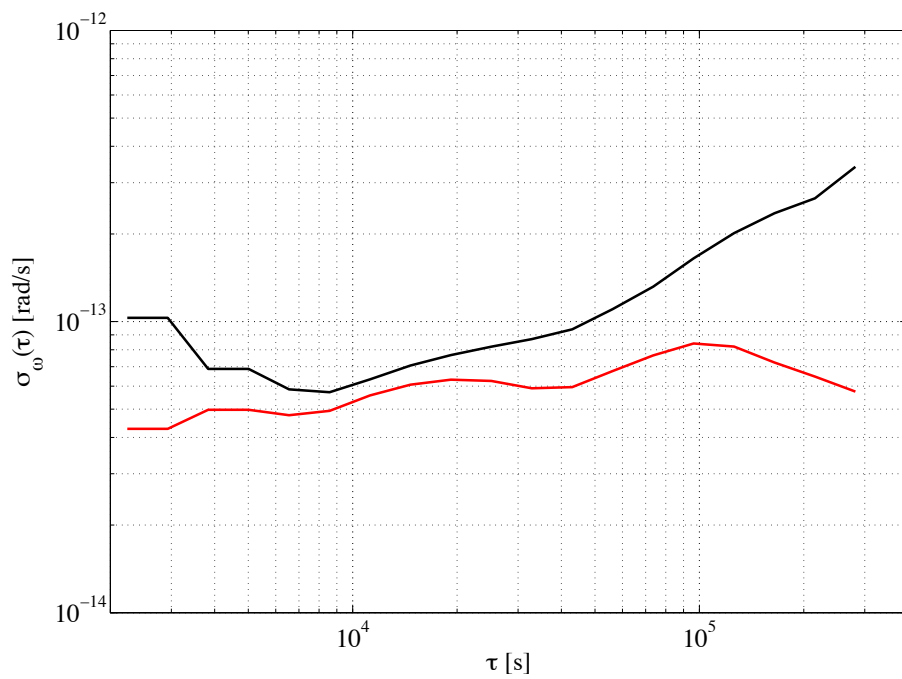


Figure 23: *Allan* deviation of the same data of Fig.22, with ( red line ) and without ( black line ) the subtraction of the laser systematics.



In this Chapter we address the study of the light path in resonant cavities. A model based on geometric optics is proposed to compute the laser beams position for given mirrors displacements. By exploiting the *Fermat's* principle, we develop a novel method to compute the beam directions in resonant optical cavities formed by spherical mirrors, as a function of mirror positions and curvature radii. These results are of some importance for the design and alignment control of the optical cavities of high accuracy *RLGs*. Afterwards we present a method to decompose the mirror coordinate matrix of a square *RL*, in order to separately account for shape and pose of the resonant cavity. On the one hand, this decomposition allows to distinguish between changes in the shape and changes in the rigid displacement of the resonant cavity; on the other hand, it provides a bijective map between the coordinates of the *RL* mirrors and their distances.

### 3.1 COMPUTING THE LASER BEAM PATH IN OPTICAL CAVITIES

In three-dimensional resonant optical cavities, laser light travels a closed path formed by  $N > 2$  mirrors that are centered at the vertices of non-planar polygons (a polygon is non-planar if its vertices do not lie in the same plane). The cavity has a perimeter length  $p$ , and encloses a vector area  $\mathbf{a}$ . With such geometric properties we can form the compactness ratio of a ring cavity  $\mathbf{k}_s \equiv \mathbf{a}/p$ , which is the relevant geometrical quantity for the absolute calibration of *RLGs* [35, 59]. Generally, the increase of the optical path length  $p$  results in higher sensitivity measuring devices and, at the same time, in more demanding requirements for the mirrors positioning or beam alignment. Indeed, the long term stability of a cavity also decreases as a function of its size. The reasons thereof is twofold: i) the intrinsic noise limiting the sensitivity of a cavity is the shot noise, and its magnitude turns out to be inversely proportional to  $p$ ; and ii) changes of the environmental conditions (e.g. temperature and pressure drifts) during measurement processes induce deformations of the optical cavity which result in a beam-jittering noise with magnitude almost proportional to  $p$ . Even if a trade off can eventually be made between the intrinsic and beam-jittering noises, to increase sensitivity and stability of an optical cavity, the latter noise must be reduced as much as possible. In order to be less sensitive to beam-jittering noise, an optical cavity can have either a monolithic or eterolithic designs. In the monolithic approach, one exploits an ultra low expansion coefficient material (e.g. *Zerodur*

or *Invar*) to form a “rigid” reference frame for the mirrors, and may, in case, add some passive stabilization of the cavity geometry by stabilizing pressure and temperature of the environment. For instance, the 4 m side square cavity of *G-WETTZELL* [60], nowadays the most sensitive and stable *RLG* for geodetic and seismic applications, has a monolithic design. However, an heterolithic design of optical cavities should be much more effective to fight against mirror displacements when *RLs* must be large and arranged in triaxial configurations [14]. In such approach, mirrors are fixed to a concrete or granite frame and equipped with handlers to react against changes in their relative positions, and so stiffening the geometry of the apparatus. The geometry can be also optimized to reduce the cavity sensitivity to the beam-jittering noise, e.g. by adjusting the beams path to regular polygonal shapes. Clearly, the heterolithic design requires also the identification of suitable signals, provided e.g. by some metrological precision system, proportional to mirror displacements.

The calculation of the beam directions in resonant optical cavities is relatively recent [85, 57]. In particular, generalized ray transfer matrices analysis is based on the optical axis perturbation, by means of a suitable coordinate system, and ray tracing methods iteratively propagates beams until a closed polygonal configuration is reached. On the other hand, the geometric Newton algorithm and the *Fermat's* principle allow us to calculate efficiently the beams position in a cavity as a function of the mirror positions and orientations. In particular, the beams position of a cavity made of spherical mirrors can be calculated starting from the positions of their centers of curvature. The calculation of the beam path is the first step to develop efficient control strategies to keep fixed either the geometry of a cavity and the relative angles among different cavities, which is the most demanding requirement for the application of a triaxial system of *RLs* to fundamental physics [14].

### 3.1.1 *Notation and Definitions*

We assume a knowledge of the theory of finite dimensional smooth manifolds and covariant differentiation. We refer to the books [1, 48] for a review on differentiable manifolds and covariant differentiation.

## 3.1.1.1 Notation

$\mathcal{E}$	Euclidean space $\mathcal{E}$ .
$\mathcal{M}, \mathcal{N} \subseteq \mathcal{E}$	Embedded Submanifolds $\mathcal{M}, \mathcal{N} \subseteq \mathcal{E}$ .
$x \in \mathcal{M}$	Element $x$ of the manifold $\mathcal{M}$ .
$f : \mathcal{M} \rightarrow \mathbb{R}$	Real valued function on $\mathcal{M}$ .
$\bar{f} : \mathcal{E} \rightarrow \mathbb{R}$	$\bar{f} = f$ on $\mathcal{M} \subset \mathcal{E}$ .
$\mathfrak{F}(\mathcal{M})$	The set of smooth real valued functions on $\mathcal{M}$ .
$\mathfrak{F}_x(\mathcal{M})$	The set of smooth real valued function defined near $x \in \mathcal{M}$ .
$T_x\mathcal{M}$	The tangent space to $\mathcal{M}$ at $x \in \mathcal{M}$ .
$\xi_x \in T_x\mathcal{M}$	The tangent vector $\xi_x$ to $\mathcal{M}$ at $x$ .
$\mathfrak{X}_x(\mathcal{M})$	The set of smooth vector fields on $\mathcal{M}$ near $x$ .
$\xi \in \mathfrak{X}_x(\mathcal{M})$	Smooth vector field $\xi : x \mapsto \xi_x$ on $\mathcal{M}$ at $x$ .
$DF : T_x\mathcal{M} \rightarrow T_{F(x)}\mathcal{N}$	The tangent map of $F : \mathcal{M} \rightarrow \mathcal{N}$ at $x$ .
$\partial f(x) \in T_x\mathcal{E}$	Euclidean Gradient of $f : \mathcal{E} \rightarrow \mathbb{R}$ .
$\partial^2 f(x) : T_x\mathcal{E} \rightarrow T_x\mathcal{E}$	Euclidean Hessian of $f$ .
$\langle \cdot, \cdot \rangle_{\mathcal{M}} : T_x\mathcal{M} \times T_x\mathcal{M} \rightarrow \mathbb{R}$	Riemannian metric on $\mathcal{M}$ .
$\nabla : T_x\mathcal{M} \times \mathfrak{X}_x(\mathcal{M}) \rightarrow \mathfrak{X}_x(\mathcal{M})$	Riemannian connection on $\mathcal{M} \subset \mathcal{E}$ .
$\text{grad } f(x) \in T_x\mathcal{M}$	Riemannian Gradient of $f : \mathcal{M} \rightarrow \mathbb{R}$ .
$\text{Hess } f(x) : T_x\mathcal{M} \rightarrow T_x\mathcal{M}$	Riemannian Hessian of $f$ .
$\mathbb{S}^2$	Unit Sphere $\{\mathbf{x} \in \mathbb{R}^3, \mathbf{x}^T\mathbf{x} = 1\}$
$\wedge$	Canonical cross product between vectors of $\mathbb{R}^3$ .
$\otimes$	Kronecker product
$d : \mathbb{R}^{n \times n} \mapsto \mathbb{R}^{n \times n}$	$d(A)_{ij} = \begin{cases} A_{ij} & i = j \\ 0 & i \neq j \end{cases}$

The Riemannian connection  $\nabla$  is determined by the condition

$$D \langle \xi_x, \chi_x \rangle_{\mathcal{M}} [\eta_x] = \langle (\nabla_{\eta_x} \xi)_x, \chi_x \rangle_{\mathcal{M}} + \langle \xi_x, (\nabla_{\eta_x} \chi)_x \rangle_{\mathcal{M}}, \quad (55)$$

where  $x \in \mathcal{M}$ ,  $\eta_x \in T_x\mathcal{M}$ , and  $\xi, \chi \in \mathfrak{X}_x(\mathcal{M})$ , i.e. it is the unique connection that is compatible with the Riemannian metric  $\langle \cdot, \cdot \rangle_{\mathcal{M}}$  of  $\mathcal{M}$ . Moreover, if  $\mathcal{M} = \mathcal{E}$ , we have that the covariant derivative associ-

ated to the Riemannian connection of the vector field  $\xi$  with respect to  $\eta_x$  is simply the directional derivative, i.e.  $\nabla_{\eta_x}\xi = D\xi[\eta_x]$ .

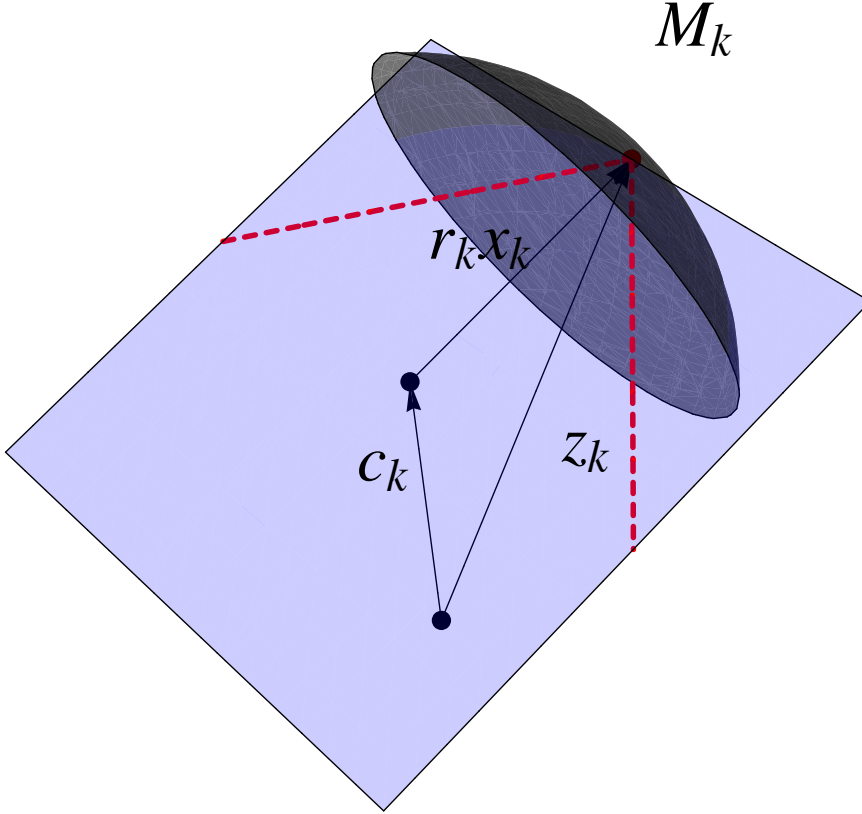


Figure 24: Parametrization of the position of the laser spot on the  $k$ -th mirror. With respect to the inertial frame origin  $O$ , the position of laser spot is  $\mathbf{z}_k = r_k \mathbf{x}_k + \mathbf{c}_k$ . The mirror  $M_k$  has radius  $r_k$ . Relative to the mirror center  $\mathbf{c}_k$ , the position of the laser spot can be parametrized as  $r_k \mathbf{x}_k$ ,  $\mathbf{x}_k \in \mathbb{S}^2$ .

### 3.1.2 Problem Statement for a RL cavity

We consider an optical cavity formed by  $N$  spherical mirrors. Indicating with  $\mathbf{z}_k$  the coordinates in  $\mathbb{R}^3$  of the position of the light spot on the  $k$ -th mirror with respect to a common reference frame, the cavity has a perimeter length  $p = \sum_{k=1}^N \|\mathbf{z}_k - \mathbf{z}_{k+1}\|$ , and encloses a vector area  $\mathbf{a} = \frac{1}{2} \sum_{k=1}^N \mathbf{z}_k \wedge \mathbf{z}_{k+1}$ , where  $\mathbf{z}_{N+1} := \mathbf{z}_1$ . Applying the formalism of geometric optics, we can model the  $k$ -th spherical mirror  $M_k$  as a sphere of center  $\mathbf{c}_k \in \mathbb{R}^3$  and curvature radius  $r_k \in \mathbb{R}^+$ . Making use of the mirror center position  $\mathbf{c}_k$ , the position of the laser spot on the  $k$ -th mirror can be expressed as  $\mathbf{z}_k = \mathbf{c}_k + r_k \mathbf{x}_k$ , where  $r_k$  is the mirror curvature radius and  $\mathbf{x}_k \in \mathbb{S}^2$ . For a graphical representation of this fact, see Figure 3.1.24.

A *configuration* for the laser beams in the optical cavity is defined as the ordered set of points  $X = (\mathbf{x}_1, \dots, \mathbf{x}_N)$ , which account for the beams positions in the cavity. In addition, we define the matrix of centers  $C = (\mathbf{c}_1, \dots, \mathbf{c}_N)$ , and the matrix of curvature radii  $R = \text{diag}(r_1, \dots, r_N)$ . We refer to  $R$  and  $C$  as the *parameters* of the

optical cavity. Given the cavity parameters  $R$  and  $C$  and a configuration  $X$ , the corresponding laser beams path as well as the associated (scalar and vector) fields  $p$ ,  $a$ , and  $k_s$  (see Section 3.1) can be computed. Since not every configuration  $X$  is allowed, we have to compute the physical beam position given the cavity parameters  $R$  and  $C$ . To this aim we resort to the *Fermat's* principle, and impose the stationarity of the optical path  $p$  with respect to  $X$ . To this end, we use a geometric approach, exploiting explicitly the fact that the laser spot at each mirror is constrained to live on a sphere.

A modern formulation of the *Fermat's* principle is that rays of light traverse the path of stationary optical length with respect to variations of the path [3]. In our model for resonant cavities the optical path length is function of the laser spot position  $\{(\mathbf{x}_1, \dots, \mathbf{x}_N) : \mathbf{x}_k \in \mathbb{S}^2\}$  with parameters  $C$  and  $R$ . This set is isometric to the cartesian product of  $N$  unit 3-spheres  $\mathbb{S}^2$ . As each unit 3-sphere inherits a smooth differential structure from  $\mathbb{R}^3$ , the set of  $X$  inherits a smooth differential structure from  $\mathbb{R}^{3 \times N}$  [1]. Therefore  $\{(\mathbf{x}_1, \dots, \mathbf{x}_N) : \mathbf{x}_k \in \mathbb{S}^2\}$  corresponds to an embedded submanifold of  $\mathbb{R}^{3 \times N}$ . This manifold is usually called the Oblique Manifold of dimension  $2 \times N$ . In general, the Oblique Manifold of dimension  $n \times m$  is defined as

$$\mathcal{OB}(n, m) = \left\{ X \in \mathbb{R}^{(n+1) \times m}, d \left( X^T X \right) = I_{m \times m} \right\} \cong \underbrace{\mathbb{S}^n \times \dots \times \mathbb{S}^n}_m, \quad (56)$$

and its tangent space at  $X$  is

$$T_X \mathcal{OB}(n, m) = \left\{ Y \in \mathbb{R}^{(n+1) \times m} : d(X^T Y) = 0_{m \times m} \right\}, \quad (57)$$

which means that each column of  $X$  is orthogonal to the corresponding column of  $Y$ , with respect to the (Riemannian) metric of  $\mathbb{R}^{n+1}$ ,  $\langle \mathbf{x}, \mathbf{y} \rangle_{\mathbb{R}^{n+1}} = \mathbf{x}^T \mathbf{y}$ . It is worth mentioning that  $\mathcal{OB}(n, m)$  inherits the Riemannian metric of  $\mathbb{R}^{n \times m}$ , i.e.  $\langle X, Y \rangle_{\mathcal{OB}(n, m)} = \text{tr} (X^T Y)$ .

A *physical configuration*  $\hat{X}$  is any element of the set of stationary points for the optical path  $p$ , defined as

$$\{X \in \mathcal{OB}(2, N) : T_X \mathcal{OB}(2, N) \ni \text{grad } p(X; C, R) = 0\}. \quad (58)$$

The set (58) can contain 2 or more elements being  $p$  a continuous function defined over a compact set  $\mathcal{OB}(2, N)$ , also the elements of (58) depends on the values of  $C$  and  $R$ . Finding closed form expressions for the elements of (58) is generally not possible, therefore we resort to a numerical algorithm. Interest is put in computing the laser beams positions on mirrors for optical cavities slightly misaligned from an ideal design model, in which the beams path is known, therefore a local approach to the optimization is justified. In particular, we



make use of a geometric version of the classical Newton method that takes into account the geometry of the search, in order to speed up calculations retaining accuracy.

### 3.1.3 Review of the Geometric Newton Algorithm

In the recent literature many authors addressed the geometric formulation and extension of classical algorithms, e.g. the Newton Algorithm. We follow the works of *J.P. Absil* and others [1, 2], that outlined an intrinsic formulation of the Newton algorithm to embedded submanifolds. The starting point is the well known iterative scheme of the multidimensional Newton algorithm for a function  $f : \mathbb{R}^n \mapsto \mathbb{R}$ . The algorithm involves the computation of the Euclidean gradient  $\partial f(\mathbf{x})$ , and the inverse of the Euclidean Hessian  $\partial^2 f(\mathbf{x})[\eta]$ . In this Section we review the extensions of the Newton algorithm to find stationary points of functions defined on an embedded submanifold of  $\mathbb{R}^n$  [1].

Given a smooth manifold  $\mathcal{M}$  and a real valued function  $f \in \mathfrak{F}(\mathcal{M})$  defined on  $\mathcal{M}$ , we build at each iteration  $x_k \in \mathcal{M}$  a quadratic model for  $f$  [1]

$$f(x_k, \eta_{x_k}) = f(x_k) + \langle \text{grad } f(x_k), \eta_{x_k} \rangle + \frac{1}{2} \langle \text{Hess } f(x_k)[\eta_{x_k}], \eta_{x_k} \rangle \quad (59)$$

where a connection  $\nabla$  is used in the computation of the Hessian. The stationary points of the local quadratic model are given by the Geometric Newton Equation

$$\text{Hess } f(x_k)[\eta_{x_k}] = -\text{grad } f(x_k) \quad (60)$$

$$\eta_{x_k} \in T_{x_k} \mathcal{M} \quad (61)$$

that provides a descent direction for the real valued function  $h = \|\text{grad } f\|$ . Note that the equation lives in the tangent space at the current iterate. Once the descent direction  $\eta_{x_k}$  has been computed solving (60), a map from  $T_{x_k} \mathcal{M}$  to  $\mathcal{M}$  is needed to compute the next iterate. Such a map, in principle, should be the exponential map associated to the Riemannian connection of  $\mathcal{M}$ . In practice, especially when computing the exponential map is expensive, a suitable approximation of the exponential map (that agrees up to the second derivative at the origin) can be used. Such a map is called a *retraction* [1], when computing the exponential map is difficult, computations can be substantially speeded up. The basin of attraction of the (geometric) Newton algorithm can be increased by employing a line search method to adjust the step length in the optimal descent direction  $\eta_{x_k}$ . Since we are searching for stationary points, the function  $h$  will be minimized

along the search direction. Here we employ the efficient line search algorithm, named *Armijo's* backtracking line search method [6]. Once the search direction and the step size have been found, the next iterate is computed and the procedure described above is repeated until a termination condition is met.

The geometric Newton algorithm with line search can be summarized as follows

---

**Algorithm 3.1** Geometric Newton with line search.

---

*Input:*  $x_0 \in \mathcal{M}$ , real valued function  $f$  on  $\mathcal{M}$

*Output:* Sequence of iterates  $x_1, \dots, x_n$

1. *Search Direction:* solve (60) in  $\eta_{x_k}$ .
  2. *Step Size:* find  $t_k = \arg \min_{\lambda} \|\text{grad } f(R(\lambda \eta_x))\|^2$
  3. *Update:* Set  $x_{k+1} = R_x(t_k \eta_{x_k})$
- 

In the following, we detail how to solve the search direction sub-problem (60). If the manifold  $\mathcal{M}$  is embedded in the Euclidean Space  $\mathcal{E}$ , we can exploit the geometry of the ambient space for computation purposes. In fact, we can represent both points in  $\mathcal{M}$  and vectors in  $T_x \mathcal{M}$  as elements of  $\mathcal{E} \simeq T_x \mathcal{E}$ , and use the Riemannian connection of  $\mathcal{E}$  to compute covariant derivatives on  $\mathcal{M}$ .

**GEOMETRIC NEWTON EQUATION** Let  $\mathcal{M}$  denote a manifold endowed with a Riemannian metric  $\langle \cdot, \cdot \rangle_{\mathcal{M}}$ . Given a point  $x \in \mathcal{M}$ , and a function  $f \in \mathfrak{F}(\mathcal{M})$ , the Newton equation update for  $f$  at  $x$  is a system of equations linear in the argument  $\eta_x$ , as  $\text{Hess } f(x)[\eta_x]$  is a linear operator in the argument  $\eta_x$ .

The Riemannian gradient and Hessian  $\forall x \in \mathcal{M}$  are defined by

$$\begin{cases} \langle \text{grad } f(x), \xi_x \rangle_{\mathcal{M}} &= Df(x)[\xi_x] \\ \text{Hess } f(x)[\eta_x] &= (\nabla_{\eta_x} \text{grad } f)_x \end{cases}, \quad (62)$$

and they can be evaluated exploiting the geometry of the ambient space  $\mathcal{E}$ . The approach of Ref.[1] shows how to compute a representation of vectors in  $T_x \mathcal{M}$  by orthogonal projection of vectors in  $T_x \mathcal{E}$ . This representation is handy since elements in  $T_x \mathcal{E}$  can be represented in the same way of elements of  $\mathcal{E}$  itself, therefore the same representation in  $\mathcal{E}$  is used for elements in  $\mathcal{M}$ ,  $T_x \mathcal{M}$  and  $T_x \mathcal{E}$ . Moreover, in Ref.[1] its shown how to compute the Riemannian gradient and Hessian of  $f$ , and thus exploit second order information on the function  $f$  defined on  $\mathcal{M}$ , by means of the orthogonal projections of the gradient and Hessian of  $\bar{f}$ , where  $\bar{f}$  is any smooth extension of  $f$  in

$\mathcal{E} \supseteq \mathcal{M}$ . The gradient and Hessian of  $\bar{f}$  in  $\mathcal{E}$ ,  $\partial\bar{f}$  and  $\partial^2\bar{f}[\eta]$ , are called Euclidean gradient and Hessian.

**TANGENT SPACE PROJECTION** To derive  $\text{grad } f$  and  $\text{Hess } f$ , starting from the corresponding operators in  $\mathcal{E}$ , we use the projection tool developed in ref. [1].

The orthogonal projection operator

$$\begin{aligned} P_x : T_x\mathcal{E} &\rightarrow T_x\mathcal{M} \\ \xi_x &\mapsto P_x(\xi_x) \end{aligned} \quad (63)$$

maps every tangent vector  $\xi_x$  of  $T_x\mathcal{E}$  into its orthogonal projection onto  $T_x\mathcal{M}$ . In addition, every tangent vector  $\xi_x$  in  $T_x\mathcal{E}$  admits the unique decomposition  $\xi_x = \eta_x + \nu_x$ , in terms of elements  $\eta_x \in T_x\mathcal{M}$  and  $\nu_x \in (T_x\mathcal{M})^\perp$ , where  $(T_x\mathcal{M})^\perp$  is the normal space of  $\mathcal{M}$  at  $x$ , i.e. the orthogonal complement of  $T_x\mathcal{M}$  to  $T_x\mathcal{E}$ . We have  $\eta_x = P_x(\xi_x)$  and  $\nu_x = \xi_x - P_x(\xi_x)$ .

**RIEMANNIAN GRADIENT** The connection between the Riemannian gradient  $\text{grad } f$  of a function  $f$  from  $\mathcal{M}$  to  $\mathbb{R}$ , and  $\partial\bar{f}$ , the Euclidean gradient of a local smooth extension  $\bar{f}$  of  $f$  into  $\mathcal{E}$  is given by

$$\forall x \in \mathcal{M}, \text{grad } f(x) = P_x(\partial\bar{f}(x)) , \quad (64)$$

$x$  here denotes the canonical immersion of  $x \in \mathcal{M}$  into  $\mathcal{E}$  [1].

**RIEMANNIAN HESSIAN** In analogy with the Riemannian gradient, the Riemannian Hessian  $\text{Hess } f$  of  $f$  at  $x$ , can be computed as the orthogonal projection onto  $T_x\mathcal{M}$  of the tangent map of the extension to  $\mathcal{E}$  of the vector field  $\text{grad } f$ . Denoting with

$$D \text{grad } \bar{f}(x) : T_x\mathcal{E} \mapsto T_x\mathcal{E} \quad (65)$$

the directional derivative in  $\mathcal{E}$  of  $\text{grad } f$  regarded as a vector field on  $\mathcal{E}$ , we have

$$\forall x \in \mathcal{M}, \text{Hess } f(x)[\eta] = P_x(D \text{grad } \bar{f}(x)[\eta]) . \quad (66)$$

We stress that in general  $D \text{grad } \bar{f}(x) \neq D\partial\bar{f}(x) = \partial^2\bar{f}(x)$ , where  $\partial^2\bar{f}$  is the Euclidean Hessian of the extension  $\bar{f}$  of  $f$  [1]. At this point we can employ the projection operator  $P_x$  to compute  $\text{grad } f$  and  $\text{Hess } f$  as functions of  $\partial\bar{f}$ ,  $\partial^2\bar{f}$ ,  $D \text{grad } \bar{f}$  and  $x$ . It is not straightforward to give a general expression for  $D \text{grad } \bar{f}$  from (64), and usually this relation is expressed in terms of the *Weingarten* map, also known as shape operator [2]. For our applications, it is enough to have a specific expression of  $D \text{grad } \bar{f}(x)$  for the Oblique Manifold  $\mathcal{OB}(2, N)$ .

3.1.4 The Newton Algorithm on  $\mathcal{OB}(2, N)$ 

A point  $X \in \mathcal{OB}(2, N)$  and a tangent vectors  $\xi_X, \eta_X$  to a point  $X$  can both be represented using  $3 \times N$  dimensional matrices, i.e. as points and tangent vectors of the ambient space  $\mathbb{R}^{3 \times N}$ . Therefore, the orthogonal projection  $P_X(\xi_X)$  of  $\xi_X \in T_X \mathbb{R}^{3 \times N}$  and the directional derivative  $D \text{grad } \bar{f}(X)$  can be represented using with  $3 \times N$  dimensional matrices, as shown in Table 5. Further details and the derivation of the these expressions are given [15].

$\mathcal{M}$	$\mathcal{OB}(2, N)$
$x$	$X$
$P_x(\xi_x)$	$P_X(\xi_X) := \xi_X - d(X^T \xi_X) X$
$D \text{grad } \bar{f}(x)[\eta_x]$	$D \text{grad } \bar{f}(X)[\eta_X] = P_X(\partial^2 \bar{f}(X)[\eta_X]) - d(X^T \partial \bar{f}(X)) \eta_X$

Table 5: Expression for the coordinate representation of  $D \text{grad } \bar{f}(x)[\eta_x]$  and of  $P_x(\xi_x)$  on the Oblique manifold  $\mathcal{OB}(2, N)$ .

**SOLUTION TO THE NEWTON EQUATION** Recalling that the Newton update (60) is a system of linear equations with solution set belonging to  $T_X \mathcal{OB}(2, N)$ , which is a subspace of  $T_X \mathbb{R}^{3 \times N}$ , we illustrate a way to choose a basis of  $T_X \mathcal{OB}$  for computing the solution. The change of basis matrix will be given as a nonlinear function of  $X$ , exploiting the vectors  $X$  and  $\text{grad } f(X)$ , and employing computation of outer products and Kronecker products of  $\mathbb{R}^3$  vectors. The idea here is to exploit the geometric structure  $\mathcal{OB}(2, N)$ , seen as the Cartesian product of  $N$  unit spheres. We denote with  $\text{grad } f_k(X)$  and  $X_k$  the  $N$  columns of the matrices  $\text{grad } f(X)$  and  $X$ , and with  $\mathbf{e}_k$  the canonical basis row vectors of  $\mathbb{R}^N$ . We also consider the map  $\text{vect}(\cdot)$  that vectorize the matrix  $\xi_X \in \mathbb{R}^{3 \times N}$  into a  $3N$  dimensional column vector  $\text{vect } \xi_X$ .

**Proposition 1.** *Let  $X \in \mathcal{OB}(2, N)$  and  $f : M \mapsto \mathbb{R}$  such that  $\text{grad } f_k(X) \neq \mathbf{0}$ ,  $k = 1, \dots, N$ . Then (60) for  $f$  and  $x$  is equivalent to*

$$H(X)\mathbf{y} = \mathbf{g}(X), \mathbf{y} \in \mathbb{R}^{2N} \quad (67)$$

where

$$\begin{pmatrix} \mathbf{g}(X) \\ \mathbf{0}_{N \times 1} \end{pmatrix} = T(X) \text{vect } \text{grad } f(X), \quad (68)$$

$$T(X) = (\text{vect } \mathbf{v}_1, \dots, \text{vect } \mathbf{v}_N, \text{vect } \mathbf{w}_1, \dots, \text{vect } \mathbf{w}_N, \text{vect } \mathbf{q}_1, \dots, \text{vect } \mathbf{q}_N)^T, \quad (69)$$

$H(X)$  is the principal minor of  $T(X)\tilde{H}(X)T(X)^T$  with indexes ranging from 1 to  $2N$ ,  $\tilde{H}_{ik}(X) = \langle \mathbf{e}_i, \text{Hess } f(X)[\mathbf{e}_k] \rangle$ . Here  $\mathbf{v}_k = \text{grad } f_k(X) \otimes \mathbf{e}_k$ ,  $\mathbf{w}_k = (\text{grad } f_k(X) \wedge X_k) \otimes \mathbf{e}_k$ ,  $\mathbf{q}_k = X_k \otimes \mathbf{e}_k$ , and  $\mathbf{e}_k$  are the canonical basis vectors of  $\mathbb{R}^N$ .

The proof of Proposition 1 can be found in the Appendix. We conclude the discussion noticing that, if a column  $\text{grad } f_k(X) = \mathbf{0}$ , in the vector  $\eta_X$  representing the solution the  $k$ -th column can be taken equal to the null vector of  $\mathbb{R}^3$ , and one can rearrange the basis vectors avoiding to account for this three components in the linear equation system (60).

**RETRACTION FOR  $\mathcal{OB}(2 \times N)$**  Despite the fact that each Riemannian manifold has a natural retraction in the exponential map, different retractions are usually employed to minimize the computational costs. For  $\mathcal{OB}(2, N)$ , the map

$$R(X, \xi_X) = (X + \xi_X) d \left( (X + \xi_X)^T (X + \xi_X) \right)^{-1/2}, \quad (70)$$

i.e., the normalization to unit norm of each column of the matrix  $X + \xi_X$ , is a retraction for  $\mathcal{OB}(2, N)$  [1, 2, 15].

**ARMIJO BACKTRACKING LINE SEARCH** An effective and computationally efficient line search algorithm is *Armijo's* [6, 1]. At each iterate, the step size  $t_k$  is choose as  $t_k = \alpha \beta^l$ , with  $l$  the smallest integer such that

$$h(x) - h(R(t_k \eta_x)) \geq -\sigma \gamma_k Dh(x)[\eta_x], \quad (71)$$

for a sufficiently small parameter  $\sigma$ , with  $x$  denoting the current iterate and  $\eta_x$  the current descent direction. Here  $\alpha > 0$ , and  $\beta, \sigma \in (0, 1)$  are design parameters. Condition (71) assure the convergence of the line search if the function  $h(R(t_k \eta_x))$  to be minimized is sufficiently smooth (continuously differentiable with Lipschitz derivative).

**DISCUSSION AND CONVERGENCE** In Alghoritm 3.1 at each iteration the Newton equation (60) is solved for the function  $f$ , then the function  $h(x) = \|\text{grad } f(x)\|^2$  is minimized along the computed direction. In this way we need to compute only Hess  $f$  and grad  $f$ , avoiding the computation of Hess  $h$ , that would require to compute the third derivative of  $f$ .

**Proposition 2.** *Algorithm 3.1 converges to the stationary point  $x^*$  of the function  $f$  with quadratic convergence rate, providing that, in a neighborhood  $\mathcal{I}(x^*)$ ,  $\text{grad } f \neq 0$ ,  $\text{Hess } f$  is injective, and the first iterate is  $x_0 \in \mathcal{I}(x^*)$  [1].*

*Proof.* Let  $x$  denote a generic algorithm iterate, note that by hypothesis the Newton vector  $\eta_x$ , solution of (60), is well defined. The Riemannian gradient of  $h$  reads

$$\text{grad } h = 2\text{Hess } f[\text{grad } f] , \quad (72)$$

evaluating the expression  $Dh(x)[\eta_x]$  we get

$$Dh(x)[\eta_x] = 2 \left\langle \text{grad } f(x), \text{Hess } f(x)[\text{Hess } f(x)^{-1}[-\text{grad } f(x)]] \right\rangle \quad (73)$$

$$= -2 \|\text{grad } f(x)\|^2 \quad (74)$$

$$= -2h(x).$$

The sequence  $\{\eta_{x_k}\}$  is gradient related to  $\{x_k\}$ . In fact by hypothesis and (72) it holds  $\text{grad } h(x_k) \neq 0$ , therefore, using (73) we get  $-2 \sup_{\mathcal{I}(x^*)} h(x_k) = \sup_{\mathcal{I}(x^*)} Dh(x_k)[\eta_{x_k}] < 0$ . By the smoothness of the functional  $\text{Hess } f$  and of the vector field  $\text{grad } f$ , since  $\mathcal{I}(x^*)$  is a compact set, we can conclude that  $\{\eta_{x_k}\}$  is bounded. Hence Algorithm 3.1 fits in the framework of Theorem 4.3.1 and Theorem 6.3.2 [1], stating that every accumulation point of  $\{x_k\}$  is a critical point of  $h$ , so that the local quadratic convergence holds.  $\square$

Note that the *Armijo* condition (71) for the function  $h$  and the direction  $\eta_x$  can be rewritten as

$$h(x) - h(y_k) < -\sigma\gamma_k Dh(x)[\eta_x] = 2\sigma\gamma_k h(x) \quad (75)$$

$$h(y_k) > (1 - 2\sigma\gamma_k) h(x) , \quad (76)$$

where  $y_k = R_x(\gamma_k \eta_x)$ ,  $x = x_k$ ,  $\eta_x = \eta_{x_k}$ , and  $k$  is the iteration number.

### 3.1.5 Application to Square RL Cavity

We will discuss in details the case of an optical cavity made by  $N = 4$  spherical mirrors whose centers approximately lie on a planar square. The practical interest in studying this configuration is to address the design and the control of the GINGER array of RLs [14, 75]. With four mirrors,  $\mathcal{E} = \mathbb{R}^{3 \times 4}$  and  $\mathcal{M} = \mathcal{OB}(2, 4)$ .

The configuration and parameters of the optical cavity are

$$X = (\mathbf{x}_1, \dots, \mathbf{x}_4) \in \mathcal{OB}(2, 4) , \quad (77)$$

$$C = (\mathbf{c}_1, \dots, \mathbf{c}_4) \in \mathbb{R}^{3 \times 4}, \quad (78)$$

and

$$R = \text{diag}(r_1, r_2, r_3, r_4) \in \mathbb{R}^{4 \times 4}; \quad (79)$$

In matrix form, the coordinates of the light spots on the mirror surface are given by

$$Z = XR + C, \quad (80)$$

where the matrix  $Z = (\mathbf{z}_1, \mathbf{z}_2, \mathbf{z}_3, \mathbf{z}_4)$ .

The 4 vectors that describes the sides of the polygonal cavity, i.e., the vectors which join the spots on consecutive mirror surfaces (see Fig.27), are given by  $\mathbf{y}_k = (\mathbf{z}_{k+1} - \mathbf{z}_k)$ ,  $k = \{1, 2, 3, 4\}$  with  $\mathbf{z}_5 := \mathbf{z}_1$ . The length of the optical path, the vector area and compactness ratio are  $p(X; C, R) = \sum_{i=1}^4 \|\mathbf{y}_i\|$ ,  $\mathbf{a}(X; C, R) = \frac{1}{2} \sum_{k=1}^{N-1} \mathbf{z}_k \wedge \mathbf{z}_{k+1}$ , and  $\mathbf{k}_r(X; C, R) = \mathbf{a}(X; C, R) / p(X; C, R)$ , respectively. Defining

$$Y = ZM, \quad M = \begin{pmatrix} 1 & 0 & 0 & -1 \\ -1 & 1 & 0 & 0 \\ 0 & -1 & 1 & 0 \\ 0 & 0 & -1 & 1 \end{pmatrix},$$

the optical path length can be written as

$$p(X; C, R) = \text{tr} \left( d \left( Y^T Y \right)^{1/2} \right), \quad (81)$$

Note that the square root operator  $(\cdot)^{1/2}$  acts component wise on the diagonal entries of the matrix, i.e.  $d(W)^{1/2} = \text{diag}(w_{11}^{1/2}, w_{22}^{1/2}, w_{33}^{1/2}, \dots, w_{nn}^{1/2})$ .

The Euclidean gradient and Hessian of the extension  $\bar{p}$  of the function  $p$  satisfies the following relations

$$\langle \partial \bar{p}, \xi_X \rangle = \text{tr} \left[ d \left( Y^T Y \right)^{-1/2} d \left( Y^T \xi_X R M \right) \right], \quad (82)$$

and

$$\langle \partial^2 \bar{p}[\eta], \xi_X \rangle = \text{tr} \left[ d \left( Y^T Y \right)^{-1/2} d \left( M^T R \xi_X^T \eta_X R M \right) \right] - \quad (83)$$

$$\text{tr} \left[ d \left( Y^T Y \right)^{-3/2} d \left( Y^T \eta_X R M \right) d \left( Y^T \xi_X R M \right) \right]. \quad (84)$$

Let us consider a square optical cavity of side  $L$ , and four mirrors with the same curvature radius, i.e.

$$C^* = \left(r - \frac{L}{\sqrt{2}}\right) \begin{pmatrix} 1 & 0 & -1 & 0 \\ 0 & 1 & 0 & -1 \\ 0 & 0 & 0 & 0 \end{pmatrix}, \quad (85)$$

$$R^* = \text{diag}(r, r, r, r),$$

so that  $p(X^*; C^*, R^*) = 4L$ . The point  $X^* = -(r - L/\sqrt{2})^{-1}C^*$  lays in  $\mathcal{OB}(2,4)$ , and one can check that  $X^*$  is an extremum of  $p$  using (82) and (83), and the formulas of Table 5. The eigenvalues of Hess  $p$  at the point  $X^*$  reads

$$\Sigma(\text{Hess } p(X^*)) = -\sqrt{2}r \cdot \left[ (1, 1, 1, 1, 1, 1, 1, 1) - \quad (86)$$

$$\left(0, 0, \frac{L}{\sqrt{2}r}, \frac{L}{\sqrt{2}r}, \frac{\sqrt{2}L}{r}, \frac{\sqrt{2}L}{r}, \frac{\sqrt{2}L}{r}, \frac{4L}{\sqrt{2}r}\right) \right]. \quad (87)$$

The eigenvalues of Hess  $p$  are non-zero provided that the ration  $L/r$  is not equal to  $\sqrt{2}$ ,  $1/\sqrt{2}$ , or  $\sqrt{2}/4$  which corresponds to unstable optical cavity configurations[]. For a stable optical cavity the Riemannian Hessian has non-zero eigenvalues, therefore  $X^*$  is an isolated root of grad  $p$ . For a stable cavity, furthermore the point  $X^*$  is neither a minimum nor a maximum, but a saddle point of  $p$ , as the spectrum of the Hessian (86) has both strictly positive and negative eigenvalues. If a stable optical cavity is slightly misaligned from  $C^*$ , by the continuity of  $p$ , the Riemannian gradient will have isolated roots, and so the eigenvalues of the Riemannian Hessian will be different from zero and the Newton algorithm will converge to the path which satisfies the *Fermat's* principle.

### 3.1.6 Numerical Study

The proposed geometric Newton algorithm has been tested by Monte Carlo techniques. Optical cavity configurations are generated starting with mirror positions close to square configuration  $C^*$ , with  $L= 1.6$  m and represented by  $3 \times 4$  random matrices whose entries are uniformly distributed over the set  $\left\{ |C_{ij} - C_{ij}^*| < \sigma \right\}$ , with  $\sigma$  ranging from  $10^{-6}L$  to  $10^{-2}L$  with a logarithmic spaced step of  $L/10$ . The radii matrix used is  $R = rI_{4 \times 4}$ , with  $r = 4$  m. Those values correspond to the design of the *RLG GP2* [75]. The geometric Newton algorithm has been applied to find the saddle point of the function  $p$ , starting from the trial configuration  $X^*$ . This procedure has been repeated  $10^4$  times to assess if mirror displacements are small enough for satisfying the convergence properties of the algorithm.

We can now state the first result: all the runs do not show ill-conditioning problems in the Newton vector computation. In addi-



tion, the algorithm took at most 3 iterations to generate an iterate such that  $\|\text{grad } p(x)\| < 10^{-12}$  m, and quadratic convergence is also attained, as expected for a problem satisfying second order sufficient condition for optimality (i.e., positive definiteness of the Hessian at the optimal point). In all the Monte Carlo run we checked the eigenvalues of the Riemannian Hessian, all the laser spots positions found by our algorithm were saddle points of  $p$ , i.e. the Hessian eigenvalues are positive and negative.

To better illustrate the algorithm execution, we show in Figure 25 the typical behavior of  $\|\text{grad } p(x)\|$  in a run with enhanced mirror displacements from the ideal square configuration. In this case it was  $\sigma \sim 0.5$  m and the algorithm took 5 iterations to converge.

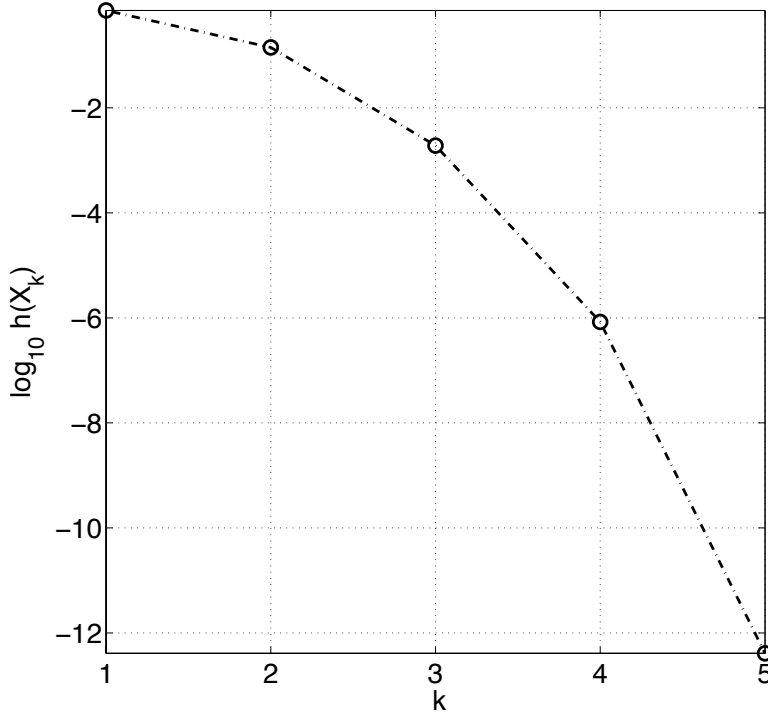
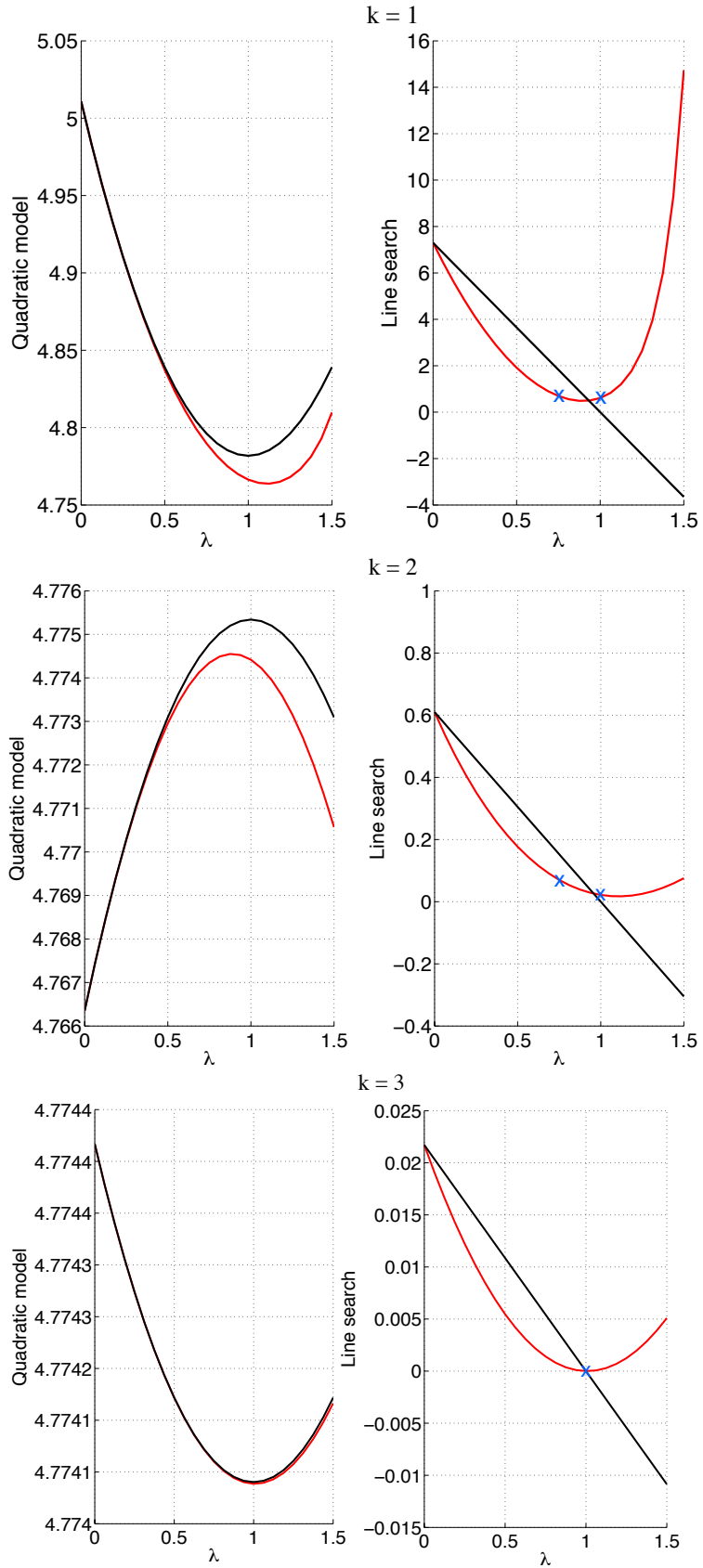


Figure 25: Plot of  $h(x_k) = \|\nabla p(x_k)\|$  versus the iteration index  $k$ .

In Figure 26 a comparison between the function  $p$  and the second order geometric model for  $p$ , and another comparison between the function  $h$  and Armijo condition for the function  $h$  are displayed. In the figure  $m_f(\lambda) = f(x_k) + \langle \text{grad } f(x_k), \lambda \eta_x \rangle + 1/2 \langle \text{Hess } f(x_k)[\lambda \eta_x], \lambda \eta_x \rangle$ ,  $m_h(\lambda) = h(x) + \sigma \langle \text{grad } h(x_k), \lambda \eta_x \rangle$ ,  $\lambda \in [0, 1]$ ,  $\sigma = 1/2$  and  $\eta_x = \eta_{x_k}$  is the Newton vector at the iteration  $k$ . Each of the 5 iterations of the run reported in Figure 25 is displayed. We note that the optical path length  $p$  is well modeled by the second order geometric model starting from the first iteration, and that condition (71) allows for step sizes  $t_k$  closer to the unity, like in pure Newton methods, as the iteration number increase.



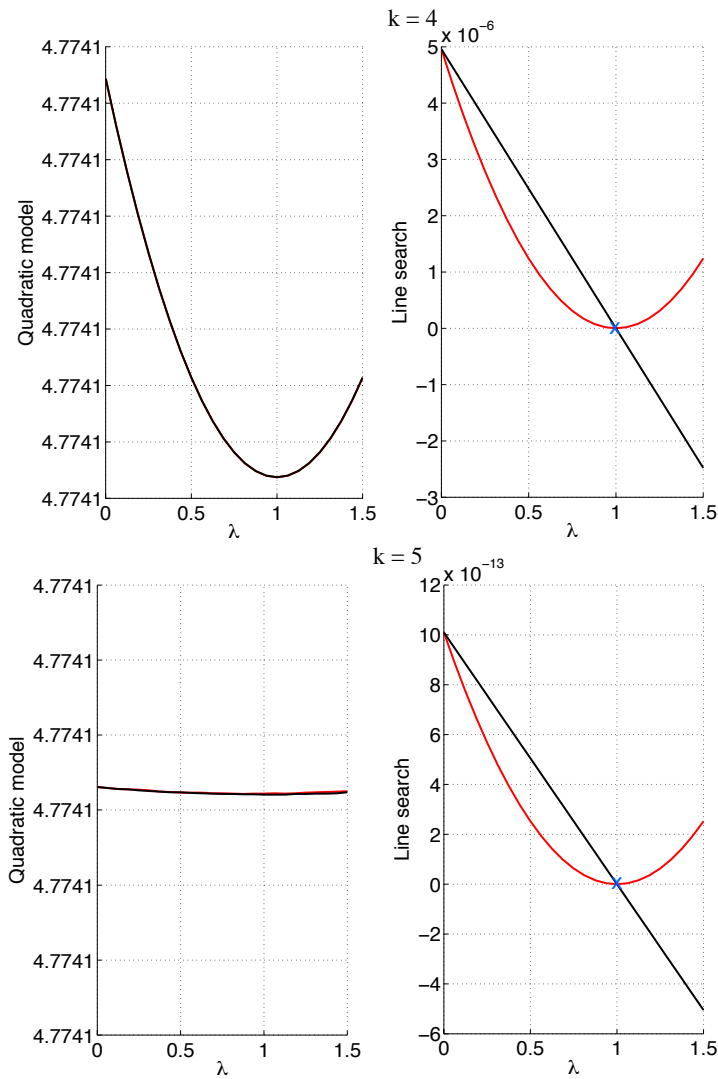


Figure 26: Comparison between the functions  $p$  and its second order geometric model, and between the function  $h$  and the *Armijo* condition, on consecutive algorithm iterations from 1 to 5. The black lines represent the second order geometric model for  $p$  and the *Armijo* condition, and the red lines represent the functions  $p$  and  $h$ , respectively. The blue crosses displayed are the iterates of the line search method.

In Figure 27 we draw an illustrative example of mirror displacements and the corresponding laser beams as calculated by *Fermat's* principle.

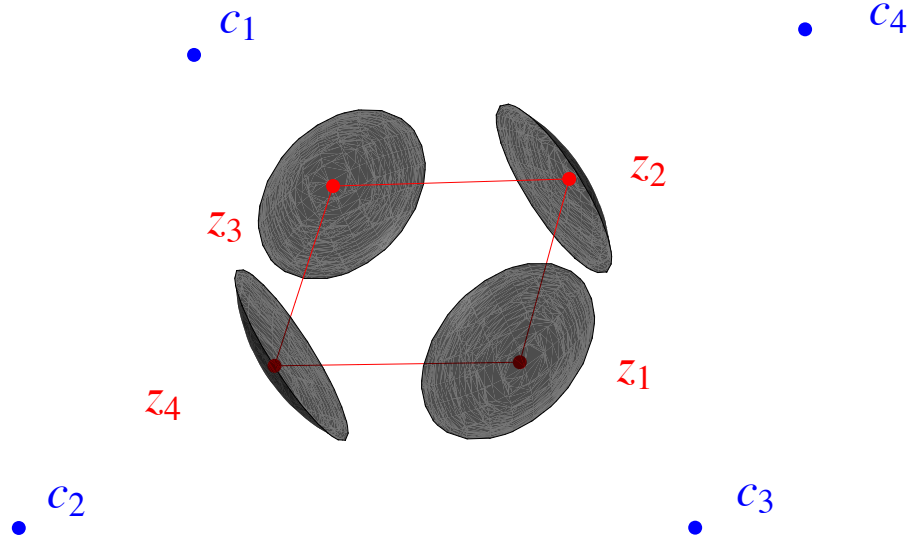


Figure 27: An example of displacements of mirrors forming a square optical cavity. Elements relative to each mirror are colored in grey. Red dots mark the mirror centers, the thick orange lines represent the optical path length as a link between consecutive laser spots  $z_k$ .

### 3.2 POSE AND SHAPE OF FOUR POINTS IN $\mathbb{R}^3$

In what follows we manipulate sets of four tridimensional points, i.e. the centers of curvature of the  $RL$  mirrors, by means of their coordinate matrix  $M \in \mathbb{R}^{3 \times 4}$ . Note that in the matrix  $M$  the components of a vector representing a single point are disposed in a column. We denote the columns of the matrix  $M \in \mathbb{R}^{3 \times 4}$  as  $M_i \in \mathbb{R}^3$ , where  $i = 1, 2, 3, 4$ .

Our aim is to address the distinction between the information related to the pose of the 4 points, and the information concerning their shape, in the matrix  $M$ . Figure 28 displays the two different situations. Consider the action of  $SE(3)$  on  $\mathbb{R}^{3 \times 4}$ , in the form of  $N = RM + \mathbf{x}\mathbb{1}_4^T$ , where  $SE(3)$  is the Special Euclidean group of dimension 3, whose elements are here represented by a pair  $(R, \mathbf{x})$  of rotation matrix  $R \in SO(3)$  and a vector  $\mathbf{x} \in \mathbb{R}^3$ . The vector  $\mathbb{1}_4 = [1 \ 1 \ 1 \ 1]^T$  is employed for the compactness of the formulas. Clearly only the pose of the 4 points has changed in the representation given by  $N$  from the one given by  $M$ . In fact one can easily check that all the distances  $d_{ij}^M = \|M_i - M_j\|$  between points represented by  $M_i, M_j$  are equal to the distances  $d_{ij}^N = \|N_i - N_j\|$  between points represented by  $N_i, N_j, i, j \in \{1, 2, 3, 4\}$ . In contrast with the latter situation consider the case  $N = 2M$ , the points of  $N$  may have the same pose of the ones of  $M$ , but certainly the shape of the points has changed. Indeed the points represented by  $N$  are simply the points represented by  $M$  zoomed by a factor of 2

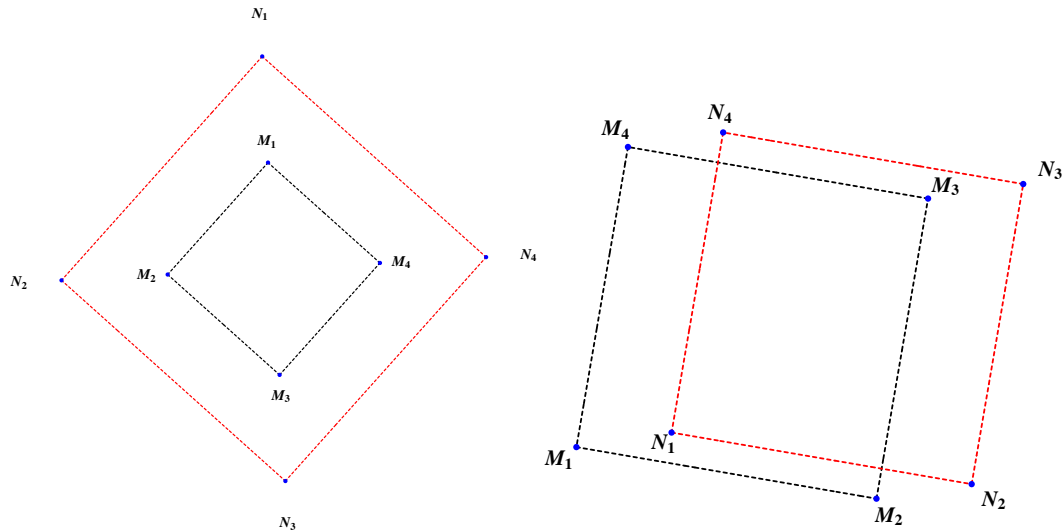


Figure 28: In the top picture the red figure is obtained from the black one by a dilatation of the points, while in the bottom picture only the pose of the points has been changed.

So far our aim has been declared to describe the information about the shape of the figure represented by means of the points which are the columns of  $M \in \mathbb{R}^{3 \times 4}$ , independently from the rigid displacement of the 4 points, thus working with sets we would like to complete  $SE(3)$  to  $\mathbb{R}^{3 \times 4}$ . To this purpose we need to restrict the configuration space  $\mathbb{R}^{3 \times 4}$  to one in which the matrices allow for a decomposition where a rotation matrix and a 3 component real vector can be unambiguously factorized. Since we have 4 vectors available and we only require 3 orthonormal components to specify a basis of  $\mathbb{R}^3$ , there will exist more than one way to accomplish our objective. An affordable way is to consider the Gram–Schmidt procedure starting from a suitable column of  $M$ , and then consider others columns of  $M$  during the next algorithm iterations. Note that, once we find two independent components, we can easily get the third one by means of the wedge product of  $\mathbb{R}^3$  of the first two. The key problem here arises if the columns of  $M$  are linearly dependent. It is worth noticing that a collection of vectors in  $\mathbb{R}^3$  can be linearly dependent or not in correspondence to the choice of the origin of their reference frame. E.g. one can represent any couple of points in  $\mathbb{R}^3$  with vectors that are linearly dependent, by choosing a suitable position for the axes origin.

It seems useful for our purposes to fix the axes origin so that the linear independence between couples of vectors representing consecutive points is preserved. We fix the axes origin in the point given by the arithmetic mean of the columns of  $M$ ,  $\bar{M} = \sum_{i=1}^4 M_i / 4$ , and then assume linear independence among couples of vectors which represent consecutive points  $M_i - \bar{M}, M_{i+1} - \bar{M}$ . From now on by convention the index  $i$  is assumed to be a circular index on the set  $\{1, \dots, 4\}$

so that e.g. if  $i = 4$  then  $i + 1 = 1$ . We then choose a coordinate chart of  $\mathcal{P}$ , the resulting linear subspace of  $\mathbb{R}^{3 \times 4}$  (4 real triplets with null mean) with the additional non linear constraints. Our choice is suited to account for asymmetry with respect to a symmetric square configuration of the points. Since the hypothesis of linear independence (among the vector representing consecutive points in  $\mathcal{P}$ ) holds for the square configuration, and we are interested in describing optical cavities only slightly misaligned from a square configuration, the assumptions made seems general enough to address all the misaligned optical cavities of interest.

### 3.2.1 Pose and Shape Decomposition

To introduce Theorem in a compact way we will require the following definitions and Lemma.

**Definition 3.**

$$\mathcal{P} = \left\{ M \in \mathbb{R}^{3 \times 4} \mid M_i \wedge M_{i+1} \neq 0, \bar{M} = 0_{3 \times 1} \right\}, \quad (88)$$

where  $\wedge$  is the wedge product in  $\mathbb{R}^3$ . The set  $\mathcal{P}$ , here called *Pre-Shape Space* in analogy with [41, 42], contains matrices whose columns have null mean that allow for the Shape and Pose decomposition.

**Definition 4.**

$$\mathcal{T} = \left\{ \begin{bmatrix} a_1 & b & 0 \\ 0 & a_2 & 0 \\ 0 & 0 & 1 \end{bmatrix} \in \mathbb{R}^{3 \times 3}, a_1, a_2 \in \mathbb{R}^+, b \in \mathbb{R} \right\}, \quad (89)$$

the elements of this set will be shown to parametrize the isosceles trapezoids, a subset of all the possible matrices in  $\mathcal{P}$ .

**Definition 5.**

$$\mathcal{V} = \mathbb{R}^3 \setminus \left\{ \mathbf{e}_1 + \alpha \mathbf{e}_2, -\mathbf{e}_2 + \beta \mathbf{e}_1, \frac{\mathbf{e}_1 - \mathbf{e}_2}{2} + \gamma (\mathbf{e}_1 + \mathbf{e}_2), \alpha, \beta, \gamma \in \mathbb{R} \right\}, \quad (90)$$

where  $\mathbf{e}_1 = [1 \ 0 \ 0]^T$ , and  $\mathbf{e}_2 = [0 \ 1 \ 0]^T$ . The set  $\mathcal{V}$  is the tridimensional space with three lines lying in the plane orthogonal to the third canonical unit vector excerpcted. The elements of the set  $\mathcal{V}$  will parametrize matrices that may represent irregular quadrilaterals, e.g. when the points  $M_i$  are not coplanar.

**Lemma 6.** Given  $\mathbf{a}$  and  $\mathbf{b} \in \mathbb{R}^3$  such that  $\mathbf{a} \wedge \mathbf{b} \neq 0$ , there exists a unique  $R \in SO(3)$  such that  $[\mathbf{a}, \mathbf{b}] = RC$ , with

$$R = \left[ \mathbf{u}, \frac{\mathbf{v} - \langle \mathbf{u}, \mathbf{v} \rangle \mathbf{u}}{\sqrt{1 - \langle \mathbf{u}, \mathbf{v} \rangle^2}}, \frac{\mathbf{u} \wedge \mathbf{v}}{\|\mathbf{u} \wedge \mathbf{v}\|} \right], \quad (91)$$

and

$$C = \begin{bmatrix} \|\mathbf{a}\| & \|\mathbf{b}\| \langle \mathbf{u}, \mathbf{v} \rangle \\ 0 & \|\mathbf{b}\| \sqrt{1 - \langle \mathbf{u}, \mathbf{v} \rangle^2} \\ 0 & 0 \end{bmatrix}, \quad (92)$$

where  $\mathbf{u} = \frac{\mathbf{a}}{\|\mathbf{a}\|}$  and  $\mathbf{v} = \frac{\mathbf{b}}{\|\mathbf{b}\|}$ . Note also that  $c_{11}$  and  $c_{22}$  are always positive.

The proof of Lemma 6 is given in the Appendix.

**Theorem 7.** Let  $Q \in \mathbb{R}^{3 \times 4}$ , be such that

$$Q \left( I_4 - \frac{\mathbf{1}_4 \mathbf{1}_4^T}{4} \right) = P \in \mathcal{P}. \quad (93)$$

Then,  $Q$  admits the pose and shape decomposition

$$Q = RT \left( \begin{bmatrix} I_2 & -I_2 \\ 0_{1 \times 2} & 0_{1 \times 2} \end{bmatrix} + \begin{bmatrix} 0_{3 \times 1} & 0_{3 \times 1} & \mathbf{v} & -\mathbf{v} \end{bmatrix} \right) + \bar{Q} \mathbf{1}_n^T \quad (94)$$

where  $\bar{Q} \in \mathbb{R}^3$ ,  $R \in SO(3)$ ,  $T \in \mathcal{T}$ , and  $\mathbf{v} \in \mathcal{V}$ . The expressions for  $R$  and  $T$  are given by Lemma 6 in terms of  $P_1$  and  $P_2$ , and  $\mathbf{v} = T^{-1}R^{-1}(Q_3 - Q_1)$  or, equivalently,  $\mathbf{v} = T^{-1}R^{-1}(Q_2 - Q_4)$ .

*Proof.* By definition, the matrix  $P$  defined by (93) is such that  $\bar{P} = 0_{3 \times 1}$ .

The linear constraint  $\bar{P} = 0_{3 \times 1}$  implicitly defines a linear subspace of  $\mathbb{R}^{3 \times 4}$ . Defining

$$\begin{cases} \mathbf{w}_1 := P_1 \\ \mathbf{w}_2 := P_2 \\ \mathbf{w}_3 := P_3 + P_1 = -(P_4 + P_2) \end{cases}, \quad (95)$$

we can rewrite  $P$  as

$$P = \begin{bmatrix} \mathbf{w}_1 & \mathbf{w}_2 & \mathbf{w}_3 - \mathbf{w}_1 & -\mathbf{w}_2 - \mathbf{w}_3 \end{bmatrix}. \quad (96)$$

Consider  $\mathbf{w}_1$  and  $\mathbf{w}_2$  as in (96), i.e., the first two columns on  $P$ . Because, by hypothesis,  $P \in \mathcal{P}$ , it follows that  $\mathbf{w}_1 \wedge \mathbf{w}_2 \neq 0$ , and, from Lemma 6, it follows that there exist unique  $R \in SO(3)$ ,  $a_1, a_2 > 0$ , and  $b \in \mathbb{R}$  such that

$$\begin{bmatrix} \mathbf{w}_1 & \mathbf{w}_2 \end{bmatrix} = R \begin{bmatrix} a_1 & b \\ 0 & a_2 \\ 0 & 0 \end{bmatrix}. \quad (97)$$

The last matrix in the right hand side of (97) can be then rewritten as

$$\begin{bmatrix} a_1 & b \\ 0 & a_2 \\ 0 & 0 \end{bmatrix} = \begin{bmatrix} a_1 & b & 0 \\ 0 & a_2 & 0 \\ 0 & 0 & 1 \end{bmatrix} \begin{bmatrix} I_2 \\ 0 \ 0 \end{bmatrix} := T \begin{bmatrix} I_2 \\ 0 \ 0 \end{bmatrix}. \quad (98)$$

As  $a_1$  and  $a_2$  are positive, it follows that  $T \in \mathcal{T}$ .

From (93) and (96), we get

$$Q = \begin{bmatrix} \mathbf{w}_1 & \mathbf{w}_2 & \mathbf{w}_3 - \mathbf{w}_1 & -\mathbf{w}_2 - \mathbf{w}_3 \end{bmatrix} + \bar{Q} \mathbf{1}_4^T, \quad (99)$$

From (99), by using (97) and (98) and defining  $\mathbf{v} = T^{-1}R^{-1}\mathbf{w}_3$ , we finally get (94).

The remaining part of this proof shows that  $\mathbf{v} \in \mathcal{V}$ .

Recalling that we have proposed the parametrization

$$\begin{cases} P_1 = \mathbf{w}_1 & = RT\mathbf{e}_1 \\ P_2 = \mathbf{w}_2 & = RT\mathbf{e}_2 \\ P_3 = \mathbf{w}_3 - \mathbf{w}_1 & = RT(\mathbf{v} - \mathbf{e}_1) \\ P_4 = -\mathbf{w}_3 - \mathbf{w}_2 & = RT(-\mathbf{v} - \mathbf{e}_2) \end{cases}, \quad (100)$$

for the element  $P \in \mathcal{P}$ . The domain of  $R$ ,  $T$ , and  $\mathbf{v}$  have to match the non linear constraints  $P_i \wedge P_{i+1} \neq 0_{3 \times 1}$ , that we can enumerate as

$$\begin{cases} P_1 \wedge P_2 & \neq 0_{3 \times 1} \\ P_2 \wedge P_3 & \neq 0_{3 \times 1} \\ P_3 \wedge P_4 & \neq 0_{3 \times 1} \\ P_4 \wedge P_1 & \neq 0_{3 \times 1} \end{cases}. \quad (101)$$

The domain of  $R$  and  $T$  have already been fixed by the first inequality in (101), explicating the remaining conditions in the following way

$$(R\mathbf{A}\mathbf{x}) \wedge (R\mathbf{T}\mathbf{y}) \neq 0_{0_{3 \times 1}} \Leftrightarrow R\mathbf{T}\mathbf{x} \neq \lambda R\mathbf{T}\mathbf{y}, \lambda \in \mathbb{R} \Leftrightarrow \quad (102)$$

$$\mathbf{x} \neq \lambda \mathbf{y}, \lambda \in \mathbb{R} \Leftrightarrow \mathbf{x} \wedge \mathbf{y} \neq 0_{3 \times 1}, \mathbf{x}, \mathbf{y} \in \mathbb{R}^3 \quad (103)$$

we get:



$$\begin{cases} \mathbf{v} - \mathbf{e}_1 & \neq \alpha \mathbf{e}_2 \\ (\mathbf{v} - \mathbf{e}_1) \wedge (\mathbf{v} + \mathbf{e}_2) & \neq 0_{3 \times 1} \quad \alpha, \beta \in \mathbb{R}. \\ \mathbf{v} + \mathbf{e}_2 & \neq \beta \mathbf{e}_1 \end{cases} \quad (104)$$

The second inequality of (104) can be rewritten as

$$\left( \mathbf{v} - \frac{\mathbf{e}_1 + \mathbf{e}_2}{2} - \frac{\mathbf{e}_1 - \mathbf{e}_2}{2} \right) \wedge \left( \mathbf{v} + \frac{\mathbf{e}_1 + \mathbf{e}_2}{2} - \frac{\mathbf{e}_1 - \mathbf{e}_2}{2} \right) \neq \mathbf{0} \Leftrightarrow \quad (105)$$

$$\begin{aligned} & \left( \mathbf{v} - \frac{\mathbf{e}_1 - \mathbf{e}_2}{2} \right) \wedge \left( \mathbf{v} - \frac{\mathbf{e}_1 - \mathbf{e}_2}{2} \right) + \dots \quad (106) \\ +2 \left( \mathbf{v} - \frac{\mathbf{e}_1 - \mathbf{e}_2}{2} \right) \wedge \left( \frac{\mathbf{e}_1 + \mathbf{e}_2}{2} \right) - \left( \frac{\mathbf{e}_1 + \mathbf{e}_2}{2} \right) \wedge \left( \frac{\mathbf{e}_1 + \mathbf{e}_2}{2} \right) \neq \mathbf{0} \Leftrightarrow \quad (107) \end{aligned}$$

$$2 \left( \mathbf{v} - \frac{\mathbf{e}_1 - \mathbf{e}_2}{2} \right) \wedge \left( \frac{\mathbf{e}_1 + \mathbf{e}_2}{2} \right) \neq \mathbf{0} \Leftrightarrow \quad (108)$$

$$\mathbf{v} \neq \frac{\mathbf{e}_1 - \mathbf{e}_2}{2} + \gamma (\mathbf{e}_1 + \mathbf{e}_2), \gamma \in \mathbb{R}. \quad (109)$$

Therefore the domain of  $\mathbf{v}$  is given by (90).  $\square$

*Remark 8.* Considering the rotation matrix  $R$  as an element of  $SO(3)$ , we can write the decomposition given in Theorem 7 in a compact form, as  $\mathcal{P} = SO(3) \times \mathcal{T} \times \mathcal{V}$ . This allows for a clean use of the quotient set operation to account for shape changes apart from pose changes. Therefore the shape of four points in  $\mathbb{R}^3$  is parametrized as an element of the set  $\mathcal{T} \times \mathcal{V}$ , and its coordinate representation is given by (94)

*Remark 9.* The parametrization given in (95) has the following interpretation: the vectors  $\mathbf{w}_1$  and  $\mathbf{w}_2$  are the two principal symmetry axes of the quadrilateral represented by the points  $P_1, P_2, P_3, P_4$ . the symmetry  $1 \rightarrow 3, 2 \rightarrow 4$ , is broken by the vector  $\mathbf{w}_3$ . In fact one can see that if  $\mathbf{w}_3 = 0_{3 \times 1}$ , the quadrilateral is regular (planar), and  $\mathbf{v} = 0_{3 \times 1}$ . Figure 29 shows the parametrization given in (95).

*Remark 10.* Note that the domain of  $\mathbf{v}$  is not simply connected, i.e. regions where  $\|\mathbf{v}\| > 1$  may not be connected with regions where  $\|\mathbf{v}\| < 1$ . However in the work interest is put in situations where  $\|\mathbf{v}\| \ll 1$ , so we can assume  $\mathbf{v}$  to be in the simply connected part of  $\mathcal{V}$  containing the origin. Figure 30 shows the plot of the lines form  $\mathbb{R}^3$  which represents the excepted part of  $\mathbb{R}^3$  in the set  $\mathcal{V}$ .

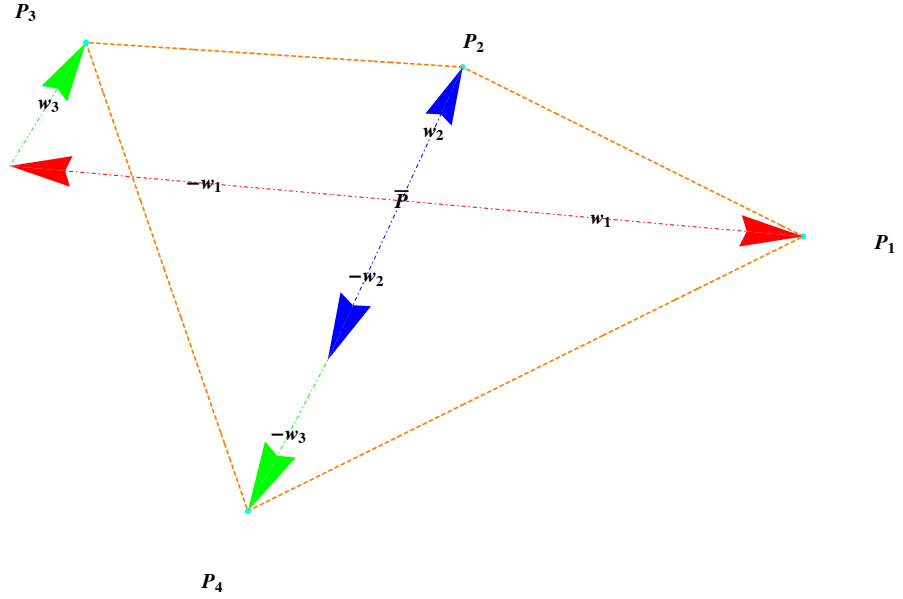


Figure 29: Visual scheme of the proposed set of coordinate for  $P$ .

*Remark 11.* By the unicity of the representation of elements in the vector subspace given by  $\bar{P} = 0_{3 \times 1}$ , and by the unicity of the decomposition given in Lemma 6, the Shape and Pose decomposition given by Theorem 7 is unique. It means that given a matrix  $M$  fulfilling the hypotheses of the Theorem it exists one and only one element  $(A, R, \mathbf{v}, \bar{M})$  for which the thesis of the Theorem 7 holds.

*Remark 12.* We stress that the parameters  $(T, R, \mathbf{v}, \bar{M})$  are given in Lemma 6 and Theorem 7 as smooth functions of the matrix  $M$ . This means that we can consider any generic curve  $t \mapsto M(t) \in \mathbb{R}^{3 \times 4}$ , and if for every fixed  $t$  the matrix  $M(t)$  satisfies the hypothesis of the Shape and Pose decomposition, then we can point-wise describe the curves  $t \mapsto R(t)$ ,  $t \mapsto T(t)$ ,  $t \mapsto \mathbf{v}(t)$  and finally  $t \mapsto \bar{M}(t)$ , which are in their turn smooth.

*Remark 13.* Let now briefly discuss the properties of our decomposition in relation to the cyclical order of the points in  $P$ . Starting from the matrix  $P$  we can consider a cyclic permutation of its columns by right multiplication by

$$S = \begin{bmatrix} 0 & 0 & 0 & 1 \\ 1 & 0 & 0 & 0 \\ 0 & 1 & 0 & 0 \\ 0 & 0 & 1 & 0 \end{bmatrix}. \quad (110)$$

We can now state the following Corollary:

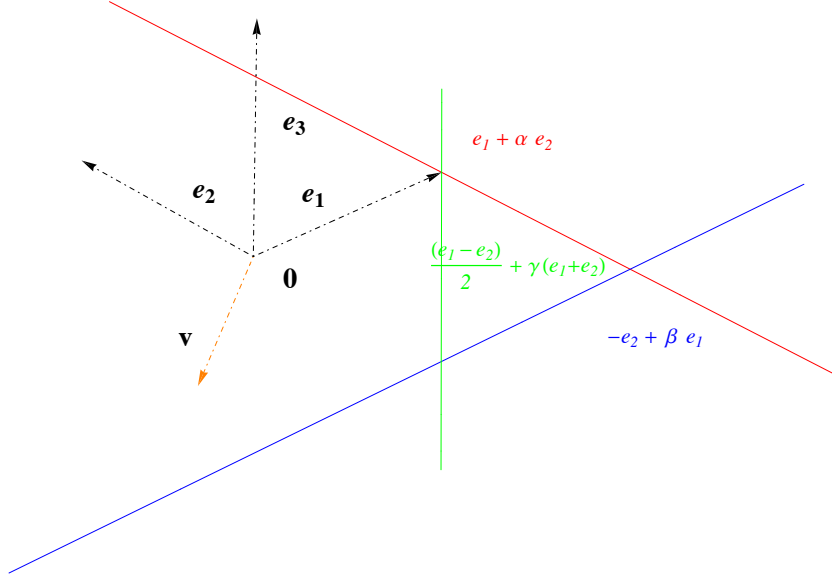


Figure 30: Picture of the domain of  $\mathbf{v}$ . The colored lines are the excerpted lines due to the nonlinear constraints  $P_i \wedge P_{i+1} \neq 0$ .

**Corollary 14.** *Within the same hypotheses of Theorem 7,  $M$  admits the 4 decompositions*

$$M = R^{(i)} T^{(i)} \left( \begin{bmatrix} I_2 & -I_2 \\ 0 & 0 \end{bmatrix} + \begin{bmatrix} 0 & 0 \\ 0 & 0 \\ 0 & 0 \\ \mathbf{v}^{(i)} & -\mathbf{v}^{(i)} \end{bmatrix} \right) S^{-i} + \bar{M} \mathbf{1}_n^T. \quad (111)$$

*Proof.* Firstly note that the mean  $\bar{M}$  is invariant for a cyclic permutation of the columns of  $M$ , i.e.  $MS^i \mathbf{1}/4 = \bar{M}$ ,  $i = 1, \dots, 4$ .

Consider the matrices  $M^{(i)} = MS^i$ , we check the hypothesis of our decomposition for those matrices with the help of

$$P^{(i)} = M^{(i)} \left( I_4 - \frac{\mathbf{1}_4 \mathbf{1}_4^T}{4} \right), \quad (112)$$

since in the last expression all the square  $4 \times 4$  matrices commutes with each other we can rewrite each  $P^{(i)}$  as

$$P^{(i)} = M \left( I_4 - \frac{\mathbf{1}_4 \mathbf{1}_4^T}{4} \right) S^i = PS^i. \quad (113)$$

Now if  $P \in \mathcal{P}$  it also holds  $P^{(i)} \in \mathcal{P}$ ,  $i = 1, 2, 3, 4$ . The proof of the Corollary follows applying Theorem 7 to the matrices  $P^{(i)}$ , obtaining thus the matrices  $R^{(i)} \in SO(3)$ ,  $T^{(i)} \in \mathcal{T}$ , and the vectors  $\mathbf{v}^{(i)}$ , then rewriting  $P = P^{(i)} S^{-i}$  using the decompositions and the inverses of

the matrices  $S^i$ . Note that for  $i = 4$  we recover Theorem 7 since it holds  $S^4 = I_4$ .  $\square$

*Remark 15.* Consider a generic  $P^{(i)}$  defined as in (93). Expressing its columns as in (96), the third component is given by  $(-1)^i \mathbf{w}_3$ , with  $\mathbf{w}_3 = P_3 + P_1 = -(P_4 + P_2)$ . We stress that this holds for any value of  $i \leq 4$  with the same vector  $\mathbf{w}_3$ . The latter vector direction and modulus are invariant by the product by  $S^i$ , therefore the quantity  $\mathbf{w}_3 = R^{(i)} T^{(i)} \mathbf{v}^{(i)}$  is conserved through all the possible decompositions of Corollary 14, up to a sign.

To describe shape variations with respect to an ideal square configuration, in which all the mirrors radii are equal to  $r$  and the optical path length is  $4L$ , it is useful to cast the square configuration as

$$T_0 = \begin{bmatrix} d/2 & 0 & 0 \\ 0 & d/2 & 0 \\ 0 & 0 & 1 \end{bmatrix}, \quad \mathbf{v}_0 = 0_{3 \times 1}, \quad (114)$$

where  $d = r - L/\sqrt{2}$  is the diagonal length of the square formed by the mirror centers.

### 3.2.2 From Shape to Distance Matrix

Now let  $R = I_3$  and  $\bar{P} = 0_{3 \times 1}$ , we can express all the distances between couples of points of  $P$  as a function of  $T$ , parametrized as in (89), and of  $\mathbf{v} = (v_1, v_2, v_3)^T$ . We get

$$\begin{cases} l_1 = \sqrt{(a_2 - a_1)^2 + a_3^2} \\ l_2 = \sqrt{[a_1(1 - v_1) + a_2(1 - v_2)]^2 + a_3^2(1 - v_2)^2 + v_3^2} \\ l_3 = \sqrt{[a_1(1 - 2v_1) - a_2(1 + 2v_2)]^2 + a_3^2(1 + v_2)^2 + 4v_3^2} \\ l_4 = \sqrt{[a_1(1 + v_1) + a_2(1 + v_2)]^2 + a_3^2(1 + v_2)^2 + v_3^2} \\ d_1 = \sqrt{[a_1(2 - v_1) - a_2v_2]^2 + a_3^2v_2^2 + v_3^2} \\ d_2 = \sqrt{[a_1v_1 + a_2(2 + v_2)]^2 + a_3^2(2 + v_2)^2 + v_3^2} \end{cases}. \quad (115)$$

Note that the quadratic equation system

$$\begin{cases} l_1^2 = (a_2 - a_1)^2 + a_3^2 \\ l_2^2 = [a_1(1 - v_1) + a_2(1 - v_2)]^2 + a_3^2(1 - v_2)^2 + v_3^2 \\ l_3^2 = [a_1(1 - 2v_1) - a_2(1 + 2v_2)]^2 + a_3^2(1 + v_2)^2 + 4v_3^2 \\ l_4^2 = [a_1(1 + v_1) + a_2(1 + v_2)]^2 + a_3^2(1 + v_2)^2 + v_3^2 \\ d_1^2 = [a_1(2 - v_1) - a_2v_2]^2 + a_3^2v_2^2 + v_3^2 \\ d_2^2 = [a_1v_1 + a_2(2 + v_2)]^2 + a_3^2(2 + v_2)^2 + v_3^2 \end{cases} \quad (116)$$

has solution in  $\mathbf{y}$ . We found 2 distinct solutions,

$$\begin{cases} a_1 = \frac{\sqrt{3d_1^2 - d_2^2 + 3l_1^2 - l_2^2 - l_3^2 + 3l_4^2}}{4} \\ a_2 = \frac{d_1^2 + d_2^2 - 5l_1^2 + l_2^2 - l_3^2 + l_4^2}{16a_1} \\ a_3 = \frac{\sqrt{4l_1^2(d_1^2 + d_2^2 + l_2^2 - l_3^2 + l_4^2 - l_1^2) - (d_1^2 - d_2^2 - l_2^2 + l_4^2)^2}}{8a_1} \\ v_1 = \frac{(d_1^2 - l_2^2)^2 - (d_2^2 - l_4^2)^2 + 2l_1^2(-d_1^2 + d_2^2 - l_2^2 + l_4^2)}{64a_1a_3} \\ v_2 = \frac{-(d_1^2 + d_2^2 - 2l_1^2)(d_1^2 + d_2^2 - l_1^2) + (d_1^2 - d_2^2 + l_1^2 - l_3^2)l_2^2 + (d_1^2 + d_2^2 - 2l_1^2 - l_4^2)l_3^2 + (-d_1^2 + d_2^2 + l_1^2 + 4l_2^2)l_4^2}{-32a_1a_3} \\ v_3 = \pm \frac{\sqrt{d_2^2[d_1^4 - (l_1^2 - l_2^2)(l_3^2 - l_4^2)] + (l_1^2l_3^2 - l_2^2l_4^2)(l_1^2 - l_2^2 + l_3^2 - l_4^2) + d_1^2[d_2^4 + (l_2^2 - l_3^2)(l_1^2 - l_4^2)] - d_1^2d_2^2(l_1^2 + l_2^2 + l_3^2 + l_4^2)}}{8a_1a_3} \end{cases} \quad (117)$$

that are different in the sign of the component  $v_3$ .

### 3.2.3 Simulation results

We compare the results of two simulations of  $10^4$  RL cavities slightly misaligned from the square configuration  $C^*$ , with  $L = 1.6$  m,  $R = 4$  m. The mirror centers matrices of the optical cavities are represented with the help of Theorem 7. In the first simulation all the scalar parameters of  $T$  and  $v$  were uniformly distributed in the relative range  $[-10^{-6}, 10^{-6}]$ , around their nominal value (114). In Fig. 31 the histograms of the perimeter  $p$  and the scalar compactness factor  $k_S = \|\mathbf{a}\| / p$  are displayed.

The second simulation is similar to the first, but with constrained shape parameter  $T$ , i.e. the first two diagonal elements of  $T$  does not vary from their nominal values. The remaining 4 elements were uniformly distributed as in the first simulation. In Fig. 32 the histograms of the perimeter  $p$ , and the scalar compactness factor  $k_S$  are displayed.

Finally, we run  $10^3$  simulations with the shape parameters uniformly distributed in the relative range  $[-\sigma, \sigma]$ , with  $10^{-10} < \sigma < 10^{-2}$ . We simulated 4 cases: an unconstrained ring, a ring with constrained diagonal elements of  $T$ , and two intermediate cases in which

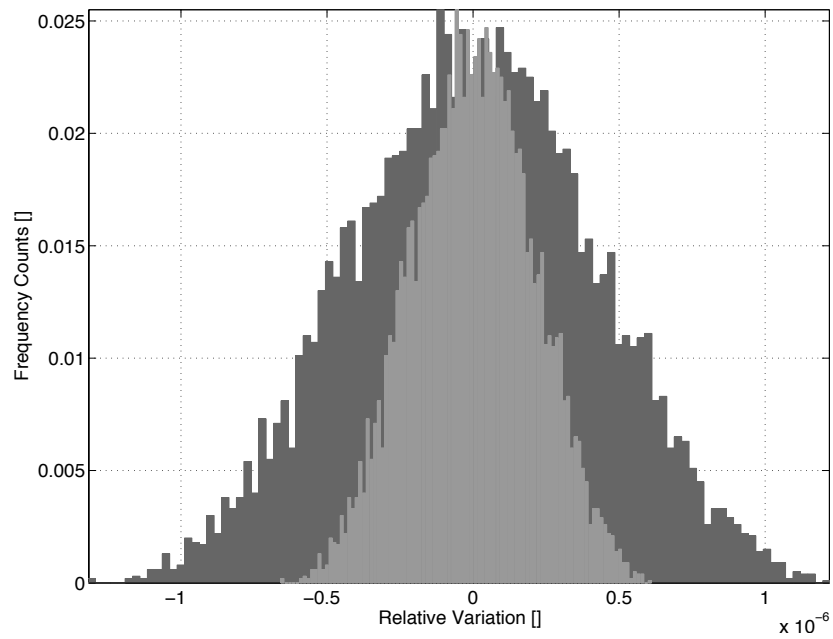


Figure 31: Histograms of the relative variations of  $p$  (dark grey), and  $k_s$  (light grey) due to mirror displacements. The histograms of the relative variations of  $p$  and  $\|\mathbf{a}\|$  are similar.

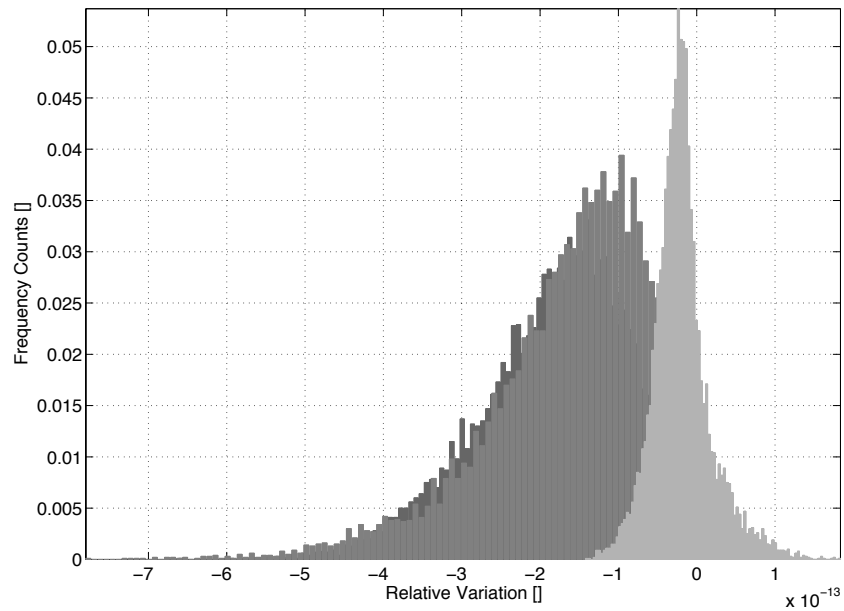


Figure 32: Histograms of the relative variations of  $p$  (dark grey), and  $k_s$  (light grey) due to mirror displacements. In all simulations the values of the first two diagonal entries of the matrix  $A$  were fixed to 2.87.

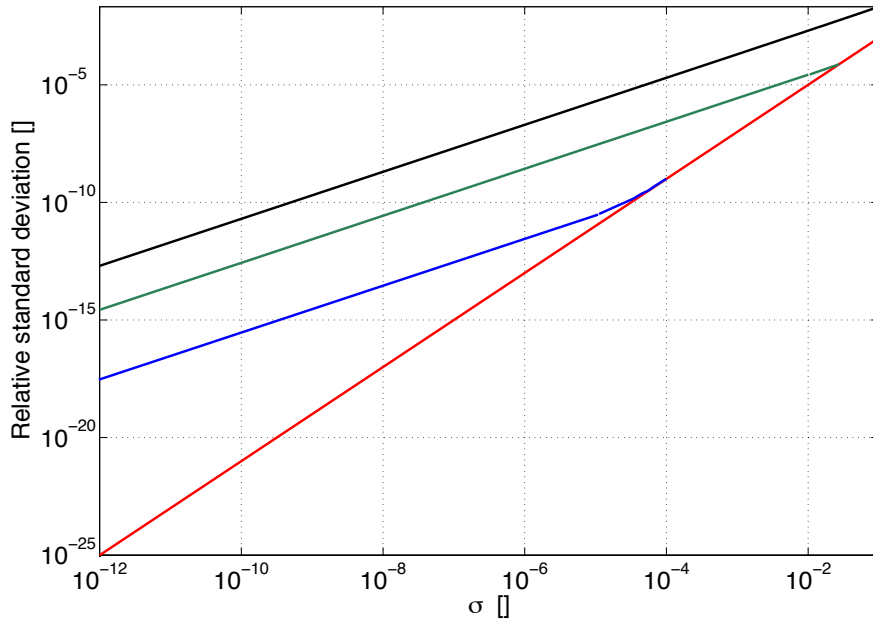


Figure 33: Relative standard deviation of  $k_S$  as a function of  $\sigma$  in the 4 cases: unconstrained ring (black), ring with constrained diagonal elements of  $T$  (red), intermediate case with  $\epsilon_d = 10^{-3}$  (green), and  $\epsilon_d = 10^{-6}$  (blue).

there the diagonal elements of  $A$  were biased by  $\pm\epsilon_d$ , with  $\epsilon_d = 10^{-3}$  and  $\epsilon_d = 10^{-6}$ .

In Fig. 33 we show the relative standard deviation of  $k_S$  as a function of  $\sigma$  for the 4 cases. It is clear that, for an unconstrained ring cavity, to achieve a relative accuracy of 1 part in  $10^{10}$  one must have almost the same relative accuracy on the mirrors displacements. On the other hand, a relative accuracy on the mirrors displacements of  $10^{-5}$  is enough for a constrained ring cavity. A small diagonal bias of 1 part in  $10^6$  does not affect the accuracy of  $k_s$  up to 1 part in  $10^{10}$ .





## COMPLETE RLG MODEL

---

In this Chapter we illustrate a detailed high accuracy simulation of the relevant processes involved in the operation of *RLGs*. The models for the *RL* dynamics, the *He – Ne* gain process, the light backscattering, and the laser beams displacement in the resonant optical cavity are merged together in a complete *RLG* model. Such model has been developed in *MATLAB*® software and *Simulink*, and it allows us to simulate the effects of control loops on *RLG* parameters and outputs. To our knowledge these effects are studied for the first time. The complete *RLG* model also permits to forecast the effect of hardware changes, being a powerful tool for *RLG* design and optimization.

### 4.1 COMPLETE RLG MODEL OVERVIEW

The complete *RLG* model provides realizations of the relevant physical processes discussed in this thesis, starting from the processes that constitutes the inputs of the simulation. These processes are then interconnected into a system which emulates the operation of a *RLG*, using the results of Chapters 2 and 3. We compute the laser beams path, the *Lamb* parameters set, and the *RLG* outputs for the given input signals. The diagonal lengths of the optical cavity  $d_1, d_2$  and the value of the monobeam intensity  $I_1$  are connected in feedbacks acting respectively on cavity geometry and on the laser single pass gain  $G$ . The schematic of the *Simulink* implementation of the complete *RLG* model is shown in Figure 34. As a case study we present the simulation of *GP2*. In particular, we simulate the feedback loops acting on the optical cavity length by means of piezoelectric transducers, and on light intensity by means of the radio-frequency circuit. Referring to the flowchart diagram of Figure 35 we describe in some detail the blocks: *IN*, *RLG\_CAV*, *RLG\_PAR*, *RLG\_DYN*, and *OUT*.

#### 4.1.1 *IN:Simulation parameters*

The *RLG* model depends on a wide set of parameters, including all the constants given in this thesis. The parameters that should be supplied to the model by the user are now listed:

- $L$  side length of the *RL*;
- $\Omega$  earth rotation vector;
- $\mathbf{n}$  *RL* orientation;



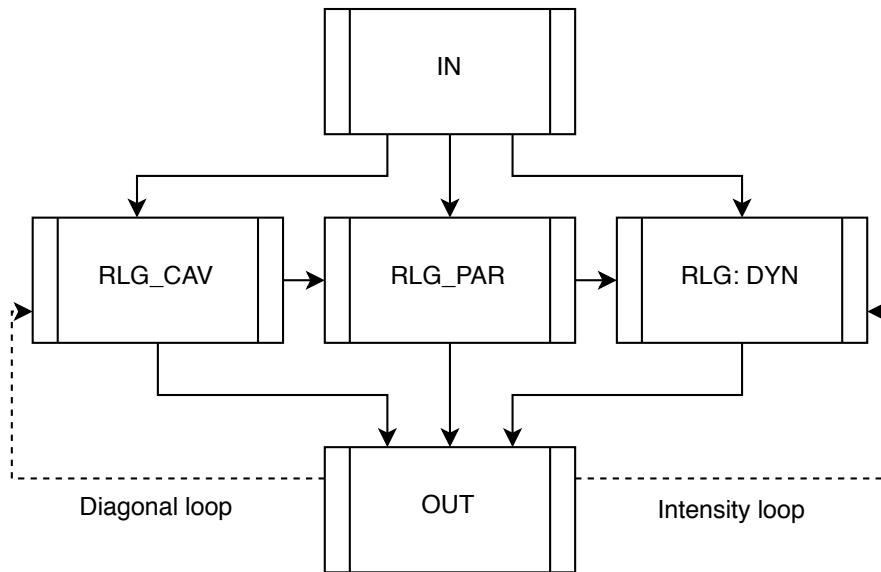


Figure 35: Flowchart diagram of the complete *RLG* model. The continuous lines represent the data shared between blocks, and the dashed lines indicate the presence of feedback loops.

- $G_0$  initial value for the laser single pass gain;
- $k_c$  *Ne* isotopic concentration in the gas mixture;
- $f_c$  the gain center frequency;
- $C_0$  initial condition of mirror centers matrix;
- $R$  mirror radii matrix;

Note that if the input signals are generated by a parametric generator in *Simulink*, these parameters must be supplied too.

#### 4.1.2 IN: Signal & noise generation block

In this block all the input signals for the *RLG* model are generated at the rate of 1 Hz. The rate has been chose accordingly to be much more lower than the time in which the physical processes involved show significant variations. The generated signals are now listed:

- The stochastic processes  $w_1, w_2, w_3, w_4$  that represent the velocity drifts of the mirrors in the optical cavity;
- The are stochastic processes  $\mu_1, \mu_2$  that represent the fluctuations of the reflectivity of the cavity mirrors;
- The stochastic process *press* representing the fluctuations of the pressure of the atomic *He – Ne* gas mixture;

- The stochastic process  $temp$  representing the drifts of the temperature of the plasma;
- The stochastic processes  $r_{ij}$  that represent the fluctuations of the scattering coefficients of each of the cavity mirrors  $M_i$   $i = 1, 2, 3, 4$  for the propagation direction  $j = 1, 2$ ;
- The stochastic processes  $e_{ij}$  that represent the fluctuations of the scattering angles of the mirrors of  $M_i$   $i = 1, 2, 3, 4$  of the optical cavity, for the propagation direction  $j = 1, 2$ .
- The generated reference signal  $d_{ref}$  for the feedback loop on the diagonal lengths of the optical cavity;
- The generated reference signals  $I_{1ref}$  for the feedback loop on the clockwise intensity  $I_1$ .

#### 4.1.3 RLG\_CAV: Optical cavity model

At each iteration  $k$  the vectors representing the mirrors velocity drifts  $w_1(t_k), w_2(t_k), w_3(t_k), w_4(t_k)$ , and the actions of the controls of the cavity diagonals  $a(t_k), b(t_k)$ , are integrated over time and added to the corresponding column in the initial condition matrix  $C_0$  to give the current centers matrix (see Subsection 3.1.2)

$$C(t) = C_0 + [w_1, w_2, w_3, w_4] + [a, b, -a, -b]. \quad (118)$$

The matrix  $C(t_k)$  is then employed together with the radii matrix  $R$  in the calculation of the laser beams positions  $X^*(C(t_k), R)$  on the cavity mirrors, via the geometric Newton Algorithm 3.1.4. The coordinates of the laser beams on the cavity mirrors are retained as  $Z(t_k) = X^*(C(t_k), R)R + C(t_k)$ , as in Subsection 3.1.5. From the matrix  $Z(t_k)$  the relevant lengths of the optical cavity and the vector area are computed as

$$\left\{ \begin{array}{l} l_1(t_k) = \|\mathbf{z}_1(t_k) - \mathbf{z}_2(t_k)\| \\ l_2(t_k) = \|\mathbf{z}_2(t_k) - \mathbf{z}_3(t_k)\| \\ l_3(t_k) = \|\mathbf{z}_3(t_k) - \mathbf{z}_4(t_k)\| \\ l_4(t_k) = \|\mathbf{z}_4(t_k) - \mathbf{z}_1(t_k)\| \\ d_1(t_k) = \|\mathbf{z}_1(t_k) - \mathbf{z}_3(t_k)\| \\ d_2(t_k) = \|\mathbf{z}_2(t_k) - \mathbf{z}_4(t_k)\| \\ p(t_k) = l_1(t_k) + l_2(t_k) + l_3(t_k) + l_4(t_k) \\ \mathbf{A}(t_k) = \frac{(\mathbf{z}_1(t_k) - \mathbf{z}_3(t_k)) \wedge (\mathbf{z}_2(t_k) - \mathbf{z}_4(t_k))}{2} \end{array} \right., \quad (119)$$

where  $\wedge$  is the wedge product in  $\mathbb{R}^3$ .

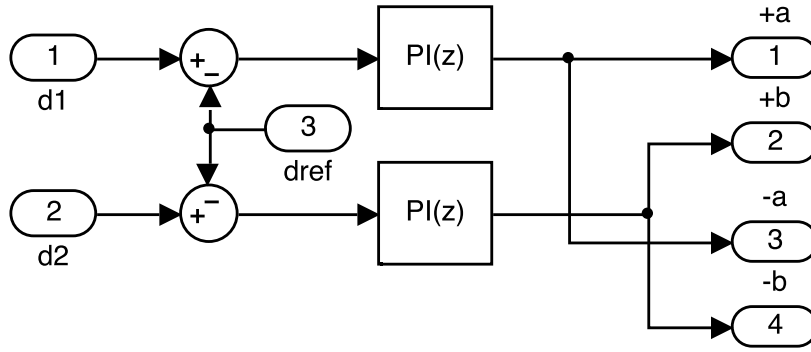


Figure 36: *Simulink* block for the diagonal loop.

#### 4.1.4 Diagonal loop

The signals  $d_1, d_2$  are then compared with a reference signal  $d_{ref}$  and fed back to two *PI* controllers suitably tuned. The outputs of the controllers are fed to the simple model of 4 piezoelectric actuators, paired two by two, pushing the mirrors  $M_1, M_2, M_3, M_4$ , in the directions  $\mathbf{e}_1, \mathbf{e}_2, -\mathbf{e}_1, -\mathbf{e}_2$ , as can be seen in the schematic in Figure 36. The output of this subsystem are the four vectors  $+a, +b, -a, -b$  that represents the feedback actions of the cavity diagonals control scheme.

#### 4.1.5 RLG\_PAR: Backscattering and detuning model

At each iteration  $k$  the backscattering coefficients  $r_1(t_k), r_2(t_k)$  and the backscattering phases  $\varepsilon_1(t_k), \varepsilon_2(t_k)$  are computed in dependence of the  $r_{ij}(t_k), e_{ij}(t_k)$ , and  $l_i(t_k), i = 1, \dots, 4, j = 1, 2$ , using the model discussed in Subsection 2.2.2 with the positions  $\varepsilon_j^{(i)} = e_{ij}(t_k)$  and  $\rho_j^{(i)} = r_{ij}(t_k)$ . Moreover, the optical path length  $p(t_k)$  is used to compute  $detn(t_k)$ , i.e. the mean of detunings  $\xi_{1,2}$  of the optical frequencies  $\omega_{1,2}$  from the gain center frequency  $\omega_0 = 2\pi f_c$ , see Subsection 2.2.1 for details. Finally, the *Sagnac* frequency  $f_s(t_k)$  is computed as in Eq.(1), as a function of the Earth rotation vector  $\Omega$ , the *RL* orientation  $\mathbf{n}$ , the compactness factor  $\|\mathbf{A}\|/p$ , with  $k_{sf} = 4\mathbf{A}/(\lambda p)$ , where  $\lambda$  is the light wavelength.

#### 4.1.6 RLG\_PAR: He – Ne laser model & Lamb Parameters

The components of the complex plasma dispersion functions  $z_\alpha = z^{(0)}(\xi), z_\beta = z_s^{(2)}(\xi_{1,2}), z_\theta + iz_\tau = z_c^{(2)}(\xi_{1,2})$  for the *He – Ne* laser system are computed in dependence on the detuning  $detn$ , the gain center frequency  $f_c$ , the gas pressure  $press$ , the plasma temperature

$temp$ , the isotopic  $Ne$  concentration  $k_c$ , and using the relations (27) of Subsection 2.2.1.

Once the plasma dispersion components are computed, at each iteration  $k$  the Lamb parameters set

$$[\alpha_1(t_k), \alpha_2(t_k), \beta(t_k), \theta(t_k), \tau(t_k)] \quad (120)$$

is computed using the components of the complex plasma dispersion function  $z_\alpha(t_k), z_\beta(t_k), z_\theta(t_k), z_\tau(t_k)$ , the mirror losses  $\mu_1(t_k), \mu_2(t_k)$ , the laser single pass gain  $G(t_k)$  and (19), (20) of Subsection 2.2.1.

#### 4.1.7 RLG\_DYN: RL dynamics integrator

The part of the RLG model that deals with laser intensities and phases is up sampled to the rate of 5 kHz. The RL dynamics for  $I_1, I_2$  and  $\psi$  are numerically integrated using (12) of Subsection 2.1.2, in dependence of the Lamb parameters  $[\alpha_1, \alpha_2, \beta, \theta, \tau]$  and the backscattering parameters  $[r_1, r_2, \varepsilon_1, \varepsilon_2]$ . The initial conditions for the integration can be set as  $I_1(0) = \alpha_1(0)/\beta(0)$ ,  $I_2(0) = \alpha_2(0)/\beta(0)$ ,  $\psi(0) = 0$ . The integration has been carried out in *Simulink* environment for continuous time systems exploiting the variable time step solver ODE45. At each iteration  $t$ , the in phase and in quadrature components of the interferogram signal  $S_1(t), S_2(t)$  and the monobeam intensities  $I_1(t), I_2(t)$  are saved as simulation outputs, their expressions is given by (16) and (18) of Subsection 2.1.3, with  $h_{1,2} = 1$ ,  $c_{1,2,3} = 1$ ,  $c_4 = 0$ .

#### 4.1.8 Intensity loop

The laser monobeam intensity  $I_1$  is filtered to get rid of the modulation, down sampled, and compared to the reference value  $I_{1ref}$ . The error signal is then fed back to a PI controller suitably tuned, that feeds in its turn the single pass gain channel  $G(t_k)$ . This simple model mimics the action of a feedback on the clockwise intensity of a RL, where the action on the laser gain is usually implemented varying the tension of the radio-frequency circuit.

#### 4.1.9 OUT: Simulation outputs

The RLG model allow for the detailed simulation of the following physical processes:

- the RL state  $\{I_1(t), I_2(t), S_1(t), S_2(t)\}$ , where  $S_{1,2}(t)$  are the in and out of phase components of the interferogram signal;
- the lengths of the optical cavity  $l_1, l_2, l_3, l_4, d_1, d_2$ ;
- the optical path  $p$ ;

- the vector area  $\mathbf{A}$  of the  $RL$ ;
- the Lamb parameters set  $[\alpha_1, \alpha_2, \beta, \theta, \tau]$ ;
- the backscattering parameters set  $[r_1, r_2, \varepsilon]$ ;
- the *Sagnac* frequency  $f_s$ .

#### 4.2 RESULTS OF THE COMPLETE SIMULATION OF GP2

The  $RLG$  model has been employed to simulate the dynamics of the resonant optical cavity and of the beat note of the  $RLG$   $GP2$ . A simulation of 1 h has been run, generating at the rate of 1 Hz the input signals. The parameters of the  $RLG$  model have been chosen as:  $L = 1.35$  m;  $\Omega = 2\pi/86164.0916$ ;  $\mathbf{n} = [\sin(0.2574\pi), 0, \cos(0.2574\pi)]$ ;  $G_0 = 1.20055 \times 10^{-4}$ ;  $k_c = 0.5$ ;  $f_c = 43.302$  MHz; the entries of the matrix  $C_0$  of the initial position of the mirror centers has been chosen as i.i.d. r.v. with mean given by the corresponding element of in (85) Subsection 3.1.5, and standard deviation  $10^{-4}$  m; finally, the mirror radii i.e. the diagonal entries of the matrix  $R$  has been chosen all equal to 4 m.

The stochastic processes were generated as white noise independent stochastic processes, whose means and variances are now listed:

- Each of the stochastic processes  $w_1, w_2, w_3, w_4$  has been simulated with null mean and standard deviation equal to  $10^{-8}$ ;
- The are stochastic processes  $\mu_1, \mu_2$  have been simulated with mean equal to  $10^{-4} \pm 10^{-7}$ , respectively, and standard deviation  $10^{-8}$ ;
- The stochastic process *press* have been simulated with mean 7.5 mbar and standard deviation  $10^{-4}$  mbar;
- The stochastic process *temp* have been simulated with mean 450 K and standard deviation  $10^{-2}$  K;
- Each of the stochastic processes  $r_{ij}$  has been simulated with mean value taken as i.i.d. uniform random variable in the range  $[0; 2 \times 10^{-7}]$ , and with standard deviation  $10^{-10}$ .
- Each of the stochastic processes  $e_{ij}$  has been simulated with mean value taken as i.i.d. uniform random variable in the range  $[0; 2\pi]$ , and with standard deviation  $10^{-10}$ .

The reference signals  $d_{ref}$  and  $I_{1ref}$  for the feedback loops have been generated as constant signals, with value 6.0908 m and  $2 \times 10^{-3}$ , respectively. The initial conditions for the integration have been set as  $I_1(0) = I_2(0) = 10^{-3}$ ,  $\psi(0) = 0$ .

In Figure 37 are shown the simulated stochastic processes for the mirror losses  $\mu_{1,2}$ , the plasma temperature  $temp$  and the gas pressure  $press$ .

Figure 38 displays some of the simulated lengths of the optical cavity, i.e. the four sides  $l_{1,2,3,4}$

In Figure 39 are shown the remaining lengths of the optical cavity, i.e. the perimeter  $p$  and the two diagonals  $d_{1,2}$ .

Figure 40 displays the simulated *Sagnac* frequency.

In Figure 41 the Lamb parameters  $[\alpha_1, \alpha_2, \beta, \theta, \tau]$  and the backscattering parameters  $[r_1, r_2, \varepsilon]$  are displayed as an output of the simulation.

Finally, in Figure 42, the in-phase  $S_1$  and in-quadrature  $S_2$  components of the interferogram signal, and the light intensities  $I_{1,2}$  are displayed.



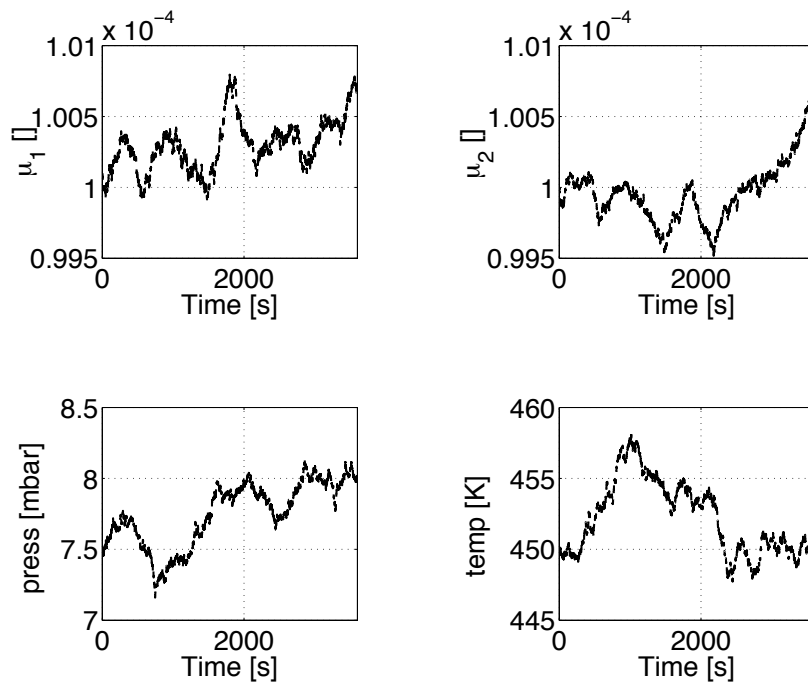


Figure 37: Realization of  $\mu_{1,2}$ ,  $temp$  and  $press$  for the simulation case study.

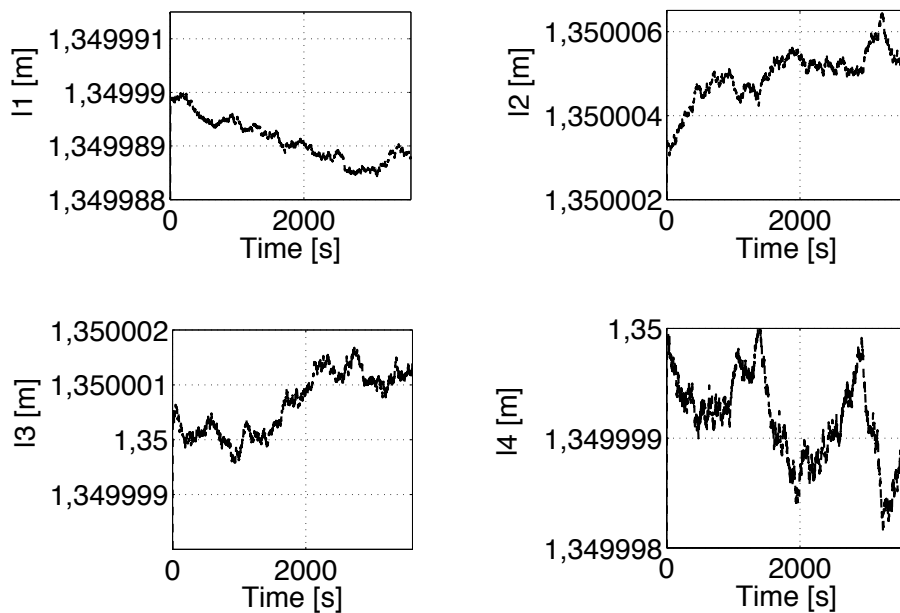


Figure 38: Optical cavity lengths  $l_{1,2,3,4}$  resulting for the simulation case study.

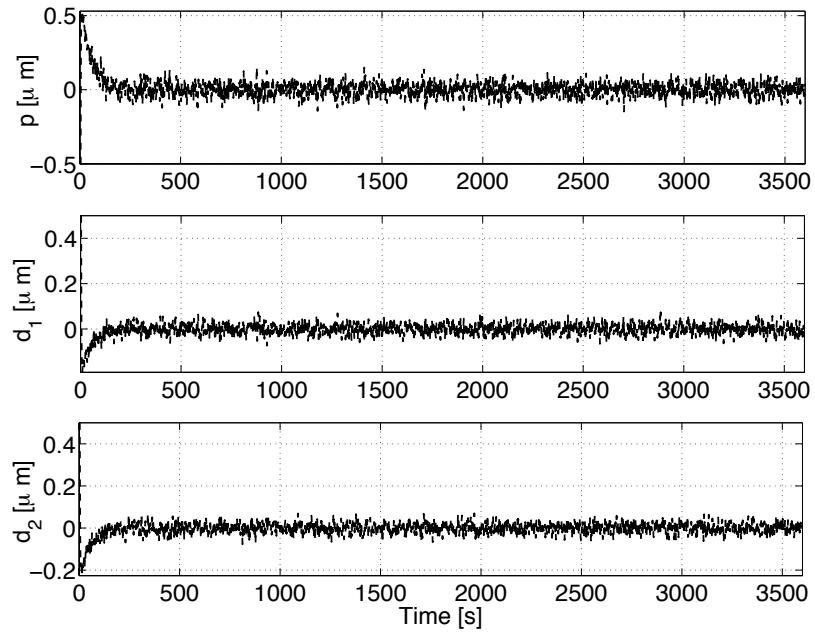


Figure 39: Optical cavity lengths  $d_{1,2}$  and  $p$  resulting for the simulation case study.

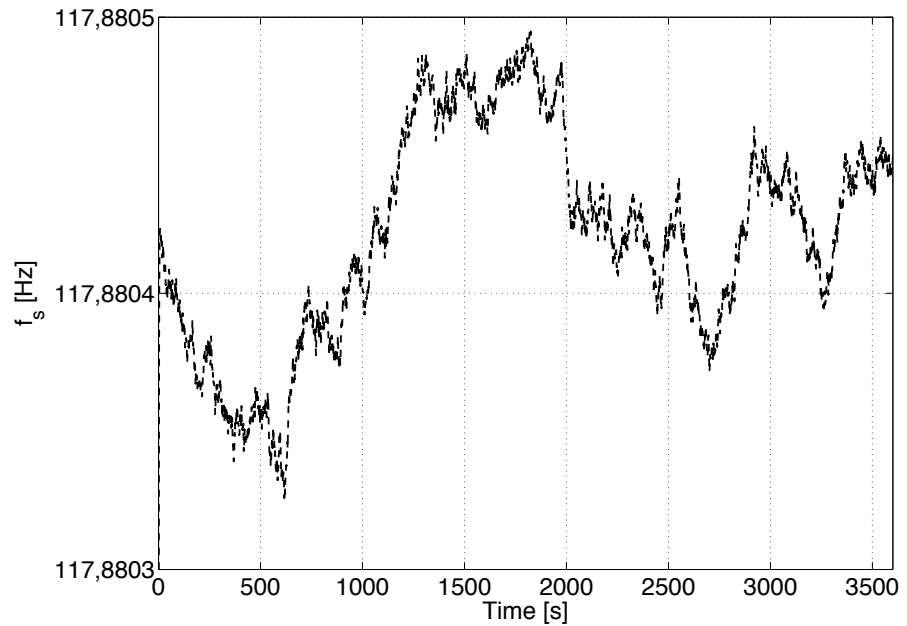


Figure 40: Sagnac frequency  $f_s$  as a result of the simulation case study.

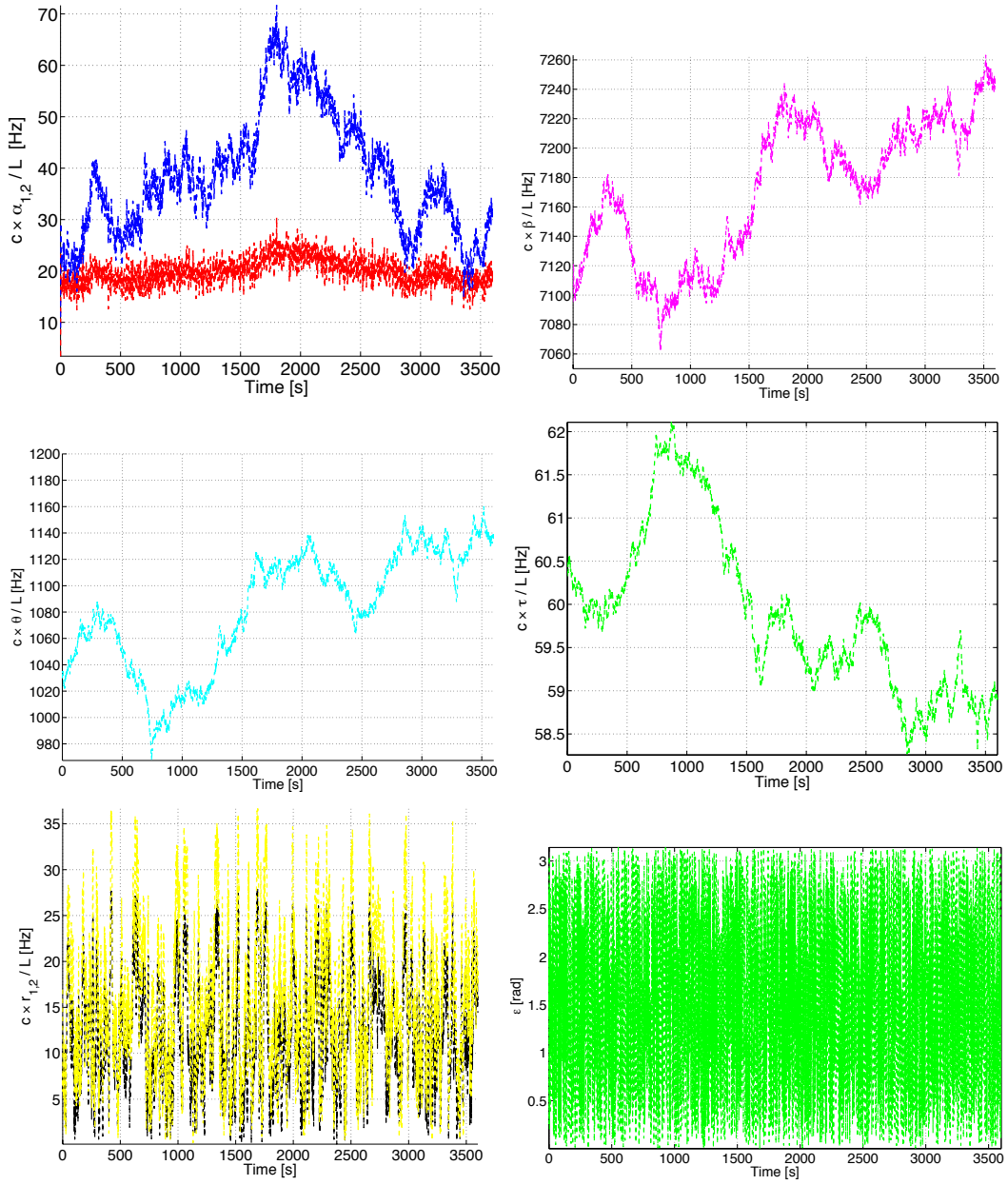
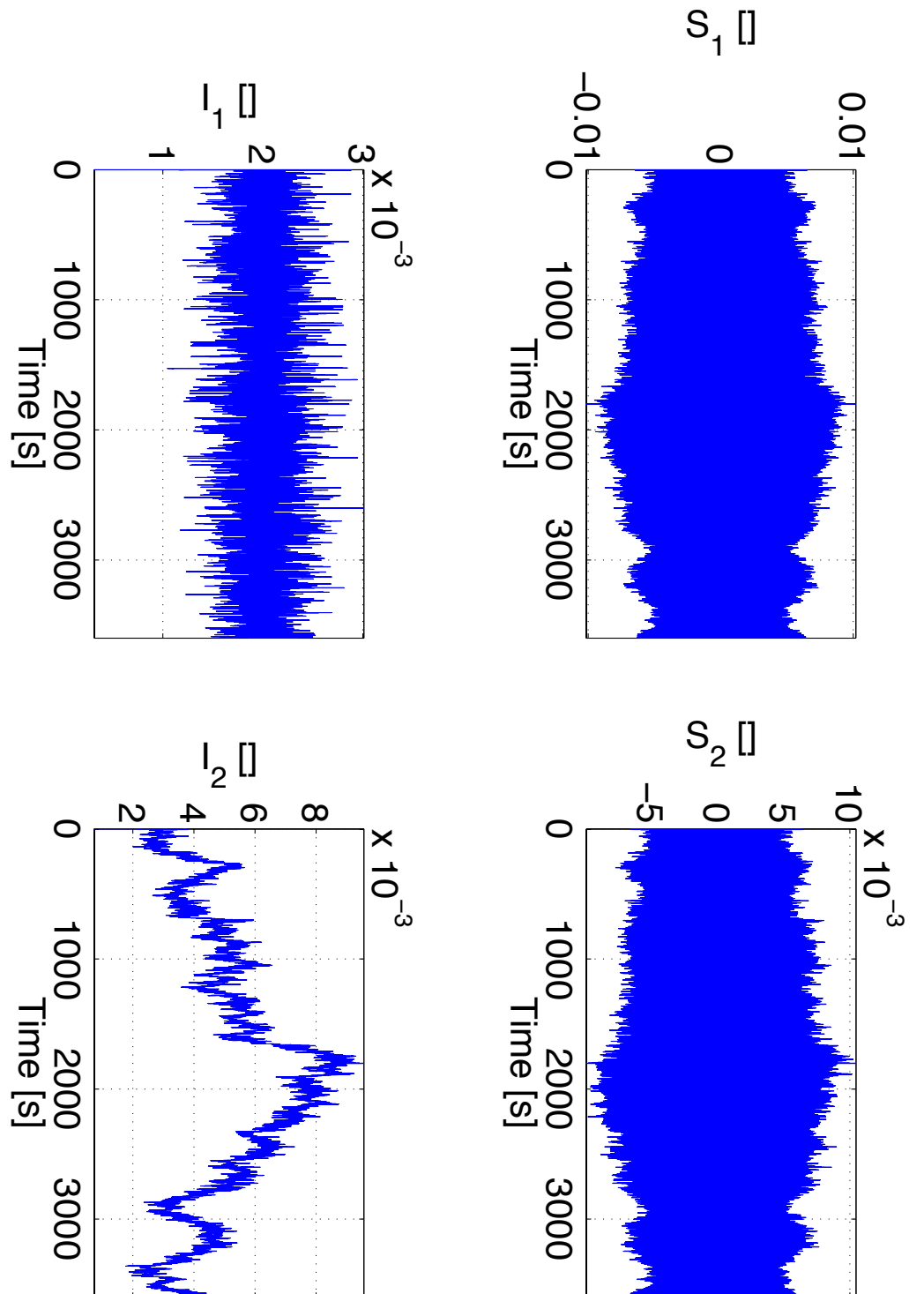


Figure 41: Lamb parameters and backscattering parameters for the simulation case study.

Figure 42: Plot of the simulated  $S_{1,2}$  and  $I_{1,2}$ .

## CONCLUSIONS

---

### 5.1 RING LASER DYNAMICS

In Chapter 2 a model of the *RL* dynamics has been studied, and then applied to the design of identification and calibration methods for cold cavity and active medium *Lamb* parameters. The identification method is based on the first harmonic approximation of the steady state solution of *RL* equations and the minimization of a quadratic functional over the Hilbert space of periodic signals. Results of Monte Carlo simulations supported the viability of the dissipative parameter estimation by yielding a relative estimation error of  $\sim 3 \times 10^{-3}$  for  $\alpha_{1,2}$  and  $r_{1,2}$ , and an estimation error of  $\sim 10^{-3}$  rad for  $\epsilon$ . On the other hand, the dynamics of a laser with cavity detuning shows many monomode or multimode dynamical behaviors that can be exploited to get rid of systematic errors in the estimation of the *Sagnac* frequency. The calibration method presented in this thesis is based on the measures of the threshold of multimode transition and the plasma dispersion function. The accurate estimation of the *Lamb* parameters allows for the application of the *Kalman* filter for the estimation of the Earth rotation rate. We have shown that the parameters of the *RL* dynamics can be identified, and their effects on resolution and long term stability removed, notwithstanding the system non linearities. Simulations showed a significant improvement in the *Sagnac* frequency estimation by means of *EKF* compared to the standard *AR(2)* method. The results we got, using the data of the *RLG* prototype *G-PISA*, make us confident about the reliability of our approach in the presence of unmodeled experimental noise and calibration errors. The systematic errors associated with the calibration measurements dominate over statistical errors, as plasma parameters depend also on radio-frequency circuit details, e.g. the capillary shape. However, the accuracy of the identified cold cavity parameters depends on the amount of losses and backscattering of light: higher quality mirrors lead to potentially higher accuracy of the estimated *Sagnac* frequency. We also reported some exciting results about the data of the *RLG* *G-WETTZELL*, obtained with no calibration of the instrument gain. However, much work has still to be devoted to improve calibration procedures and estimation of non-reciprocities for testing fundamental physics with *RLs*. Our approach can be further improved, and different mathematical tools can be used. For instance, there exist other dynamical filters (e.g. Unscented *Kalman* Filter, Particle filters, etc.) that could perform better than *EKF* in the presence of non linear dy-

namics, and the statistics used for the estimation of the *Lamb* parameters can be improved too. *RLGs* achieved world record in rotation sensitivity, accuracy and time stability with sophisticated hardware, accurate selection of the working point of the *He – Ne* laser, despite a very basic off-line analysis. We think that data analysis will cooperate more and more with *RLG* hardware in pushing the resolution and the time stability of *RLGs* forward the current limitations. The problem of pushing calibration and identification methods to their intrinsic accuracy limit, with or without the addition of a calibrated rotation signal to the *RLG* input, would deserve further investigation.

## 5.2 RING LASER GEOMETRY

We calculated the beam steering in optical cavities as a function of the mirror positions and orientations by means of the Fermat's principle. To find the stationary optical path in a polygonal cavity, we have used an extension of the Newton algorithm to Matrix Manifolds. Our approach is motivated by the need to compute the optical path of the laser beams in resonant cavities, and our results allow for the application of control techniques to constrain the beams path. With the help of the results obtained in ref.[1], we proved the correctness and quadratic convergence rate of our algorithm under mild assumptions of regularity of the function  $p$ . Using smoothness we showed that the function  $p$  meets the regularity requirements in a neighborhood of the point  $C^*$ , representing the perfectly aligned square cavity of side  $L$ . Monte Carlo simulations have shown that this neighborhood contains all the cavity configurations that can be encountered in practice for heterolithic *RLGs*. In fact, manufacture tolerances of a *RL* frame ensure  $\|C - C^*\| \sim 10^{-5}L$ , while we showed that our algorithm successfully evaluates the beams position in a square cavity with errors in mirror positioning or alignment up to  $10^{-3}L$ .

The geometric Newton method devised has been reported to provide a relative accuracy of  $10^{-12}$  in evaluating the optical cavity configuration of a square *RL*. It is worth noticing that greater precision may be achieved, even if not of physical interest. We found that the computational cost of the proposed method is low, since at most 3 iterations are required to reach the desired precision in the Riemannian gradient norm during the Monte Carlo simulation. We also derived a decomposition, suitable for the mirror centers matrix of a square *RL*, capable to separately account for the shape and pose of the mirror centers. By this decomposition we derived a model for the deformations of the optical cavity of a square *RL*, and one remarkable result of this model is the existence of closed form solution to the triangulation problem to find the coordinates of the mirrors centers given the 6 distances among them.

The treatment of an optical cavity in the framework of differential geometry is more suitable for an extension of geometrical optics formalism which includes also the description of Gaussian beams.

Once the laser beam configuration in the cavity is determined by Fermat's principle, the calibration and active control of the optical cavity can be formulated as a optimization problem. However, a suitable description of the cavity configurations, and a dynamical model for the active control of the light path in resonant cavities are still issues which require further researches.

Such further investigations will allow us to estimate the sensitivity and long term stability of heterolithic RLGs, with the aim to highlight their promising applications to the fundamental physics, e.g. General Relativity or Axion detection.

### 5.3 COMPLETE RLG MODEL

A complete high accuracy simulation of the relevant processes involved in the operation the RLG GP2 has been performed. The complete RLG model accounts for, the RL dynamics, the He – Ne gain process, the light backscattering process, and the laser beams displacement in the resonant cavity. The RLG model has been developed using MATLAB® and Simulink, and allow for the simulation of the effects of the control loops implemented in high resolution RLGs as GP2 on the RL parameters and output. For the first time these effects have been studied with completeness and precision. The model developed is a powerful tool for the design and operation of high accuracy RLGs, as it permits to forecast the effect of hardware upgrades.





## APPENDIX

---

### A.1 PROOF OF PROPOSITION 1

We recall that and  $\mathbf{e}_k$  are the canonical basis vectors of  $\mathbb{R}^N$ . Suppose that  $\text{grad } f_k(X) \neq \mathbf{0}$  for  $k = 1, \dots, N$ . each  $X_k$  is orthogonal to the corresponding  $\text{grad } f_k(X)$  by the definition of  $T_X \mathcal{OB}(2, N)$  since  $X_k \neq \mathbf{0}$  and  $\text{grad } f_k(X) \neq \mathbf{0}$ . Therefore the vectors  $\mathbf{v}_k = \text{grad } f_k(X) \otimes \mathbf{e}_k$  and  $\mathbf{w}_k = (\text{grad } f_k(X) \wedge X_k) \otimes \mathbf{e}_k$  are mutually orthogonal, and they belongs to  $T_X \mathcal{OB}(2, N)$  by construction, therefore the set  $\{\mathbf{v}_1, \dots, \mathbf{v}_N, \mathbf{w}_1, \dots, \mathbf{w}_N\}$  is a basis of  $T_X \mathcal{OB}(2, N)$ . The vectors  $\mathbf{q}_k = X_k \otimes \mathbf{e}_k$ , are mutually orthogonal and belong to the normal space of  $T_X \mathcal{OB}(2, N)$ ; therefore  $(\mathbf{v}_1, \dots, \mathbf{v}_N, \mathbf{w}_1, \dots, \mathbf{w}_N, \mathbf{q}_1, \dots, \mathbf{q}_N)$  is a suitable basis of  $T_x \mathbb{R}^{3 \times N}$  and

$$T(X) = (\text{vect } \mathbf{v}_1, \dots, \text{vect } \mathbf{v}_N, \text{vect } \mathbf{w}_1, \dots, \text{vect } \mathbf{w}_N, \text{vect } \mathbf{q}_1, \dots, \text{vect } \mathbf{q}_N)^T \quad (121)$$

is the basis change matrix associated.

To prove the proposition we recast (60) in a suitable form. We get

$$T(X) \text{vect } \eta_X = \begin{pmatrix} \mathbf{y}(X) \\ 0 \end{pmatrix}, \quad T(X) \mathbf{z}(X) = \begin{pmatrix} \mathbf{g}(X) \\ 0 \end{pmatrix}, \quad (122)$$

Defining the matrix  $\tilde{H}(X) \in \mathbb{R}^{12 \times 12}$ , where  $\tilde{H}_{ik}(X) = \langle \mathbf{e}_i, \text{Hess } f(X)[\mathbf{e}_k] \rangle$ , the Newton Equation (60) can be rewritten as

$$H(X) \mathbf{y}(X) = \mathbf{g}(X), \quad (123)$$

where  $\mathbf{y}(X) \in \mathbb{R}^{2N}$  and  $H(X)$  is the principal minor of  $T(X) \tilde{H}(X) T(X)^T$  with indexes ranging from 1 to  $2N$ .

If the Matrix  $H(X)$  is not singular, an expression for the Newton vector at each iteration is therefore:  $\text{vect } \mathbf{J}_X = T(X)^T (H(X)^{-1} \mathbf{g}(X), 0)^T$ .

### A.2 PROOF OF LEMMA 6

Note that within the assumptions made neither  $\mathbf{a}$  nor  $\mathbf{b}$  can be the equal to the null vector, so both  $\mathbf{u}$  and  $\mathbf{v}$  are not equal to the null vector.

One can check by inspection of the product  $RC$  that is  $RC = [\mathbf{a}, \mathbf{b}]$ , and that the diagonal elements of  $C$  are positives.

Suppose now that there exists another rotation matrix  $R'$  and another upper triangular matrix  $C' \in \mathbb{R}^{3 \times 2}$  such that

$$R' C' = RC = [\mathbf{a}, \mathbf{b}] . \quad (124)$$

Rewriting (124) for the first column of  $C$  and  $C'$  we get

$$R' C'_1 = RC_1 = \mathbf{a} , \quad (125)$$

Since both  $C_1$  and  $C'_1$  have the last two components equal to zero, by normalizing the three columns involved in (125) we get  $R_1 = R'_1 = \mathbf{a} / \|\mathbf{a}\|$ . Moreover, taking the norms of the each column in (125), we get  $c_{11} = c'_{11} = \|\mathbf{a}\|$ .

Consider now (124) rewritten for the second column of  $C$  and  $C'$ , we get

$$R' C'_2 = RC_2 = \mathbf{b} , \quad (126)$$

and writing component-wise in  $C_2$  and  $C'_2$  the last relation we get

$$R_1 c_{12} + R_2 c_{22} = R'_1 c'_{12} + R'_2 c'_{22} \quad (127)$$

since it is  $R_1 = R'_1$ , by multiplying the parts of (127) by  $R_1^T$  and recalling that the columns of a rotation matrix are an orthonormal set of vectors, we get  $c_{12} = c'_{12}$ .

From (127) we finally have that  $R_2 c_{22} = R'_2 c'_{22}$ , normalizing the two columns and taking again the norms of the each part of the latter relations we get the thesis.

## BIBLIOGRAPHY

---

- [1] P.-A. Absil, R. Mahony, and R. Sepulchre. *Optimization Algorithms on Matrix Manifolds*. Princeton University Press, 2008. (Cited on pages [54](#), [58](#), [59](#), [60](#), [61](#), [63](#), [64](#), and [96](#).)
- [2] P. A. Absil, Robert Mahony, and Jochen Trumpf. An extrinsic look at the riemannian hessian. In *Geometric Science of Information*, page 8085, 2013. (Cited on pages [59](#), [61](#), and [63](#).)
- [3] G. Ajoy. *Optics (4th ed.)*. McGraw Hill, 2010. (Cited on page [58](#).)
- [4] G. B. Al'tshuler, E. D. Isyanova, V. B. Karasev, A. L. Levit, V. M. Ovchinnikov, and S. F. Sharlai. Analysis of misalignment sensitivity of ring laser resonators. *Sov. J. Quantum Electron*, 7(7):857–859, July 1977. (Cited on page [7](#).)
- [5] D. Z. Anderson. Alignment of resonant optical cavities. *Applied Optics*, 23(17):2944–2949, September 1984. (Cited on page [7](#).)
- [6] L. Armijo. Minimization of functions having lipschitz continuous first partial derivatives. *Pacific journal of Mathematics*, 16(1):1–3, January 1966. (Cited on pages [60](#) and [63](#).)
- [7] F. Aronowitz. Theory of a travelling wave optical maser. *Physical Review*, 139(3A):A635–A645, December 1965. (Cited on pages [6](#), [13](#), [15](#), [18](#), and [23](#).)
- [8] F. Aronowitz. Optical gyros and their application. RTO AGAR-Dograph 339, RTO/NATO, BP 25, 7 rue Ancelle, F-92201 Neuilly-sur-Seine cedex, France, May 1999. (Cited on page [6](#).)
- [9] F. Aronowitz and R. J. Collins. Lock-in and intensity-phase interaction in the ring laser. *Journal of Applied Physics*, 41(1):131–141, January 1970. (Cited on pages [6](#), [13](#), [15](#), and [18](#).)
- [10] A. Bambini and S. Stenholm. Theory of a dithered-ring-laser gyroscope: A floquet-theory treatment. *Physical Review A*, 31(1):329–337, January 1985. (Cited on page [6](#).)
- [11] M. A. Bandres and M. Guizar-Sicairos. Paraxial group. *Optics Letters*, 34(1):13–15, January 2009. (Cited on page [7](#).)
- [12] P. S. Begum and N. Neelima. Development of control algorithm for ring laser gyroscope. *International Journal of Scientific and Research Publications*, 2(10):1–6, October 2012. (Cited on page [7](#).)

- [13] H. R. Bilger and G. E. Stedman. Stability of planar ring lasers with mirror misalignment. *Applied Optics*, 26(17):3710–3716, September 1987. (Cited on page 7.)
- [14] F. Bosi, G. Cella, A. Di Virgilio, A. Ortolan, A. Porzio, S. Solimeno, M. Cerdonio, J.P. Zendri, M. Allegrini, J. Belfi, N. Beverini, B. Bouhadeh, G. Carelli, I. Ferrante, E. Maccioni, R. Passaquieti, F. Stefani, M.L. Ruggiero, A. Tartaglia, K.U. Schreiber, A. Gebauer, and J.-P. R. Wells. Measuring gravitomagnetic effects by a multi-ring-laser gyroscope. *Physical Review D*, 84(122002):1–23, December 2011. (Cited on pages 8, 54, and 64.)
- [15] N. Boumal. Discrete curve fitting on manifolds. Master’s thesis, Universite catholique de Louvain, Louvain-la-Neuve, June 2010. (Cited on pages 62 and 63.)
- [16] C. Etrich, Paul Mandel, R. Centeno Neelen, R. J. C. Spreeuw, and J. P. Woerdman. Dynamics of a ring-laser gyroscope with backscattering. *Physical Review A*, 46(1):525, 536, July 1992. (Cited on page 6.)
- [17] M. Chen, J. Yuan, Z. Wang, Y. Li, and X. Long. Practical method for eliminating the magnetic bias sensitivity of square ring laser gyros by adjusting the nonplanar angle. *Optics Communications*, 331:330–333, Genuary 2014. (Cited on page 7.)
- [18] W. R. Christian, E. C. Gage, and L. Mandel. Reducing the effects of backscattering on the behavior of a ring laser. *Optics Letters*, 12(5):328–330, May 1987. (Cited on page 6.)
- [19] W.R. Christian, T.H. Chyba, E.C. Gage, and L. Mandel. Observation of random  $\pi$  phase jumps in a ring laser with backscattering. *Optics Communications*, 66(4):238–244, May 1988. (Cited on page 6.)
- [20] T.H. Chyba. Phase-jump instability in the bidirectional ring laser with backscattering. *Physical Review A*, 40(11):6327–6338, December 1989. (Cited on page 6.)
- [21] T.H. Chyba. Deterministic solution to the inhomogeneously broadened bidirectional ring laser equations with backscattering, asymmetry and cavity rotation. *Optics Communications*, 76(5,6):395–405, May 1990. (Cited on pages 6 and 25.)
- [22] W.T. Coffey, Yu. P. Kalmykov, and E.S. Massawe. Effective-eigenvalue approach to the nonlinear langevin equation for the brownian motion in a tilted periodic potential. ii. application to the ringlaser gyroscope. *Physical Review E*, 48(2):699–704, August 1993. (Cited on page 6.)

- [23] J. D. Cresser. Quantum noise in ring-laser gyros. approximate analytic results in unlocked region. *Physical Review A*, 26(1):397–409, July 1982. (Cited on page 6.)
- [24] D. Cuccato. Identification and estimation procedures for the dynamics of a ring laser gyroscope, October 2011. (Cited on page 8.)
- [25] A.W.J. Dawkins. Clarification of aronowitz’s theory for the effects of back-scattering in a ring laser. *J. Phys. D: Appl. Phys.*, 14(L153):133–135, October 1981. (Cited on page 6.)
- [26] R. G. Defoe and R. G. Brewer. Laser-frequency division and stabilization. *Physical Review A*, 30(5):2827–2829, November 1984. (Cited on page 7.)
- [27] F. Dell’Olio, A. Di Nisi, and P. Lino F. Indiveri, C. Ciminelli, and M. N. Armenise. Backscattering noise control in the read-out circuit of innovative optoelectronic resonant gyroscopes. In IEEE, editor, *Photonics Technologies*, number 14415605 in 2014 Fotonica AEIT Italian Conference, pages 1–3. IEEE, 2014. (Cited on page 7.)
- [28] F. Dell’Olio, T. Tatoli, C. Ciminelli, and Armenise M. N. Recent advances in miniaturized optical gyroscopes. *J. Europ. Opt. Soc. Rap. Public.*, 9(14013):1–14, March 2014. (Cited on page 8.)
- [29] Z. Fan, H. Luo, G. Lu, and S. Hu. Online effective backscattering estimation for ring laser gyro. *CHINESE OPTICS LETTERS*, 10(5):051404–1/051404–3, May 2012. (Cited on page 7.)
- [30] M. Faucheux, D. Fayoux, and J.J. Roland. The ring laser gyro. *J. Optics*, 19(3):101–115, March 1988. (Cited on page 6.)
- [31] Yu. V. Filatov, D. P. Loukianov, and R. Probst. Dynamic angle measurement by means of a ring laser. *Metrologia*, 34(4):343–351, February 1997. (Cited on page 8.)
- [32] H. Goldstein. *Classical Mechanics*. Addison-Wesley, london edition, 1980. (Cited on page 27.)
- [33] R. Graham. *New Concepts for Operating Ring Laser Gyroscopes*. PhD thesis, University of Canterbury, Christchurch 8140, New Zealand, December 2010. (Cited on pages 8 and 30.)
- [34] R. D. Graham, R. B. Hurst, K-U. Schreiber, and J.-P. R. Wells. Mode selection in an ultralarge ring laser gyro. *Applied Optics*, 51(22):5592–5595, August 2012. (Cited on page 30.)
- [35] O. Graydon. Giant laser gyroscope detects earth’s wobble. *Nature Photonics*, 6(12):12, January 2012. (Cited on pages 8 and 53.)

- [36] L.M. Hoffer and N.B. Abraham. Analysis of a coherent model for a homogeneously broadened bidirectional ring laser. *Optic Communications*, 74(3,4):261–268, December 1989. (Cited on page 6.)
- [37] Honeywell. Honeywell site, October 2014. (Cited on page 1.)
- [38] Q. Hong, J. A. Ramswell, V. G. Stavros, C. J. Barnett, and H. H. Fielding. A nano-stabilization technique for low repetition rate phase-sensitive optical experiments. *Meas. Sci. Technol.*, 9:378–382, November 1998. (Cited on page 7.)
- [39] R. B. Hurst, R. W. Dunn, K. U. Schreiber, R. J. Thirkettle, and G. K. MacDonald. Mode behavior in ultralarge ring lasers. *Applied Optics*, 43(11):2337–2346, April 2004. (Cited on page 8.)
- [40] H. Igel, U. Schreiber, A. Flaws, B. Schuberth, A. Velikoseltsev, and A. Cochard. Rotational motions induced by the m8.1 tokachi-oki earthquake, september 25, 2003. *Geophys. Res. Lett.*, 32, April 2005. (Cited on page 8.)
- [41] D. G. Kendall. Shape manifolds, procustean metrics, and complex projective spaces. *Bull. London Math. Soc.*, 16:81–121, July 1984. (Cited on page 72.)
- [42] D. G. Kendall. A survey of the statistical theory of shape. *Statistical Science*, 4(2):87–120, 1989. (Cited on page 72.)
- [43] H. Kogelnik and T. Li. Laser beams and resonators. *Applied Optics*, 5(10):1550–1566, October 1966. (Cited on page 7.)
- [44] N. V. Kravtsov and N. N. Kravtsov. Nonreciprocal effects in ring lasers. *Quantum Electronics*, 29(5):378–399, December 1999. (Cited on page 7.)
- [45] X. Long and J. Yuan. Method for eliminating mismatching error in monolithic triaxial ring resonators. *Chinese Optics Letters*, 8(12):1135–1138, December 2010. (Cited on page 7.)
- [46] G. Lu, Z. Fan, S. Hu, and H. Luo. Mirrors movement-induced equivalent rotation effect in ring laser gyros. *Optics Express*, 21(12):14458–14465, June 2013. (Cited on page 7.)
- [47] W. M. Macek and Jr. D.T.M. Davis. Rotation rate sensing with travelling wave ring laser. *Applied Physics Letters*, 2(3):67–68, February 1963. (Cited on page 5.)
- [48] J. E. Marsden and T. Ratiu. *Manifolds, Tensor Analysis, and Applications*. Springer, 2002. (Cited on page 54.)
- [49] L. N. Menegozzi and Jr. W. E. Lamb. Theory of a ring laser. *Physical Review A*, 8(4):2103–2125, october 1973. (Cited on pages 5, 6, 13, and 23.)

- [50] P. Pasula and R. B. Natha. Implementation of control algorithm for ring laser gyroscope. *International Journal of Engineering Research and Applications*, 2(3):850–853, June 2012. (Cited on page 7.)
- [51] L. Pesquera, R. Blanco, and M. A. Rodriguez. Statistical properties of gas ring lasers with backscattering. *Physical Review A*, 39(11):5777–5784, June 1989. (Cited on pages 6 and 25.)
- [52] E. J. Post. Sagnac effect. *Rev. Mod. Phys.*, 39(2):475–493, April 1967. (Cited on pages 1 and 6.)
- [53] W. H. Press, S. A. Teukolsky, W. T. Vetterling, , and B. P. Flannery. *Numerical Recipes 3rd Edition, The Art of Scientific Computing*. Cambridge University Press, Sept. 2007. (Cited on pages 11 and 34.)
- [54] W. Qiao, Z. Xiaojun, L. Zongsen, W. Yonggang, S. Liqun, and N. Hanben. Simple method of optical ring cavity design and its applications. *Optics Express*, 22(12):14782–14791, June 2014. (Cited on page 7.)
- [55] G. Rizzi and M. L. Ruggiero. The relativistic sagnac effect: Two derivations. *Fundamental Theories of Physics*, 135:179–220, 2004. (Cited on page 1.)
- [56] R. Rodloff. A laser gyro with optimized resonator geometry. *IEEE journal of Quantum Electronics*, QE-23(4):438–446, April 1987. (Cited on page 7.)
- [57] B. E. A. Saleh and M. C. Teich. *Resonator Optics*. John Wiley & Sons, Inc, 2001. (Cited on page 54.)
- [58] R. Santagata. Controllo della stabilità geometrica di un sistema di gyrolaser. Master's thesis, Università di Napoli, Corso Umberto I, Ottobre 2011. (Cited on page 8.)
- [59] K. U. Schreiber, A. Gebauer, A. Velikoseltsev, and J.-P. R. Wells. Precision cavity control for the stable operation of a large ring laser gyroscope. In Institute of Electrical and Electronics Engineers, editors, *Laser Optics*. IEEE, June-July 2014. (Cited on pages 8 and 53.)
- [60] K. U. Schreiber, A. Gebauer, and J.-P. R. Wells. Long-term frequency stabilization of a 16 m<sup>2</sup> ring laser gyroscope. *Optics Letters*, 37(11):1925–1927, June 2012. (Cited on pages 8 and 54.)
- [61] K. U. Schreiber, A. Gebauer, and J.-P. R. Wells. Closed-loop locking of an optical frequency comb to a large ring laser. *Optics Letters*, 38(18):3574–3577, September 2013. (Cited on page 8.)

- [62] K. U. Schreiber, J. N. Hautmann, A. Velikoseltsev, J. Wassermann, H. Igel, J. Otero, F. Vernon, and J.-P. R. Wells. Ring laser measurements of ground rotations for seismology. *Bulletin of the Seismological Society of America*, 99(2B), May 2009. (Cited on page 8.)
- [63] K. U. Schreiber, T. Klügel, J.-P. R. Wells, R. B. Hurst, and A. Gebauer. How to detect the Chandler and the annual wobble of the Earth with a large ring laser gyroscope. *Physical Review Letters*, 107:173904-1/173904-4, October 2011. (Cited on pages 8 and 44.)
- [64] K. U. Schreiber, G. E. Stedman, H. Igel, and A. Flaws. *Earthquake Source Asymmetry, Structural Media and Rotation Effects*. Springer Berlin Heidelberg, 2006. (Cited on page 8.)
- [65] K. U. Schreiber and J.-P. R. Wells. Large ring lasers for rotation sensing. *Review of Scientific Instrument*, 8(4):041101 – 041101-26, April 2013. (Cited on page 8.)
- [66] K. U. Schreiber, J.-P. R. Wells, and G. E. Stedman. Noise processes in large ring lasers. *General Relativity and Gravitation*, 40(5):935–943, January 2008. (Cited on page 8.)
- [67] S.-C. Sheng. Optical-axis perturbation singularity in a out-of-plane ring resonator. *Optics Letters*, 19(10):683–685, May 1994. (Cited on page 7.)
- [68] D.V. Skryabin, A.G. Vladimirov, and A.M. Radin. Spontaneous phase symmetry breaking due to cavity detuning in a class A bidirectional ring laser. *Optics Communications*, 116(1-3):109–115, April 1995. (Cited on pages 7 and 24.)
- [69] J. J. E. Slotine and W. Li. *Applied nonlinear control*. Prentice-Hall, 1991. (Cited on page 31.)
- [70] R. J. C. Spreeuw, R. Centeno Neelen, N. J. van Druten, E. R. Eliel, and J. P. Woerdman. Mode coupling in a He-Ne ring laser with backscattering. *Physical Review A*, 42(7):4315–4324, October 1990. (Cited on page 6.)
- [71] A. Hepton Stall. LIGO website, January 2015. (Cited on pages 4 and 8.)
- [72] G. E. Stedman. Ring-laser tests of fundamental physics and geophysics. *Rep. Prog. Phys.*, 60(615):615–688, January 1997. (Cited on pages 7 and 8.)
- [73] G. E. Stedman, Z. Li, C. H. Rowe, A. D. McGregor, and H. R. Bilger. Harmonic analysis in a large ring laser with backscatter-induced pulling. *Physical Review A*, 51(6):4944–4958, June 1995. (Cited on pages 7, 24, and 25.)



- [74] F. Sun, X. Zhang, H.-B. Zhang, and C.-C. Yang. Dependence of mis-alignment sensitivity of ring laser gyro cavity on cavity parameters. In IOP Publishing, editor, *3rd International Photonics and OptoElectronics Meetings*, volume 276 of *Conference Series*, pages 1–5. Journal of Physics, IOP Publishing Ltd, 2010. (Cited on page 7.)
- [75] A. Tartaglia, J. Belfi, N. Beverini, A. Di Virgilio, A. Ortolan, A. Porzio, and M. L. Ruggiero. Light and/or atomic beams to detect ultraweak gravitational effects. In *EPJ WEB OF CONFERENCES*, volume 74 of *EPJ Web of Conferences*, pages 1–10. EDP Sciences, 2014. (Cited on pages 8, 11, 64, and 66.)
- [76] W. Tian. On tidal tilt corrections to large ring laser gyroscope observations. *Geophysical Journal International*, 196:189–193, January 2014. (Cited on pages 4 and 8.)
- [77] A. Velikoseltsev. The development of a sensor model for large ring lasers and their application in seismic studies. Master’s thesis, Technische Universität München, Arcisstraße, June 2005. (Cited on page 8.)
- [78] J.Y. Vinet, P. Hello, C. N. Man, and A. Brillet. A high accuracy method for the simulation of non-ideal optical cavities. *J. Phys I France*, 2:1287–1303, July 1992. (Cited on page 7.)
- [79] A. Di Virgilio, M. Allegrini, J. Belfi, N. Beverini, F. Bosi, G. Carelli, E. Maccioni, M. Pizzocaro, A. Porzio, U. Schreiber, S. Solimeno, and F. Sorrentino. Performances of ‘g-pisa’: a middle size gyro-laser. *Class. Quantum Grav.*, 27(084033):1–9, April 2010. (Cited on pages 8, 16, 38, and 39.)
- [80] D. Viswanath. The lindstedt-poincare technique as an algorithm for computing periodic orbits. *SIAM Rev*, 43(478), 2001. (Cited on page 27.)
- [81] K. Vogel, H. Risken, W. Schleich, M. James, F. Moss, and P. V. E. McClintock. Skewed probability densities in the ring-laser gyroscope: A colored noise effect. *Physical Review A*, 35(1):463–465, January 1987. (Cited on page 6.)
- [82] Jr. W. E. Lamb. Theory of an optical maser. *Physical Review*, 134(6A):1429–1450, June 1964. (Cited on pages 6, 13, and 23.)
- [83] Z. Wang and F. Wang. Nonreciprocal feedback in a ring laser and its application. *Optics Letters*, 37(23):5024–5026, October 2012. (Cited on page 7.)
- [84] J. Yuan and X. Long. Optical-axis perturbation in nonplanar ring resonators. *Optics Communications*, 281:1204–1210, October 2007. (Cited on page 7.)

- [85] J. Yuan, X. Long, and M. Chen. Generalized ray matrix for spherical mirror reflection and its application in square ring resonators and monolithic triaxial ring resonators. *Optics Express*, 19(7):6762–6776, March 2011. (Cited on pages 7 and 54.)
- [86] J. Yuan, X. Long, and L. Liang. Optical-axis perturbation in triaxial ring resonator. *Applied Optics*, 47(5):628–631, February 2008. (Cited on page 7.)
- [87] J. Yuan, X. Long, L. Liang, B. Zhang, F. Wang, and H. Zhao. Nonplanar ring resonator modes: generalized gaussian beams. *Applied Optics*, 46(15):2980–2988, May 2007. (Cited on page 7.)
- [88] H. Zeglache, P. Mandel, N. B. Abraham, L. M. Hofkr, G. L. Lippi, and T. Mello. Bidirectional ring laser: Stability analysis and time-dependent solutions. *Physical Review A*, 37(2):470–497, January 1988. (Cited on page 6.)

#### COLOPHON

This document was typeset using the typographical look-and-feel classicthesis developed by André Miede. The style was inspired by Robert Bringhurst's seminal book on typography "*The Elements of Typographic Style*". classicthesis is available for both L<sup>A</sup>T<sub>E</sub>X and L<sup>Y</sup>X:

<http://code.google.com/p/classicthesis/>

Happy users of classicthesis usually send a real postcard to the author, a collection of postcards received so far is featured at:

<http://postcards.miede.de/>

*Final Version* as of April 7, 2015 (classicthesis version 2).